Dissertation

Molecular Nano-Architecture

of

Synaptic Vesicle Clusters in Mammalian Synapses

Steffen Saß

2024

Inaugural dissertation

for

obtaining the doctoral degree

of the

Combined Faculty of Mathematics, Engineering and Natural Sciences

of the

Ruprecht - Karls - University

Heidelberg

Presented by

M.Sc. Biologie Steffen Saß

born in: Pinneberg, Germany

Oral examination: …….

Molecular Nano-Architecture

of

Synaptic Vesicle Clusters in Mammalian Synapses

Referees: Prof. Dr. Thomas Kuner

Prof. Dr. Christoph Schuster

Abstract

Chemical synapses are essential for neuronal processing of information. Synaptic plasticity, the ability to alter the strength of a synapse, is the basis for learning and higher cognitive functions. The properties of synaptic transmission are strongly affected by the organisation of synaptic vesicles (SV) into SV pools. The majority of SV pool concepts agrees on the following three main classes: the readily releasable pool (RRP), which is capable of immediately responding to an AP event, 2) the recycling pool which consists of SVs that are actively participating in the SV cycle but are not release-competent yet, and 3) the reserve pool which is comprised of SVs that are immobile or irresponsive under physiological conditions; the latter also being referred to as “mature” SVs. This maturation process is tightly linked to the age of a given SV and therefore must include a molecular or spatial marker of sort. A handful of candidate proteins has been investigated *in vitro* but convincing evidence *in vivo* is lacking to date.

The calyx of Held, a relay station in the auditory pathway, represents an ideal model synapse for this endeavour because of its recognisable appearance, strongly conserved and repetitive structure and the expression of multiple paralogs of major SV proteins (e.g. VAMP and vGluT), which can be studied side-by-side.

To investigate protein distribution patterns at the scale of SVs is a challenging task due to the size of SVs, approximately half an order below the diffraction limit of light microscopy. *direct* Stochastic Optical Reconstruction Microscopy (*d*STORM) lowers the resolution limit to around 30 nm and permits insights into the nano-architecture of mammalian synapses. The employed multiplexed automated serial staining STORM (maS³TORM) microscope combines the principles of *d*STORM with automated restaining capabilities for highly multiplexed protein correlation studies.

To further improve the maS³TORM approach, I developed an immobilisation approach for carboxylated nanoparticles that allows restaining-based multiplexing of 10-15 targets with high image registration precision. To ensure calyx-specific interpretation of my results, I confirmed the extracalyceal origin of a VAMP2 and vGluT2-positive subset of terminals that are contacting the MNTB principal cell and developed an approach that allows identification of these terminals without the need of an artificially expressed marker like GFP. Using optimized highly multiplexed maS³TORM imaging, I investigated the protein distribution within calyceal as well as extracalyceal terminals and extracted leads towards molecular SV pool markers that label spatially distinct subsets of SVs.

I reveal the distinct distribution of multiple SV cycle proteins in subpopulations of the SV cluster and conclude that SV pool identity might not be conferred by specialised proteins, but rather represents the sum of secondary interactions of key players of the SV cycle, thus adding another layer of complexity to the protein expression profile of chemical synapses.

Zusammenfassung

Chemische Synapsen sind essentiell für die neuronale Verarbeitung von Informationen. Synaptische Plastizität, also die Fähigkeit die Stärke einer Synapse zu verändern, ist die Basis für Lernfähigkeit und höhere kognitive Funktionen. Die Eigenschaften der synaptischen Übertragung werden stark durch die Organisation von synaptischen Vesikeln (SV) in SV Pools beeinflusst. Die Mehrheit der SV Pool Konzepte stimmen den folgenden drei Hauptkategorien zu: 1) dem schnell abrufbaren Pool (RRP), welcher in der Lage ist, sofort auf ein Aktionspotenzial zu reagieren, 2) dem Recycling Pool, welcher aus SV besteht, die aktiv am SV Zyklus partizipieren, jedoch noch nicht bereit für eine erneute Ausschüttung sind, und 3) dem Reserve Pool, welcher durch SV gebildet wird, die unter physiologischen Bedingungen unbeweglich oder teilnahmslos sind; Letztere werden auch als "reife" SV bezeichnet. Dieser Alterungsprozess ist eng mit dem Alter von SV verknüpft und muss daher eine molekulare oder räumliche Markierung irgendeiner Art beinhalten. Eine Handvoll potenzieller Proteine wurde bereits in vitro untersucht, überzeugende Belege in vivo fehlen allerdings bis heute.

Die Calyx von Held, eine Relaisstation in der Hörbahn, stellt eine ideale Modellsynapse für dieses Vorhaben dar, auf Grund ihrer wiedererkennbaren Erscheinung, ihrer stark konservierten und sich wiederholenden Struktur und der Expression von mehreren Paralogen wichtiger SV Proteine (z.B. VAMP und vGluT), welche daher nebeneinander untersucht werden können.

Proteinverteilungsmuster auf der Ebene von SV zu untersuchen ist eine herausfordernde Aufgabe auf Grund der Größe von SV, welche eine halbe Größenordnung unterhalb der Auflösungsgrenze von sichtbarem Licht liegt. direkte Stochastische Optische Rekonstruktionsmikroskopie (dSTORM) reduziert die Auflösungsgrenze auf ungefähr 30 nm und ermöglicht daher Einblicke in die Nanoarchitektur von Säugetiersynapsen. Das eingesetzte multiplexe automatisierte Serienfärbungs-STORM- (maS³TORM) Mikroskop kombiniert das Prinzip von *d*STORM mit automatisierten Umfärbungsfähigkeiten für hochmultiplexe Korrelationsstudien.

Um den maS³TORM Ansatz weiter zu verbessern, habe ich einen Immobilisierungsansatz für carboxylierte Nanopartikel entwickelt, welcher Umfärbung-basiertes Multiplexing von 10-15 Zielen mit hoher Bildregistrierungspräzision erlaubt. Um eine Calyx-spezifische Interpretation meiner Ergebnisse sicherzustellen, habe ich den extracalycären Ursprung einer VAMP2- und vGluT2-reichen Subpopulation von Nervenenden, welche die MNTB Prinzipalzelle kontaktieren, bestätigt und einen Ansatz entwickelt, welcher die Identifikation dieser Nervenenden ohne die Notwendigkeit einer künstlich exprimierten Markierung wie GFP ermöglicht. Unter Nutzung der

optimierten, hoch-multiplexen maS³TORM Bildgebung habe ich die Proteinverteilung in calycären sowie extracalycären Nervenenden untersucht und Hinweise in Richtung molekularer Marker entnommen, welche spezifische Subpopulationen von SV markieren.

Ich zeige die unterschiedliche Verteilung mehrerer SV Zyklus-Proteine in Subpopulationen von SV Ansammlungen und folgere daraus, dass die Identität von SV Pools möglicherweise nicht durch spezialisierte Proteine verliehen wird, sondern wahrscheinlicher die Summe sekundärer Funktionen von Schlüsselakteuren des SV Zyklus darstellt, wodurch der Proteinexpression der chemischen Synapse eine weitere Komplexitätsebene hinzugefügt wird.

List of Publications

Narayanasamy KK, Stojic A, Li Y, **Sass S**, Hesse MR, Deussner-Helfmann NS, Dietz MS, Kuner T, Klevanski M and Heilemann M (2021) Visualizing Synaptic Multi-Protein Patterns of Neuronal Tissue With DNA-Assisted Single-Molecule Localization Microscopy. *Front. Synaptic Neurosci*. 13:671288. doi: 10.3389/fnsyn.2021.671288

Klevanski M, Herrmannsdoerfer F, **Sass S**, Venkataramani V, Heilemann M and Kuner T (2020) Automated highly multiplexed super-resolution imaging of protein nano-architecture in cells and tissues. *Nat Commun* 11, 1552. doi: 10.1038/s41467-020-15362-1

Contents

List of Figures

List of Tables

List of Abbreviations

*d*STORM	*direct* Stochastic Optical Reconstruction Microscopy
(e)GFP	(enhanced) Green Fluorescent Protein
pAB/sAB	primary/secondary Antibody
2D	Two-Dimensional
3D	Three-Dimensional
a.u.	arbitrary units
AZ	Active Zone
ch	Chicken
ddH_2O	double-distilled water (“Milli-Q”)
EDC	1-Ethyl-3-(3-dimethylaminopropyl)carbodiimide
EM	Electron Microscopy
FWHM	Full Width (at) Half Maximum
GB***	Gold Beads (of *** nm diameter)
GBC	Globular Bushy Cells
gp	Guinea pig
IF	Immunofluorescence
IgG1	Immunoglobulin Type G1
MEA	Mercaptoethylamine
MES	2-(N-morpholino)ethanesulfonic acid
MinFlux	Minimal photon Fluxes

MNTB	Medial Nucleus of the Trapezoid Body
ms [pAB/sAB]	Mouse
ms [time]	millisecond
ms(k)	Mouse (kappa light chain)
ND	Nanodiamonds
P**	Prenatal day ** (e.g. P14)
PBS	Phosphate-Buffered Saline
P_R	Release Probability
PSA	*Pisum Sativum* Agglutinin
PSF	Point Spread Function
px	pixel
Rab3a	Ras-related protein Rab-3A
rb	Rabbit
ROI	Region Of Interest
RP	Reserve Pool
RRP	Readily Releasable Pool
SD	Spectral Demixing
SDS	Sodium Dodecyl Sulphate
SMLM	Single Molecule Localization Microscopy
SNAP25	Synaptosomal-Associated Protein, 25kDa
SNARE	Soluble NSF Attachment Protein Receptor
SNR	Signal-to-Noise Ratio
SR	Staining Round
SRM	Super-Resolution Microscopy
StD	Standard Deviation
SV	Synaptic Vesicle
SV2	Synaptic Vesicle Protein 2
TIFF	Tagged Image File Format
TS	TetraSpeck™ Microspheres
VAMP	Vesicle-Associated Membrane Protein
VCN	Ventricle Cochlear Nucleus
vGluT	vesicular Glutamate Transporter
WGA	Wheat Germ Agglutinin

1. Introduction

1.1 The Glutamatergic Synapse

1.1.1 Synaptic Neurotransmission

Neuronal information processing is the basis of cognition and cue-based adaptive reactions. In simple terms, sensory information is received, integrated and an action is performed based on the outcome of the information processing. The integration of said information is achieved through a complex network, in vertebrates represented by the central nervous system (CNS), whose smallest building blocks are neurons. Neurons transport information as electric signals and predominantly communicate with one another via neurotransmitters. This process of synaptic transmission occurs at specialised cell-cell contacts, the chemical synapse. Here, an arriving electrical signal, the action potential (AP), depolarises the cell membrane and in turn activates voltage-gated Ca^{2+} channels. The influx of Ca^{2+} triggers the exocytosis of neurotransmitters from their storage vessels, the synaptic vesicles (SVs), into the synaptic cleft. On the postsynaptic side, ligand-gated ion channels located at the postsynaptic density (PSD), the postsynaptic equivalent of the AZ, await the arrival of the neurotransmitters and, upon binding, allow ion influx into the postsynaptic cell[1]. Depending on the type of postsynaptic receptor, the corresponding ion influx either depolarises the postsynaptic cell and therefore facilitates the propagation of the AP (excitatory input) or hyperpolarises it and thus dampens neurotransmission (inhibitory input). The sum of excitatory and inhibitory inputs to a certain neuron determines if and when an AP is relayed and therefore shapes the computational output of the neuronal network. While some neurotransmitters are tightly associated with a certain mode of action (e.g. glutamate with excitation, γ-aminobutyric acid (GABA) or glycine with inhibition), ultimately the postsynaptic receptor type alone determines the effect on AP generation[2]. In addition to the AP-dependent - evoked - neurotransmitter release, spontaneous release occurs, although its purpose and regulation are still not fully understood[3,4].

In the adult brain, neurons are terminally differentiated[5] and neurogenesis is low[6,7]. Adaption of the network is instead achieved by alteration of the number and strength of synaptic connections, a process called synaptic plasticity. All CNS synapses share the set of common building blocks as discussed above (SVs, AZ, PSD, etc.), but differ in (nano-) architecture and copy numbers. This is referred to as synaptic heterogeneity or synaptic diversity and enables the cognitive

processes that we characterise as intelligence: situational learning and adaptation to changing environments[8].

Synaptic architecture has already been reviewed from many perspectives[9–14]. This introduction will therefore focus on the presynaptic side of the excitatory, glutamatergic synapse in general and the morphology of the model synapse of the calyx of Held in particular, as they are of relevance for the present study.

1.1.2 Nanoarchitecture of the Glutamatergic Presynapse

1.1.2.1 Organisation of the Active Zone

Neuronal networks require highly synchronous activity to maintain function. For this reason, neurotransmission is tightly regulated both spatially and temporally. For example, the exocytosis of neurotransmitters, with the exception of modulatory neuropeptides from dense core vesicles[15], is spatially restricted to the membrane specialisation called the active zone (AZ; Figure 1.1a). It harbours the release machinery that facilitates SV exo- and endocytosis as well as the ion channels that temporally control transmitter release[16]. The AZ is in turn precisely aligned with the postsynaptic site of neurotransmitter reception, the PSD[17]. SVs are typically strongly enriched towards the AZ[18].

The AZ itself is comprised of various multi-protein complexes (Figure 1.1b). The cytomatrix proteins Bassoon, Piccolo, RIM, RIM-BP, ELKS, Liprin-α and Munc13 provide the scaffold that guides the release machinery in place. Of these proteins, RIM is believed to be the master regulator of AZ formation as direct interactions with most AZ proteins have been demonstrated[16]. One of these interactions recruits voltage-gated Ca^{2+} channels to the AZ[19], whose composition and distribution is an important factor for SV release kinetics[20]. Exocytosis is mediated by the soluble NSF attachment protein receptor (SNARE) complex, which consists of three different Q-SNARE and one R-SNARE motif. During SV exocytosis, these motifs form a quad-helical core complex that provides the energy which is necessary for membrane fusion. The R-SNARE motif is provided by the vesicle-associated membrane protein (VAMP), in the CNS predominantly represented by the paralogs VAMP1 and -2. The AZ membrane-anchored Syntaxin contributes a Q_a-SNARE motif and the synaptosomal-associated protein of 25 kDa (SNAP25) possesses both a Q_b- and Q_c-SNARE motif[21,22]. Towards the outer regions of the AZ, the peri-active zone, the components of the Clathrin-dependent endocytosis pathway are located. To quickly clear the site of exocytosis and allow docking and priming of a new set of SVs, the remnants of fused SVs are displaced outwards of the AZ and retrieved for recycling there[23].

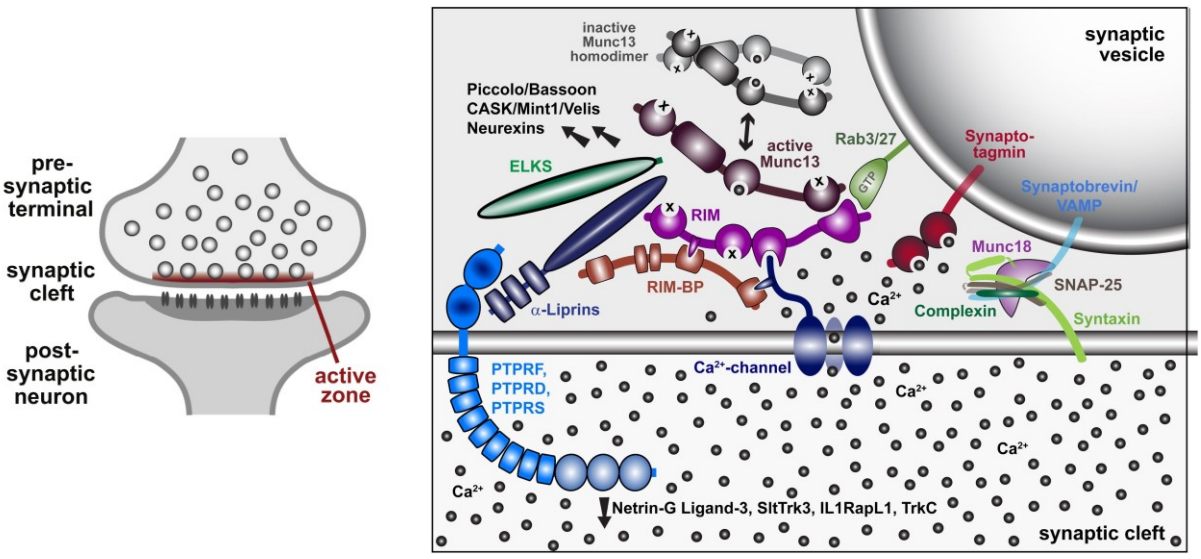

Figure 1.1 Structural organisation of the synapse. A synapse consists of a presynaptic terminal, which contains SVs that are exocytosed in the area of the AZ, opposed by the postsynaptic density and separated by the synaptic cleft (**a**). In the AZ, a multitude of cytomatrix, ion channels and release machinery proteins facilitate neurotransmitter release (**b**). (with permission from Südhof, 2012[1])

1.1.2.2 The Synaptic Vesicle Cycle

The release cycle begins with neurotransmitter-filled SVs in close proximity to the AZ. A complex of Munc13, Rab3 and RIM tethers the SV to the AZ, a process called docking. Binding of SV-associated Synaptotagmin to the AZ membrane enables SNARE complex formation. In a process involving Munc18, an SV-bound VAMP engages with AZ membrane-bound SNAP25 and Syntaxin and partially forms the *trans*-SNARE complex. The now primed SV is prevented from immediate exocytosis by a protein clamp, which is comprised of Synaptotagmin and Complexin and inhibits complete zippering of the SNARE motifs. Upon Ca^{2+} entry, triggered by the opening of the voltage-gated Ca^{2+} channels in the AZ membrane in response to an AP, Ca^{2+} binds to Synaptotagmin, releases the clamp and SNARE complex formation can continue to conclude SV exocytosis[1,24].

While one SNARE complex appears to be sufficient to provide the energy which is necessary for membrane fusion, numbers in a range of 3-15 complexes have been observed[25,26]. Given the intricate assembly process of the SNARE complex and its competition with off-target SNARE pathways, this process is unlikely to take place spontaneously. An elegant solution for a guided SNARE complex formation has been proposed recently: on the SV surface, Synaptophysin and VAMP2 (but not VAMP1[27]) dimers are proposed to form a hexameric complex, which would lower the entropic barrier for membrane fusion and thus catalyse the SNARE complex formation, allowing it to assemble at the speed necessary to maintain synchronous signalling[28,29]. A

complementary hexameric protein complex on the AZ membrane, consisting of Munc13, has been suggested as well. In the proposed scenario, the second hexamer would capture Synaptotagmin from the SV membrane to align both hexameric assemblies, which would facilitate VAMP2-binding and finally recruit Syntaxin-Munc18 heterodimers and SNAP25 proteins from the AZ membrane to fully assemble the *trans*-SNARE complex[30].

Before the SV can be retrieved from the AZ membrane, the SNARE complex needs to be disassembled. Since the zippering of the SNARE motifs released substantial amounts of energy, ATP is required to reverse the process. This is mediated by the N-ethylmaleimide-sensitive fusion protein (NSF), which dissociates both the post-fusion *cis*-SNARE complex as well as non-canonical off-target SNARE assemblies[22]. The SV is then retrieved from the plasma membrane either through Clathrin-mediated endocytosis (CME) or, under intense stimulation, activity-dependent bulk endocytosis (ADBE). Alternative pathways, e.g. ”kiss-and-run”, have been demonstrated but are controversially discussed[31–33]. After retrieval, SVs are refilled with transmitters before the cycle can be reiterated. In glutamatergic synapses, the key proteins for SV loading are vesicular ATPases and the vesicular glutamate transporters (vGluT) 1 and -2[34].

1.1.2.3 **Release Probability and Synaptic Vesicle Pools**

As mentioned above, APs do not necessarily trigger transmitter release in response to an arriving AP. The likelihood of an AP to be propagated by a certain AZ has been termed the release probability (P_R). As a main factor of synaptic short-term plasticity, P_R is dynamically regulated. At the level of the AZ, the availability of docked and primed SVs and control of cytoplasmic Ca^{2+} levels are two of the means that determine P_R. This topic has been reviewed extensively[35–37].

However, the concept of P_R can also be applied on the SV level, since only a subset of SVs is released upon stimulation and even the docked and primed state of an SV does not predict fusion. It was recognised that subpopulations of SVs exhibit similar P_R and as a consequence the concept of SV pools was established. Terminology and the number of distinguished pools differ between publications, but from a functional point of view three main pools are widely agreed on: the readily releasable pool (RRP) that consists of SVs which are docked and primed and therefore able to immediately respond to an AP; the recycling pool (RP) that comprises SVs which have recently undergone a SV cycle and can be recruited for secretion on a short time scale; and the reserve or resting pool which consists of SVs that are neither RRP nor RP[38]. While the first two pools are therefore easily defined based on the observed SV cycle phase of a given SV, the resting pool (or pools) lack(s) a clear definition. Commonly, the mobility or immobility of SVs at a given time

or under certain stimulation conditions is used as a denominator, especially when the reserve pool is further subdivided[39]. In addition, a super pool of SVs has been reported, which contains SVs that are trafficked between synapses of the same neuron[40].

It has been demonstrated that the synapse is capable of tracking SV identities over multiple SV cycles. Since the probability of damages to the SV-inherent protein equipment increases with SV age and consequently elevates the risk of release failure, SV employment is reduced with age[41]. To date, the mechanisms that allow SV tracking are still under investigation. While initially it was proposed that SV pools might be spatially segregated and therefore could be distinguished by geometric features, this concept does not align well with actual observations[42,43]. However, the concept of spatially intermixed but functionally distinct SV pools axiomatically predicts one or multiple molecular markers that allow the synapse to distinguish between SV identities[44]. Different recycling pathways might be involved to maintain SV identity after exocytosis[45]. SNAP25 has been identified as a potential pool marker, which is sporadically sorted from the plasma membrane into newly retrieved SVs and thus reduces the chance of successful *trans*-SNARE complex formation and, in turn, exocytosis. This process was termed maturation and provides one of the first experimentally proven definitions for a resting pool[41]. Other proteins, e.g. Synapsins, have been linked with resting pool formation as well. It was suggested that synapsins either bridge SVs to actin filaments and/or other SVs in a phosphorylation- or Ca^{2+}-dependent, reversible manner or immobilise them by liquid-liquid phase separation[46,47]. However, Synapsins dissociate from the SV under stimulation[48], therefore the SV would lack a correlate that remains bound under mobile conditions and allows continuous identity tracking.

In addition to SV pools that are distinguished by their P_R, in the calyx of Held two subpopulations of SVs have been identified that exhibit distinct release kinetics: the fast and slow releasing vesicle pools[49]. They are thought to represent the two forms of AP-evoked transmitter release, synchronous and asynchronous release, respectively[50].

In conclusion, while the classic distinction of SV populations into a handful of pools, regardless of them being segregated or intertwined, provides a very approachable concept of SV regulation, it is becoming increasingly clear that a simple pool concept as it is introduced above is an oversimplification and unfit to account for the various forms of release heterogeneity that are observed *in vivo*[51].

1.1.2.4 Specific Functions of Select Presynaptic Proteins

Over 1 000 different proteins have been detected in the presynaptic terminal[52], 410 of which have been identified on SVs[53]. This study could only cover a select subset of presynaptic proteins, which I chose for the following reasons:

VAMP1 and -2 are SV-bound, mutually exclusive members of the SNARE complex which, while they are structurally closely related and can substitute for each other in cultured hippocampal neurons, possess highly different regulatory sequences and are associated with different P_R as a consequence[54]. Since, in contrast to the exclusive expression pattern in most of the CNS[55], the calyx of Held (see below) contains both paralogs, this allows to investigate whether they label distinct subpopulations and thus could be a potential pool marker, or coexist on SVs.

Similarly, vGlut1 and -2 are structurally related but differentially regulated, thus exhibit different P_R [56,57], and mostly occur in distinct parts of the brain but are co-expressed at the calyx[58].

Synaptophysin exclusively interacts with VAMP2, not VAMP1, and has been demonstrated to be involved in VAMP2-dependent exocytosis as well as playing a role in VAMP2 retrieval from the plasma membrane during endocytosis[59]. Generally, Synaptophysin is thought to be present on the vast majority of SVs[53] and might thus serve as a SV proxy.

SNAP25 has already been linked to SV pool formation, in that its labelling an aged subpopulation of SVs which are characterised by a significantly reduced P_R[41]. While Truckenbrodt *et al.* avoid a direct statement whether this subpopulation represents a SV pool, the mechanism fulfils all criteria of common definitions. The question whether the aging process of SVs has spatial consequences has not been addressed, yet.

Rab3 dynamically associates with SVs in a GTP-dependent manner[60]. As part of the SV docking machinery, it has been implicated in “superpriming” of a subset of SVs, i.e. boosting of P_R. As a consequence, Rab3 has been associated with the fast-releasing SV pool of the calyx of Held[61]. This mechanism has been reported to involve Rabphilin3a, which links Rab3 to SNAP25 and promotes both SV docking and SNARE complex formation[62]. Since multiple isoforms of Rab3 exist, this study is focused on the most abundant form which is Rab3a.

Although SV2 only seems to be present on SVs at comparably low copy numbers, it was reported to be particularly evenly distribution among SVs[63]. The distributional precision reflects the importance of SV2 for unimpaired neurotransmission, although its exact role is still under

investigation. Regulation of SV exocytosis, likely by binding to Synaptotagmin has been reported[64]. Lack of SV2 on a subset of SVs would therefore be a striking discovery.

1.1.3 The Calyx of Held

An essential function of the mammalian auditory system is the ability to localise the source of a sound wave. This is, amongst others, achieved by comparing the interaural time delay and intensity level difference of a sound wave. To cross-correlate these cues, part of the auditory pathway needs to cross from one ear over to the contralateral side of the brainstem.

APs are generated in the cochlea and travel along the vestibulocochlear nerve to the ventral cochlea nucleus (VCN; Figure 1.2). Here, they are relayed onto globular bushy cells (GBCs) via the endbulbs of Held. From the VCN, the axons of GBCs project to the contralateral superior olivary complex (SOC), more specifically the medial nucleus of the trapezoid body (MNTB), where in a second relay station, the calyx of Held, the glycinergic MNTB principal cell is innervated. The calyx of Held contacts the soma of a single principal cell, which in turn projects to the lateral superior olive (LSO), where finally the ipsilateral and contralateral projections from the VCN are integrated. Extensive reviews are provided by Schneggenburger and Forsythe[65] or more recently by Baydyuk *et al.*[66].

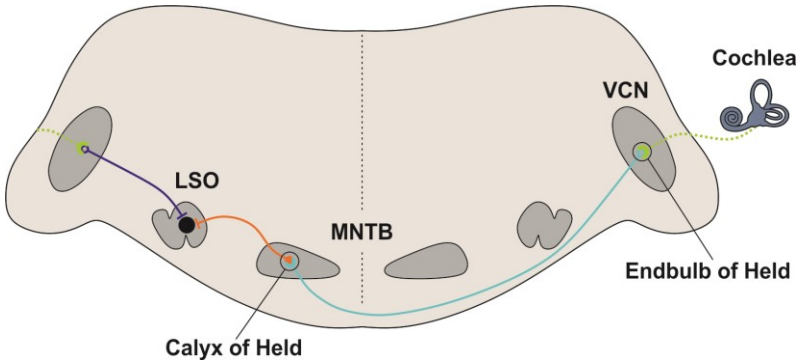

Figure 1.2 The Auditory Pathway of Sound Localisation in the Brainstem. GBCs receive auditory information from the cochlea via endbulb of Held synapses in the VCN. GBC axons project to the contralateral MNTB, where they terminate in calyx of Held synapses and contact the MNTB principal cell. Finally, auditory information from the ipsi- and contralateral ear is integrated in the LSO. (based on Cramer, Rubel, 2016[67])

In adult rodents, the majority of GBC axons give rise to a single calyx, thus forming a 1:1 connection with the principal cell. At prenatal age, polyinnervation is observed more frequently, which then decreases[68–71] towards the onset of hearing around P12[72]. Within the same time course, the cup-shaped prenatal proto-calyx matures into a highly fenestrated, complex geometry[73,74] (see below). In addition to the calyx, various non-calyceal inputs to the principal cell

have been described[75]. The exact origins and functions of these inputs are still under debate, but both precalyceal[76] and extracalyceal[77,78] identities have been demonstrated. Confirmed sources of extracalyceal afferents are a subset of the periolivary nuclei[79] as well as the ventral nucleus of the trapezoid body[79,80]. While the calyx as an excitatory synapse solely releases glutamate, extracalyceal inputs have been confirmed to be both excitatory[81] and inhibitory[77,82] in nature.

At a diameter of ~ 20 µm, the calyx of Held with its MNTB principal cell is remarkably large in size. This allows simultaneous electrophysiological recordings from both the pre- and postsynaptic side and has enabled detailed functional characterisation of this synapse[83–86]. The mature calyx wraps around the spherical soma of the principal cell with multiple digit-like stalks which taper down into necks and swellings[87] (Figure 1.3a). At the contact sites between calyx and principal cell, hundreds of AZs are located (Figure 1.3b,c). In many aspects, these AZs resemble those found in smaller, bouton-type synapses[88,89]. However, the highly paralleled neurotransmission infrastructure allows the calyx to follow significantly higher AP frequencies of between 350 Hz[90] to 800 Hz[91] under intense stimulation. This is achieved by the high number and low P_R of AZs to avoid synaptic depression and specific adaptations of the release machinery and postsynaptic receptor composition to ensure highly synchronous signalling[91].

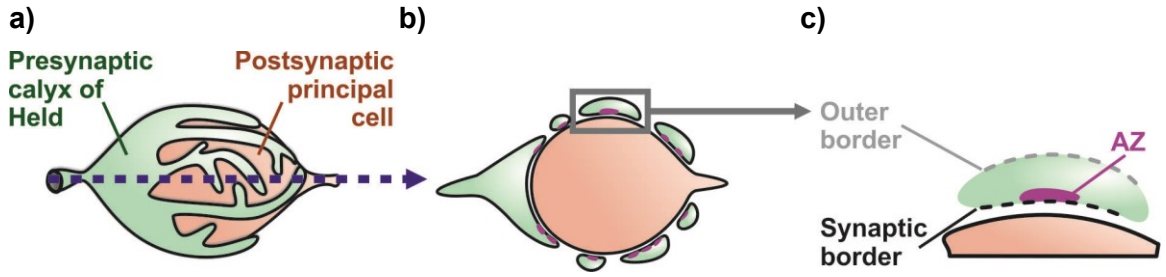

Figure 1.3 Structural Overview of the Calyx of Held. The presynaptic calyx of Held encloses the postsynaptic principal cell with multiple digit-like protrusions (**a**). A cross-section along the main axis reveals a multitude of synaptic contacts between the presynaptic compartments and the principal cell (**b**). Synaptic contacts are characterised by the presence of one or multiple AZs which are located at the synaptic border (**c**). **b** and **c** represent prototypic examples of the orientation that was examined in this study. (modified from Klevanski, Herrmannsdoerfer, Sass *et al.,* 2020[92])

From an imaging perspective, the calyx of Held offers three major advantages: first, the large size of the calyx means that ultrasectioning of the tissue readily opens up the cellular compartments of pre- and postsynaptic neurons and thus supersedes the use of permeabilisation agents; second, the dense arrangement of a multitude of calyces in the MNTB ensures a sufficient number of target structures in each ultrasection; and third, the highly conserved geometry of numerous AZs facilitates target structure identification and orientation[92]. In addition, the presence of

glutamatergic terminals from multiple origins enables a direct comparison of nanoarchitectural features in a single preparation.

1.2 Microscopy

1.2.1 Principles of Light Microscopy

The proteins and molecular machineries that shape neurotransmission have a size in the range of a few to some tenths of nanometres and are spatially organised on even smaller scales. To visualise molecules at these length scales, specialised microscopes are necessary. Two milestone developments ultimately gave access to this molecular domain of imaging: Firstly, the introduction of fluorescent dyes which drastically improved the contrast, in camera-based microscopes usually referred to as the signal-to-noise ratio (SNR). And secondly, techniques that circumvent the lateral resolution limit by spatially or temporally modulating the emission state of said fluorescent molecules, typically summarised as super-resolution microscopy (SRM). In this chapter, I will lay out the fundamentals behind these developments and explain the considerations that led to the development of our multiplexed automated serial staining STORM (maS³TORM) microscope.

1.2.1.1 Fluorescence Microscopy

Early light microscopy methods relied on density differences or simple dyes to provide contrast by diffracting, refracting or absorbing transmitted polychromic light. However, the contrast levels that could be achieved this way were severely limited and allowed only the identification of larger morphological features on a cellular level. In the second half of the 19th century, George Stokes and others discovered the phenomenon of fluorescence, in which a molecule – called fluorophore – absorbs a photon of appropriate wavelength, i.e. energy, and subsequently reemits a photon of larger wavelength. Due to this wavelength shift, appropriately named Stokes shift, fluorescence emission can be separated from the excitation light and therefore allows imaging of fluorophore-bound target molecules at an exceptionally high SNR[93].

The basis for fluorescence to occur are valence electrons that remain in an excitable ground state (S_0), from which they can be raised to an excited singlet state upon the absorption of a compatible photon (Figure 1.4). If the excited energy level exceeds the first excited singlet state (S_1), the electron immediately relaxes to the S_1 state through internal conversion or vibrational relaxation. The excess energy is dissipated into the surrounding solution in the form of vibrational energy,

i.e. heat, and the resulting energy delta equates to the aforementioned Stokes shift. From the S_1 state, typically within a few nanoseconds, the electron relaxes back to the ground state by emitting a new photon of now decreased energy and therefore red-shifted wavelength. The fluorophores which are typically used for microscopy applications repeat this cycle several hundreds to thousands of times, thus giving rise to an equal amount of photons, before they bleach or transit into a dark state. These dark states are created by intersystem crossing, where the excited electron randomly inverts spin and thus reaches the first excited triplet state (T_1). As this spin inversion is deemed physically forbidden and therefore comparably unlikely, but needs to be reversed for the electron to relax back to the S_0 state, the T_1 state exhibits much longer lifetimes, typically in a range of milliseconds to seconds; this process is called phosphorescence and causes fluorophores to blink. In the presence of reducing agents such as primary thiols, the T_1 state fluorophore can be reduced to a radical ($R^{\bullet}$) and, in some cases, further into a leuco dye (RH), both of which represent stable dark states. Molecular oxygen with its triplet ground state efficiently quenches all three of these dark states and therefore repopulates the S_0 state of the fluorophore, but creates reactive oxygen species (ROS) in the process. In applications where bleaching is critical or long-lived dark states are favoured, oxygen needs to be depleted from the sample medium[94]. If the cycling between an excitable and a non-fluorescent or dark state is induced intentionally, it is referred to as photo-switching.

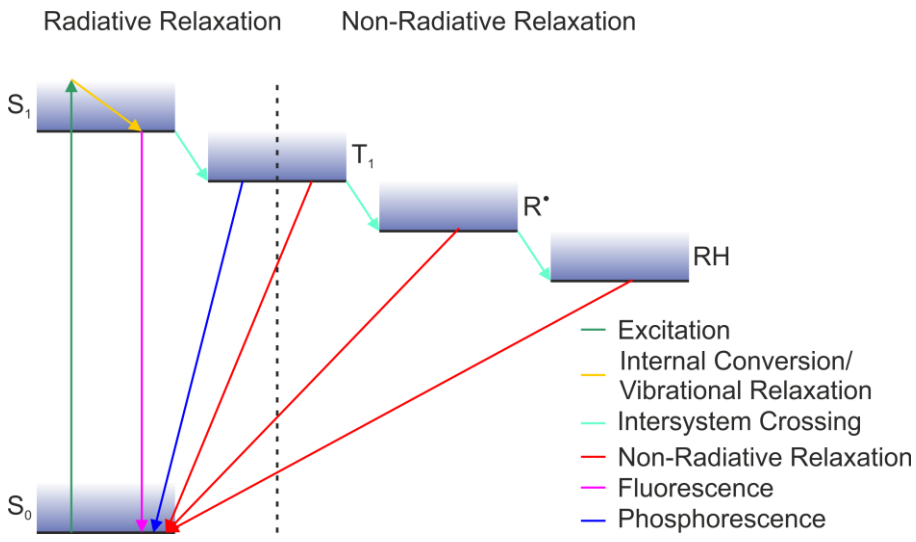

Figure 1.4 Simplified Jablonski diagram of a fluorophore in the presence of a reducing agent. Valence electrons are raised from the ground state (**S_0**) to an excited singlet state (e.g. **S_1**) by absorption of a photon of appropriate energy. Radiative relaxation to S0 gives rise to fluorescence, intersystem crossing populates the triplet state (**T_1**) and causes phosphorescence. In the presence of a reducing agent, a fluorophore in the meta-stable T1 state can be reduced into a radical (**R**·) or leuco state (**RH**), which arrests the fluorophore in a stable dark state until it non-radiantly relaxes back to S_0 after collision with a suitable oxidation agent, e.g. molecular oxygen.

A wide variety of fluorophores exist that cover the entire visible spectrum of light, some of which are photo-convertible or -switchable, or change their characteristics dependent on the ambient pH or the presence of a ligand. Fluorophores can be conjugated to a repertoire of target-binding molecules such as antibodies, nanobodies, lectins, toxins, aptamers, oligonucleotides or protein tags (for details see 1.2.4) or, in the case of fluorescent proteins, are expressed directly in tandem with the target protein. Therefore, the combination of fluorophore and label needs to be carefully considered to suit the experimental conditions.

1.2.1.2 The Diffraction Limit

Due to the wave nature of light, it is subject to diffraction. Following the Huygens-Fresnel principle, the lens system of a microscope acts as a circular aperture and introduces diffraction to microscopic images. In the image plane, the diffracted rays of light interfere with one another and create a concentric two-dimensional pattern, known as the Airy pattern. As a result, even an infinitesimal point emitter can only be focussed to a finite size, in microscopy represented by the bright spot in the centre of an Airy pattern, the Airy disc. The Airy pattern follows a Bessel function, where the Airy disc represents its zero order maximum and can therefore be closely approximated by a Gaussian function. Translated into 3D, the Airy pattern is known as the Point Spread Function (PSF) of the microscope[95]. Even though in theory describing different aspects of the image formation, the terms Airy disc and PSF are often used synonymously. For reasons of simplicity, the term PSF will be used for the detectable representation of a point emitter in the image plane throughout this thesis.

In 1903, Lord Rayleigh noticed that a pair of point emitters, which individual fluorophores essentially are, needed to be a certain distance $d_{x,y}$ apart to be observed as such. More specifically, once the PSF of one emitter coincided closer with the centre of the second PSF than the first minimum of its Airy pattern, the pair of emitters became indistinguishable. Hence, this phenomenon was termed the Rayleigh criterion and is summarised by Equation 1[96]:

$$d_{x,y} = \frac{0.61\,\lambda}{NA} \qquad \textbf{Equation 1}$$

where λ is the wavelength of light and NA the numerical aperture, i.e. the product of the refractive index of the immersion medium and the sine of semi-aperture angle of the objective lens. The axial derivative (d_z) is given by Equation 2[96]:

$$d_z = \frac{2\,\lambda}{NA^2} \qquad \textbf{Equation 2}$$

With modern optics, this limits the lateral resolution to approximately half of the wavelength. Since the visible light spectrum begins at ~400 nm, this equates to a resolution limit of ~200 nm. The axial resolution is always lower than the lateral resolution and in this example equates to ~550 nm.

An implication from the Rayleigh criterion is that a reduction of the illumination wavelength of a microscope is directly proportionate to an increase in resolution capabilities. As a result, electron microscopy (EM) was created, which utilises that electrons possess de Broglie wavelengths in the picometre range. However, electrons as an illumination source only allow visualisation of electron density differences in the sample and create various new challenges[97]. In addition, the identification of molecular targets, e.g. specific proteins, is severely limited, therefore rendering it unsuited for the present study.

1.2.2 Super-Resolution Microscopy

1.2.2.1 Spatial Fluorescence Modulation Techniques

Instead of decreasing the wavelength of the illumination or excitation source, early SRM approaches relied on the spatial modulation of the excitation light to bypass the diffraction limit. One of the first SRM approaches that allowed the use of standard immunofluorescence (IF) sample preparation methods, conventional fluorophores and comparably simple widefield optics was Structured Illumination Microscopy (SIM). Here, a series of sinusoidal illumination patterns of different frequencies and/or orientations are used for excitation. The resulting Moiré fringe patterns have a lower detail frequency than the original structure and can therefore encode details below the diffraction limit, which can be retrieved mathematically by cross-computing multiple of the resulting images. A 2-fold resolution improvement was demonstrated both for lateral[98] and axial directions[99], however, a lateral resolution of ~100 nm is still insufficient to access the molecular imaging domain. Later iterations, such as saturated SIM, demonstrated higher resolution improvements, but at the cost of experimental simplicity[100].

In Stimulated Emission Depletion (STED) microscopy, a derivative of confocal microscopy[101], instead of illuminating the entire sample volume, a focussed laser beam is scanned over the sample and resulting fluorescence signal is captured with a sensitive point detector. The addition of two pinholes restricts both excitation and signal detection to a small volume within the sample and therefore increases axial resolution and the SNR by suppressing out-of-focus signal. To circumvent the resolution limit of standard confocal techniques, the sample-scanning excitation beam is superimposed with a doughnut-shaped depletion beam. The depletion beam induces stimulated emission in a defined area around the central excitation spot, which can be spectrally

separated from the remaining spontaneous fluorescence signal in its centre. By increasing the intensity ratio of the depletion doughnut over the excitation beam, detected fluorescence can be confined to a sub-diffraction-sized spot, whose position is precisely known from the beam position. Images are then reconstructed analogous to confocal microscopy[101], but with superior resolution[102]. While theoretically the volume of evoked fluorescence can be made arbitrarily small by further increasing the intensity ratio of the two beams, in practical terms lateral resolution is limited to ~50 nm by effects like photobleaching[103].

In conclusion, spatial fluorescence modulation methods are insufficient to routinely achieve molecular resolution as it is needed to investigate synaptic nanoarchitecture, e.g. individual SVs.

1.2.2.2 **Single Molecule Localisation Microscopy**

A second approach in SRM is to separate emitters temporally instead of spatially. These methods are summarised as Single Molecule Localisation Microscopy (SMLM), based on their common principle of how images are generated. The prerequisite for SMLM are fluorophores which can transition between two distinct, spectrally separable states. Instead of imaging the entire structure at once, at any given moment only a subset of fluorophores is switched into the detectable state, which creates isolated emission events, i.e. PSFs (Figure 1.5). The centre of gravity of these PSFs can then be mathematically approximated with high precision, e.g. with a Gaussian function, which yields the lateral coordinates at which the respective fluorophore is positioned. By acquiring a series of images of randomly distributed subsets of detectable fluorophores - such an image series typically being in a range of several tenths of thousands - the entire structure can be sampled. The list of coordinates is finally mapped onto a fine pixel grid (typically 10x10 nm) and rendered into a reconstructed, super-resolved image[104,105]. Provided a sufficient SNR is achieved, SMLM permits localisation accuracy of fluorophores up to the single digit nanometre range[104].

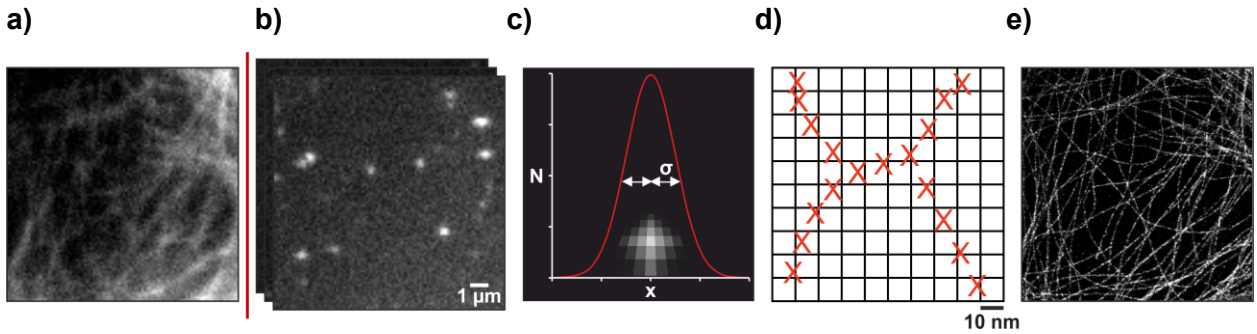

Figure 1.5 The principle of SMLM. In regular widefield fluorescence microscopy, the resolution of fluorescently labelled samples is limited by diffraction (**a**). By randomly cycling the fluorophores between an undetectable and a detectable state, subsets of isolated PSFs can be recorded (**b**). The centre of gravity (**c**: *x*) of these PSFs can be approximated with precision *σ*, dependent on the intensity *N*. Mapping the resulting coordinates onto a fine pixel grid (**d**) allows rendering of images with increased resolution (**e**).

The means by which SMLM techniques achieve temporal separation of emission, differ:

In Photoactivated Localisation Microscopy (PALM), the target protein is expressed as a fusion construct including a fluorescent protein. In its original state, this fluorescent protein does not exhibit fluorescence in the recorded spectrum of light. Upon irradiation with an activation laser of appropriate wavelength, a structural change in the conjugated π-system of the fluorophore is induced which shifts the fluorescence spectrum towards the imaging channel. By modulating the intensity of the activation laser, the density of detectable fluorophores can be controlled. The converted subset of fluorophores is then recorded and finally bleached to ensure sufficient spatial separation of emission events[106,107]. The stoichiometric labelling of target proteins by genetic fusion makes this technique ideal for molecular counting experiments (e.g. qPALM[108]). On the downside, the comparably weak intensity of fluorescent proteins limits the SNR and in turn the achievable resolution (see 1.2.2.5). In addition, the need for genetic fusion constructs limits its general application and requires individual validation experiments to ensure that the tandem protein behaves naturally.

While in PALM, the blinking of fluorophores is detrimental as it further reduces the intensity of PSFs and complicates the counting of target molecules, blinking fluorophores are the basis for *direct* Stochastic Optical Reconstruction Microscopy (*d*STORM). In contrast to PALM, *d*STORM typically employs synthetic fluorophores, which often are significantly brighter than fluorescent proteins. More specifically, fluorophores are selected that exhibit a strong tendency for intersystem crossing into the T_1 state (see Figure 1.4). Temporal separation of emission events is then achieved by submerging the sample in photoswitching buffer which contains reducing agents, e.g. primary thiols like β-mercaptoethanol or β-mercaptoethylamine (MEA), often with the addition of oxygen scavengers. The photoswitching buffer stabilises the triplet state of excited

valence electrons and therefore leads to long-lived dark states of the fluorophores. In the beginning of an image acquisition series, strong irradiation quickly populates the dark state. The excitation density and concentration of molecular oxygen in the imaging buffer are then used to set the equilibrium of fluorophores entering and returning from the dark state and therefore the emitter density during imaging[94,109,110].

In Points Accumulation for Imaging in Nanoscale Topography (PAINT), instead of controlling the emission state of a fluorophore, two distinct kinetic states are used to create detectable emission events. Fluorophore-bound or inherently fluorescent labels (e.g. transferrin or Nile red, respectively) are freely diffusing in solution, where the constant emission is distributed over a wide area, thus merging with the background. The binding of said labels to their target structures momentarily seizes mobility and causes the accumulation of photons, leading to a corresponding localised spike in intensity whose PSF can be recorded. Dynamic unbinding or bleaching of the immobilised fluorophore completes the “blinking” cycle. Since the probability of a binding event scales linearly with the concentration of labels in solution, control of the detectable emitter density is straight-forward[111]. Reversible binding approaches offer the advantage of neglectable bleaching since the labels are constantly exchanged from the suspended pool. Later iterations of PAINT utilise of complementary single-stranded DNA oligonucleotides (DNA-PAINT), which allows tuning of the binding characteristics through DNA sequence design and therefore uncouples PAINT kinetics from the binding characteristics of the employed label[112]. Multiple approaches have also tackled the issue of high label concentrations that are needed for fast sampling rates, but also raise the background and therefore lower the SNR. Total Internal Reflection Fluorescence (TIRF) illumination drastically reduces out-of-focus background but simultaneously restricts the imaging depth to ~100 nm from the cover slip[113]. Fluorogenic[114] or self-quenching[115] imager strands, on the other hand, aim to reduce fluorescence emission of unbound labels. Commercial availability of DNA-PAINT constructs is still limited, though.

Common to all SMLM techniques is the time-consuming image acquisition, compared to standard widefield, but also modern scanning microscopy techniques. However, recent computational advancements in the field of artificial intelligence (AI) allow image reconstruction from recordings with significantly higher emitter densities and have led to a drastic acceleration of SMLM image acquisition[116,117]. On the downside, the black-box nature of AI requires careful validation of obtained images with ground-truth data.

1.2.2.3 **Minimal Flux Microscopy**

The latest microscopy developments like Minimal photon Fluxes (MinFlux) or single-molecule localization by RASTer scanning a MINimum of light (RASTMIN) combine the stochastic blinking of SMLM with a doughnut-shaped laser beam similar to the one used in STED microscopy. Converse to the STED beam, in minimal flux microscopy the excitation part is arranged around the centre of the beam while the centre itself stays unilluminated. The exact position of a fluorophore is now located by circling the excitation beam around its suspected position until the fluorophore coincides with the dark centre of the beam and fluorescence reaches a minimum; hence the term minimal flux microscopy. Accordingly, the optical resolution depends on how narrow the central zero-excitation spot can be, which is limited by the feasible intensity steepness of the doughnut flanks. Localisation accuracy up to 1 nm has been demonstrated[118]. The targeted detection process significantly increases imaging times and therefore decreases the practical field of view (FOV), and, to date, in our hands, dual-colour 3D acquisitions were not routinely achieved (data not shown).

1.2.2.4 **Accessing the Third Dimension**

In theory, both the lateral and axial position of a fluorophore are directly encoded by the recorded PSF. As mentioned above, the centre of gravity of a PSF accounts for its lateral position. In addition, the width of a PSF is proportionate to the axial distance of the fluorophore to the focal plane. In practical terms, axial localisation is complicated by the symmetry of the PSF on both sides of the focal plane. The straightforward solution would be to position the focal plane at a known edge of the sample, e.g. the cover slip[119]. However, this approach restricts the imaging volume to half of the microscope's capability. Multiple solutions that maintain the axial imaging volume by breaking the focal symmetry have been reported, among them biplane[120,121], double-helix[122] and astigmatism-based approaches[123]. The latter has the advantage of a comparably straightforward implementation both into the optical setup as well as the postprocessing pipeline and was chosen for the maS³TORM setup.

Astigmatism is introduced in the emission path of a microscope by the addition of a long focal-length cylindrical lens. As a result, two separate focal planes are created for light focussed along the x- and y-axis, respectively (Figure 1.6a). At the midline between these new focal planes, the PSF appears symmetrical. Moving away from it, the PSF is defocussed mainly along one of the two lateral axes and changing direction when crossing the midline. With the help of appropriate calibration curves, also called sigma tables, the Full Width at Half Maximum (FWHM or σ) of the

fitted Gaussian is used to determine the axial position of the respective emitter (Figure 1.6b), typically with a localisation accuracy of up to ~20 nm.

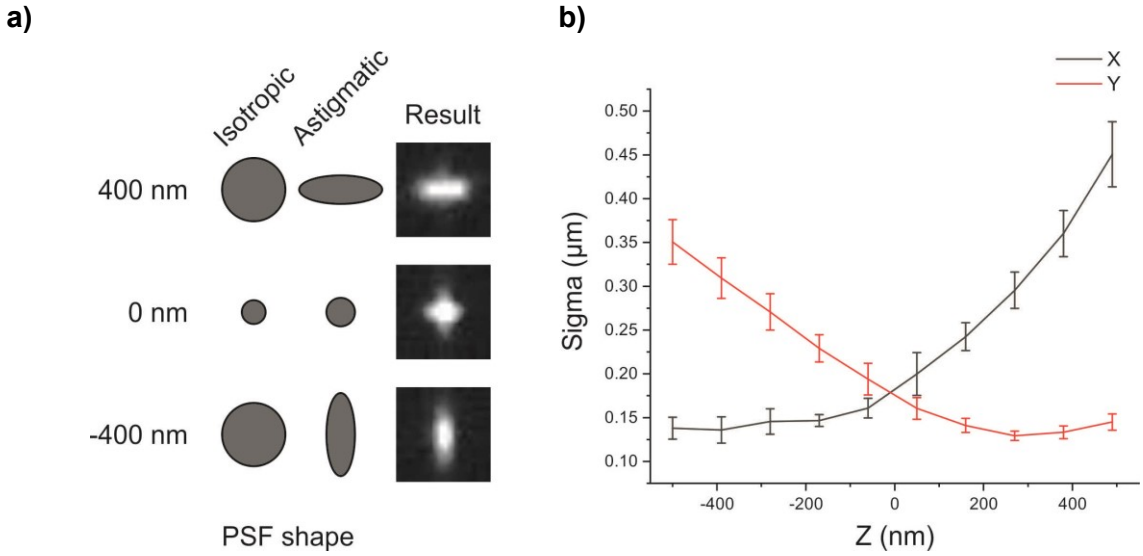

Figure 1.6 Astigmatism enables 3D emitter localisation. The issue of symmetry of the PSF dimensions on both sides of the focal plane is resolved by the addition of a cylindrical lens in the detection path of the microscope, which introduces astigmatism (**a**). Using a calibration or sigma curve, the PSF dimensions are related to an axial position (**b**).

1.2.2.5 The Redefinition of Resolution in SMLM

Since in SMLM the resolution of the resulting image, i.e. the minimum distance at which separate emitters can be identified as such, is no longer directly dependent on the optical resolution of the microscopy system, the term “resolution” in SMLM needs to be redefined. A common approach is to use the uncertainty of a target position as the resolution criterion. This target uncertainty is dependent on two main contributions: as in fluorescence microscopy the position of a fluorophore is mapped instead of the true position of the target, the label-dependent distance between the target and the fluorophore, known as linkage error, dictates a spatial limit of precision. In addition, the localisation precision at which the centre of gravity of a PSF can be located, needs to be considered. The latter is again dependent on two main factors: the quality of the optical setup, represented by the standard deviation of the Gaussian approximator σ, and the number of collected photons per emission event N. In cases of high SNR, where background can be neglected, the complex derivation from Mortensen *et al.*[124] for the localisation accuracy Δx can be simplified to **Equation 3**[94]:

$$\Delta x = \frac{\sigma}{\sqrt{N}} \qquad \textbf{Equation 3}$$

In addition to the accuracy, the practical resolution is also dependent on the sampling rate, i.e. the labelling efficiency or label density for a certain target. According to the Nyquist-Shannon sampling theorem, the label frequency needs to be at least twice the desired resolution to accurately depict the structure of interest[125,126]. This is especially relevant for continuous or periodic structures like cytoskeletal filaments or membrane constituents, but also for targets with dimensions well above the achieved resolution such as the cytomatrix proteins Bassoon and Piccolo, in case primary antibodies (pABs) only bind in a single location[104].

1.2.3 Multiplexed Imaging

To determine the spatial relation of a set of targets, ideally all targets should to be imaged within the same sample to allow meaningful correlation. In standard multicolour SMLM this restricts the number of addressable targets to a maximum of four separable colour channels (typically blue, green, orange and red)[127]. In practical terms the availability of separate channels is often further restricted to two[128,129] or three[130,131] targets. Since excitation and emission spectra regularly have a width of 100 nm and above, a corresponding distance between individual colour channels needs to be kept to avoid cross-talk. This broad spacing, on the other hand, renders multicolour imaging prone to chromatic aberrations due to the effects of refraction (Figure 1.7a). Modern achromatic or apochromatic optics account for chromatic aberrations of two or ≥3 reference wavelengths, respectively, (Figure 1.7b). However, although the remaining error of typically ≤ 50 nm is neglectable in diffraction-limited microscopy, in SRM it can cause relevant image artefacts[132].

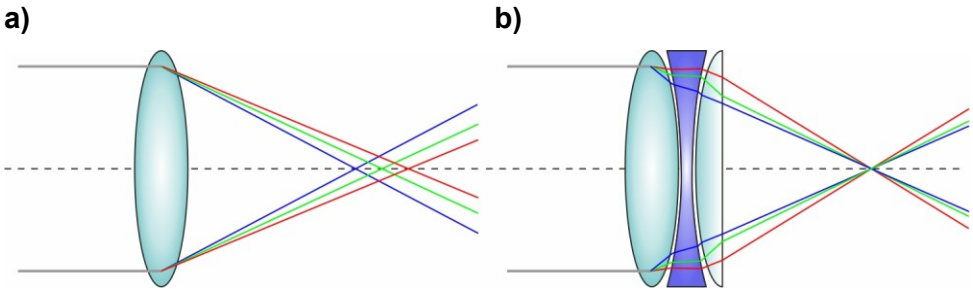

Figure 1.7 Apochromatic lenses avoid the chromatic aberration of standard lenses. Due to the effect of refraction, the focal plane of a standard lens is dependent on the wavelength of light (a). The combination of multiple lenses of different glass compositions and the possible addition of glass coatings allows construction of apochromatic lenses, which compensate for refraction and create a virtually identical focal plane across the visible spectrum.

Spectral Demixing (SD) elegantly circumvents the issue of chromatic aberrations for multicolour SMLM by employing two or more spectrally close, but not identical fluorophores which are simultaneously imaged. The emission signal is split onto two detectors through the insertion of a dichroic mirror in the emission path of the microscope (Figure 1.8). The resulting pairs of recorded

PSFs display a distinct intensity ratio that depends on the position of the beam splitter relative to the respective emission spectrum of the fluorophore and therefore allows ratiometric separation of the fluorophore species into multiple colour channels[133]. The need for spectral as well as experimental compatibility (e.g. buffer composition and imaging conditions) limits the range of fluorophores that are applicable to SD.

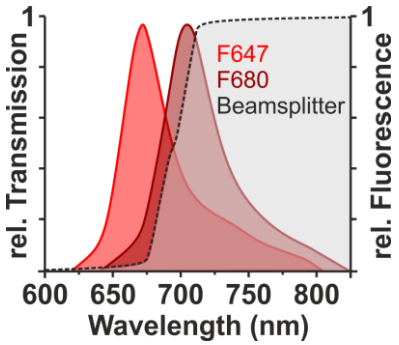

Figure 1.8 Example of suitable emission spectra for Spectral Demixing. Hypothetical emission spectra of two red-emitting fluorophore species and a corresponding beam splitter that allow ratiometric separation via SD.

Experiments that require correlation of more than the aforementioned two to four spectrally separable targets necessitate sequential labelling and imaging. Multiple approaches have been published in recent years, among them multiplexed antibody size-limited *d*STORM (madSTORM)[134], exchangePAINT[135,136] and others[137,138], each with their own advantages and drawbacks. With the multiplexed automated serial staining STORM (maS³TORM) microscope, our group has developed an independent approach for sequential multiplexed *d*STORM imaging[92]. It combines a SD- and 3D-capable, fully automated *d*STORM microscope with a pipetting robot to enable label removal and restaining (see 2.2.4.2 for details). I validated the label removal strategy, which is summarised in Figure 1.9 and Figure 1.10.

To avoid cross-talk between consecutive staining rounds (SRs), previously applied labels need to be removed from the sample before a new set can be introduced. In situations where pAB host species are going to be repeated throughout the experiment, it is necessary to remove the bound antibodies altogether which can be achieved by chemical elution. In our hands a solution of 0.1% SDS at pH 13 proved to be most efficient without compromising the sample's structure and integrity exceedingly (Figure 1.9a). Elution efficacy as well as structural degradation increased with incubation time, hence we chose an incubation time of 15 min as a suitable compromise (Figure 1.9b). As our elution paradigm only reached an efficiency of ~95%, an additional bleaching step is required. For labels that will not be detected by secondary antibodies (sABs) used in later SRs, such as lectins or directly labelled NBs, chemical elution can be omitted in favour of sample integrity. Bleaching efficacy did not significantly change with irradiation durations so we chose

4 min to ensure reliable signal suppression while minimising negative effects on the sample (Figure 1.9c).

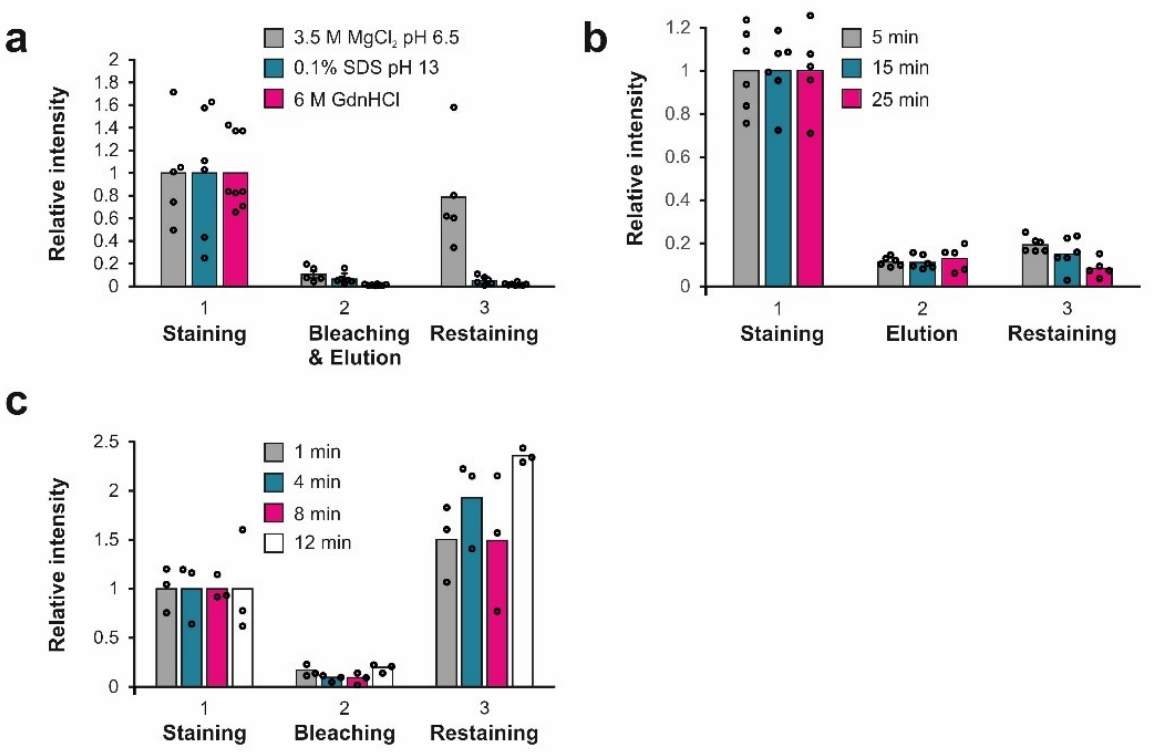

Figure 1.9 Validation of label removal between staining rounds by chemical elution and bleaching. The efficacy of primary label removal with different elution buffer compositions was tested (**a**). Dependence of the label removal on elution times (**b**) and bleaching times (**c**) was evaluated for the SDS buffer composition. (from Klevanski, Herrmannsdoerfer, Sass et al., 2020[92]).

We tested the effects of chemical elution both in PFA-fixed U2OS cell cultures as well as brain tissue sections and found an average loss of overall target immunofluorescence (IF) of ~2.7% and 4.1% per SR, respectively (Figure 1.10a+c), which was measured by reapplying the same pAB/sAB combination after elution and bleaching for a total of 10 SRs (Figure 1.10b+d). Sample integrity was assessed using cross-correlation analysis and revealed no significant structural changes over the course of 10 SRs (Figure 1.10e+f)

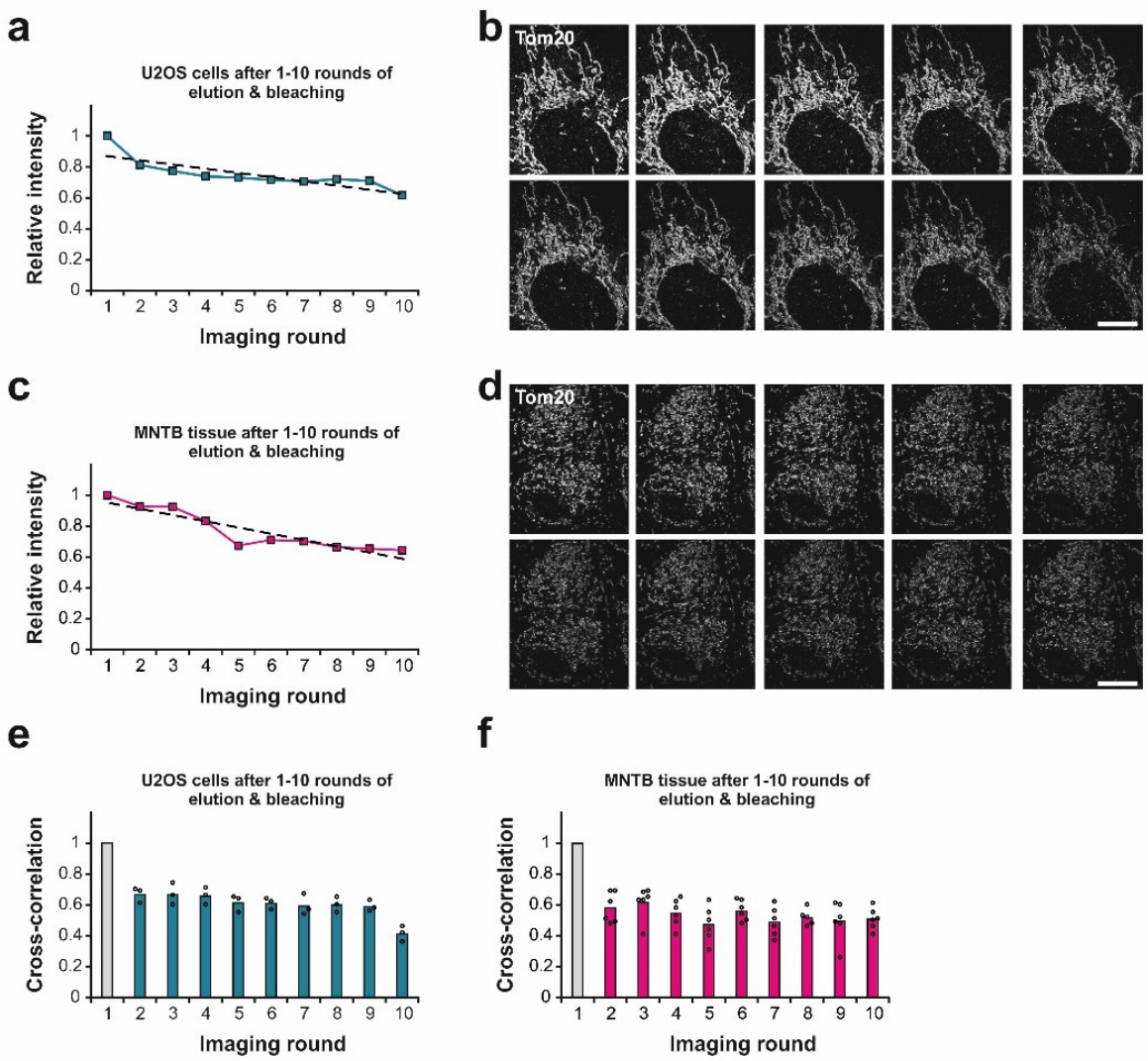

Figure 1.10 Effects of elution procedures on sample integrity. Loss of epitopes from elution and restaining was tested in U2OS cell culture (**a+b**), as well as brain tissue sections (**c+d**) by repeatedly staining for Tom20. Sample integrity was tested by cross-correlation analysis (**e+f**). (from Klevanski, Herrmannsdoerfer, Sass et al., 2020[92]).

1.2.4 The Label Strategy Determines the Linkage Error

As mentioned above (see 1.2.2.5), the resolution of SMLM images, i.e. the localisation precision, can be influenced in two ways: by increasing the localisation accuracy of the PSF, e.g. through an increase in the photon budget available for emitter localisation, or by decreasing the linkage error. However, current iterations of SMLM have already been optimised already and leave little potential for further accuracy enhancement, especially in the case of minimal flux approaches. This highlights the importance of the label choice for optimal imaging results. A multitude of labels

is readily available these days, which permit a significantly smaller linkage error than the conventional indirect IF approach (Figure 1.11). Future developments, like aptamers[139], might allow a further reduction of label sizes and promise a rational design of labels.

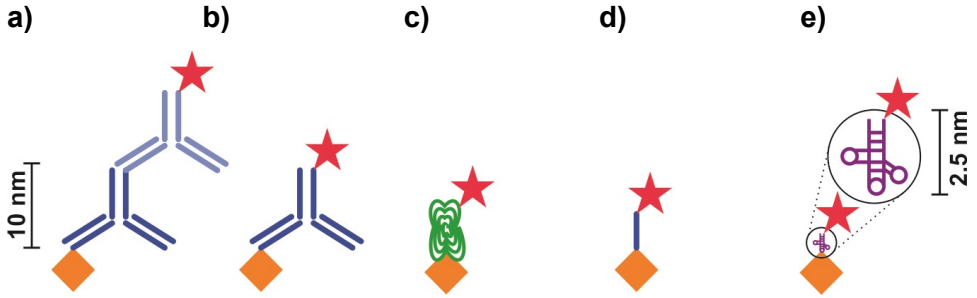

Figure 1.11 Labelling approaches ordered by potential linkage error. The linkage error describes the probable distance between the binding location of a label (e.g. the epitope) marked in **orange** and the fluorophore (**red star**). The popular indirect IF approach employs both a pAB and sAB (**a**), which doubles the potential linkage error of directly conjugated IgG antibodies of ~10 nm[140] (**b**). The majority of protein tags[141,142], toxins[143] or lectins[144] can be expected to be significantly smaller, in a range ≤5 nm (**c**). Single-domain camelid antibodies, better known as nanobodies[145], have a reported size of ~ 4 nm (**d**). Oligonucleotide-based labels such as aptamers[139] (under-) match the size of the smallest protein binders (**e**). Labels are drawn to scale. Size estimates for **c** are predominantly based on molecular weight conversion[146].

1.3 Rationale

1.3.1 Technical Challenges

Highly multiplexed, super-resolved image sets have not been routinely achieved yet, especially not from tissue samples. While our maS³TORM microscope offers comparably easy access to the domain of multiplexed imaging, finding the right parameters for sample preparation and restaining procedures as well as suitable labels that perform reasonably well in a mutual sample preparation is challenging. In addition, to date, analysis pipelines for such data sets have not been established.

1.3.2 Biological Questions

Substantial evidence points towards molecular markers to convey SV pool identity. However, it is still unclear whether the functionally observed SV pools truly are homogeneous groups of SVs, which marker or markers are representative for each pool and if these markers are solely present on SVs for tracking purposes or rather engage in “regular” synaptic functions and structure SV populations through “off-target” effects (e.g. SNAP25) or dissimilar interactions (e.g. VAMP1 vs. VAMP2).

In addition, from a point of energy homeostasis it is still conceivable that SVs are spatially sorted but in a probabilistic fashion, where aged or otherwise tagged SVs that are not participating in the SV cycle anymore, or lack a specific interaction partner for other reasons, are displaced outwards from the AZ by actively recycling SVs. Under physiological stimulation, the energy demand of a counteracting active transport of “unsuitable” SVs back towards the AZ has no supposable benefit for the synapse and thus appears unlikely[147,148]. If or to which extent this predicted passive spatial sorting exists *in vivo* has not been determined yet.

Lastly, the question remains whether different types of synapses are equipped with similar SV pools, if present pools are structured comparably and if pool identity is conveyed by a common set of molecular markers or different proteins have homologous functions with respect to pool formation.

1.3.3 Hypothesis

I hypothesised that multiple subsets of SVs are each tagged with a pool-specific marker protein and spatially sorted with respect to the adjacent AZ. I investigated this hypothesis with highly multiplexed SRM and image-based spatial correlation analyses. Hypothetical protein distributions as they might be observable as a consequence of my hypothesis are shown in Figure 1.12:

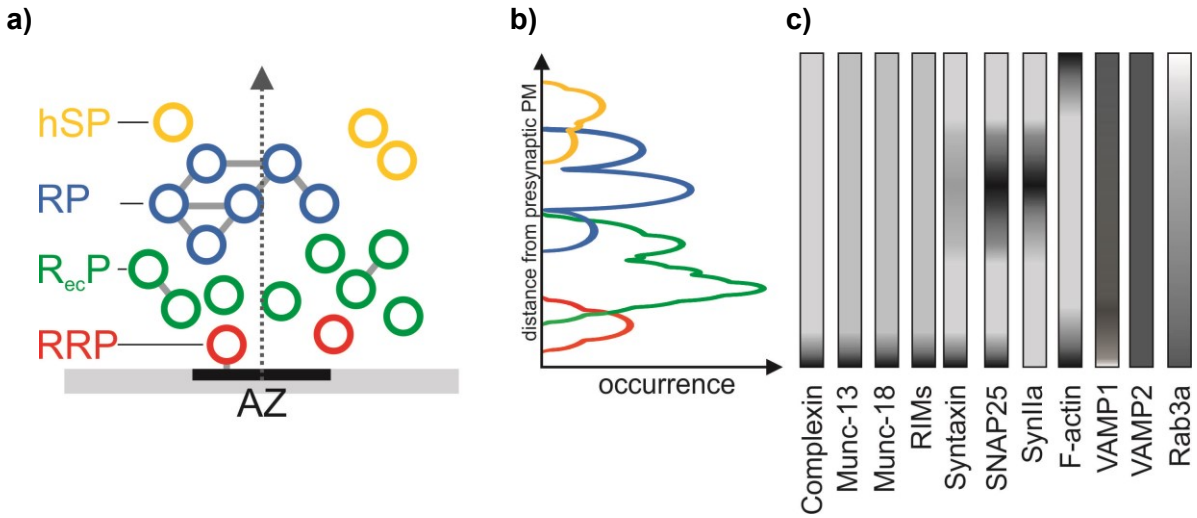

Figure 1.12 A hypothetical protein distribution in marker-dependent SV pools. The SV population is suggested to be divided into a readily releasable pool (RRP), recycling pool ($R_{ec}P$), resting pool (RP) and a hypothetical super pool (hSP) (**a**). Assuming some level of spatial organisation exists, orthogonal line profiles (**b**; corresponding to dotted arrow in **a**) would be suited to capture the pool distribution along the transverse axis of the presynaptic compartment. Proteins which only partially correlate with the SV distribution might represent candidates for molecular pool markers (**c**). (modified from Maja Klevanski)

2. Materials and Methods

2.1 Materials

Table 2.1: Reagents

Name	Product number	Manufacturer
Cacodylic acid buffer (pH 7.4)	5169.2	Roth
Dimethyl Sulfoxide (DMSO)	3176/25ML	Tocris Bioscience
1-Ethyl-3-(3-dimethylaminopropyl)carbodiimide (EDC)	034449-1G	Sigma Aldrich
Potassium hydroxide (KOH)	30603	Sigma Aldrich
Mercaptoethylamine (MEA)	M6500-25G	Sigma Aldrich
2-(N-morpholino)ethanesulfonic acid (MES)	M3671-50G	Sigma Aldrich
Methylcellulose	M6385-100G	Sigma Aldrich
N-Hydroxysulfosuccinimid (sulfo-NHS)	56485-1G	Sigma Aldrich
PBS	14040091	Gibco
Paraformaldehyde (PFA)	16005	Sigma Aldrich
Poly-L-lysine (PLL)	P4832-50ml	Sigma Aldrich
Sodium Dodecyl Sulfate (SDS)	39575.01	Serva
Sucrose	84097	Sigma Aldrich

Table 2.2: Materials

Name	Product number	Manufacturer
Glass bottom dishes	P35G-0-14-C	MatTek Life Sciences
Gold Nanoparticles (100 nm)	A11-100-NPC-DIH-1-50	NanoPartz Inc.
Gold Nanoparticles (150 nm)	742058-25ML	Sigma Aldrich
NV^- Nanodiamonds	NDNV100nmHi2ml	Adamas Nanotechnologies
TetraSpeck™ Microspheres	T7279	Invitrogen

Table 2.3: Antibodies and labels

Antigen	Host	Product number	Manufacturer
Bassoon	mouse (kappa)	SAP7F407	Enzo Life Sciences
CHC17-AF647	mouse	NB300-613AF647	Novusbio
eGFP	chicken	ab13970	Abcam
Homer1bc	rabbit	160 023	Synaptic Systems
Piccolo	rabbit	142 113	Synaptic Systems
Rab3a	mouse (kappa)	107 111	Synaptic Systems
SNAP25	mouse (kappa)	111 111	Synaptic Systems
SV2abc	mouse	AB2315387 Supernatant	DSHB
Synapsin2	mouse (kappa)	106 211	Synaptic Systems
Synaptophysin	rabbit	101 002	Synaptic Systems
Tom20	rabbit	sc-17764	Santa Cruz Biotech
VAMP1	rabbit	104 002	Synaptic Systems
VAMP2	rabbit	104 008	Synaptic Systems
vGluT1	Guinea pig	AB5905	Millipore
vGluT1-CF680	camelid	Custom conjugation	NanoTag Biotech
vGluT2	chicken	135 416	Synaptic Systems
Secondary	**Conjugation**	**Product number**	**Manufacturer**
anti-chicken	AF647	A21499	Invitrogen
anti-Guinea pig	AF647	A21450	Invitrogen
anti-mouse	CF680	SAB4600199	Sigma Aldrich
anti-mouse	AF647	A21235	Invitrogen
anti-mouse (IgG1)	Atto647n	N2002-At647N-S	NanoTag Biotech
anti-mouse (kappa)	CF680	N1202	NanoTag Biotech
anti-rabbit	AF647	A21245	Invitrogen
anti-rabbit	CF680	SAB4600362	Sigma Aldrich
Lectin	**Conjugation**	**Product number**	**Manufacturer**
PSA	AF647	21511543	BioWORLD
WGA	AF488	W11261	Thermo Fisher
WGA	CF680	29029	Biotium
Virus	**Plasmid**	**Batch**	**Manufacturer**
rAAV	pAM-CAGprom-eGFP	889 (419)	in-house

2.2 Methods

2.2.1 Fiducial Immobilization Development

Experiments were conducted using 100 nm nitrogen-vacancy (NV^-) Nanodiamonds (ND), 100 nm Tetraspecks (TS) and two variants of readily available gold nanospheres (GB): 100 nm particles with carboxyl surface modifications (GB_{100}) where experimental focus lay on the immobilization capability and 150 nm non-carboxylated particles (GB_{150}) where SNR was prioritized.

2.2.1.1 Spectra Acquisition

Excitation and emission spectra of ND and the far-red component of the TS were acquired from the respective manufacturers. GB_{150} excitation spectra were provided by Dr. Jörg Malsam and recorded on an Ultrospec 2100 pro UV/Vis spectrometer (GE Biochrom Amersham Biosciences), using a 1:10 dilution in ddH_2O. GB_{150} luminescence spectra were provided by Franziska Grün and recorded using a Jasco FP6500 spectrofluometer (JASCO Corporation), using a 1:10 dilution in ddH_2O. The spectra were recorded using 560 nm and 660 nm laser lines at a photomultiplier gain value of 300, recording an emission range from 10 nm above the respective laser line to 900 nm.

2.2.1.2 Initial EDC coupling protocol

Glass bottom dishes were coated with 250 µl PLL for 15 min at room temperature and washed once with PBS. Fiducials were diluted 1:250 in 0.5 M MES buffer containing 6.5 mM EDC and 38 mM NHS. 320 µl of fiducial suspension were added per glass bottom dish and incubated for 15 min at RT. The solution was carefully removed and immediately replaced with 320 µl of identical buffer without the addition of fiducials for 45 min at RT. Finally, the dishes were washed twice with ddH_2O and left in a dust-free environment until dry. Prepared dishes were stored at 4°C until use.

2.2.1.3 Intensity Tracking

Samples were generated containing either ND, TS or GB_{100}. To compare signal strength with different excitation and emission channel combinations, isolated fiducials were imaged using the 561 nm or 661 nm excitation at ~0.3 kW/cm² (10%) and orange or red emission channels. 10 frames were recorded at 5 Hz. For each excitation/emission combination 5 field-of-view (FOV) were recorded, analysed with rapidSTORM 3.3 and averaged.

To test for signal persistence in a *d*STORM regime, FOV with multiple well-isolated fiducials (ND, TS or GB_{150}) were chosen and imaged using the 661nm excitation at 2.7 kW/cm² (100%) and red

emission channel at 10 Hz for 36 000 frames, resulting in 1 h of recording time. 5 individual fiducials were cropped from the image stack using Fiji, analysed in rapidSTORM 3.3 and averaged. Localisation precision was calculated for the first and last 300 frames (30 sec) as the average vector length of the coordinate delta in adjacent frames.

2.2.1.4 **Cluster Analysis**

ND were immobilised onto coverslips following either a protocol derived from the Merck-Millipore Application Note on EDC coupling[149] or my revised strategy as detailed in 2.2.2.1. To assess the fiducials' tendency for aggregation, samples were imaged using the 561 nm excitation at 0.3 kW/cm², red emission channel and a frame rate of 5 Hz. To account for brightness differences of the ND[150], cluster size was measured by thresholding the images in Fiji[151] using the "Triangle dark" pre-set. Selections were converted into masks and cluster areas were measured. To convert cluster areas into particles per cluster I have reasoned that a histogram of cluster size is most likely to follow an exponential decay function. This would result in a cluster size of one particle per cluster being the most abundant cluster form even in an aggregate-prone environment. Therefore, the median area can serve as rough estimate for the size of a single particle and the total area per cluster was normalised to the median cluster size accordingly.

The revised protocol 2.2.2.1 was also tested on GB_{100} and TS. Image frames were recorded using the 661 nm excitation and red emission channel with otherwise identical parameters. Analysis was carried out as described above.

Significance was tested in GraphPad Prism 10.2.2. via unpaired t-test. Significance is denoted as: $p \leq 0.05$ (*), $p \leq 0.01$ (**), $p \leq 0.001$ (***), $p \leq 0.0001$ (****).

2.2.1.5 **Dilution-to-Density Analysis**

To calculate the average fiducial density at different dilutions, ND samples were prepared at dilutions of 1:5 000, 1:8 000 and 1:10 000. 15 FOV from two independent samples each were recorded per condition as described in 2.2.1.4, analysed with rapidSTORM 3.3 and the total number of detected localizations per FOV was averaged. An exponential decay was fitted to the data to create the trend line.

At a pixel size of ~125 nm and a resolution of 512 pixels squared our camera covers a sample area of ~4100 µm².

2.2.1.6 Registration Precision and Mechanical Resilience

Samples were generated containing either ND, GB_{100} or TS. For each sample 5 FOV of isolated fiducials were imaged with suitable fiducial parameters in line with 2.2.4.3: ND and PB: 561 nm excitation/GB: 661 nm excitation at 0.3 kW/cm², red emission channel, 5 Hz for 10 sec. After the initial image acquisition, utilising the integrated pipetting robot samples were washed 10 times with 300 µl PBS and then imaged again. The procedures were repeated 10 times resulting in 100 washing steps between the first and last image acquisition. Images were analysed with rapidSTORM 3.3 and consecutive image stacks were registered using the 3D-Transformer Matlab script created by Maja Klevanski (see 2.2.5.1). The standard deviation of fiducial positions between rounds was extracted and averaged as a measure for fiducial displacement and localisation precision.

2.2.2 Sample Preparation

Detailed procedures are published in Klevanski, Herrmannsdoerfer, Sass et al., 2020[92].

2.2.2.1 Fiducial Application

EDC was mixed into DMSO at a concentration of 1 M, aliquoted and stored at -20°C until use.

Glass bottom dishes were coated with 250 µl PLL for 15 min at room temperature and washed once with PBS. Fiducials were diluted in ddH_2O at concentrations of 1:8 000 (ND, TS) or 1:250 (GB) and agitated vigorously. 250 µl of fiducial suspension was added per glass bottom dish and incubated for 15 min at RT. The solution was carefully removed and immediately replaced with 320 µl of 5 mM EDC in 50 mM MES buffer (pH 6 in ddH_2O) for 45 min at RT. Finally, the dishes were washed twice with ddH_2O and left in a dust-free environment until dry. Prepared dishes were stored at 4°C until use.

2.2.2.2 Animal Experiments

Experiments in this section were performed in compliance with German animal welfare guidelines as approved by the Regierungspraesidium Karlsruhe under animal grant 35-9185.81/G-214/20.

Anesthetized Spraque Dawley rats (Charles River) were transcardially perfused with ~20 ml PBS and 4% PFA in PBS, respectively. Perfusion was performed at P12-P13 or P21, depending on the experimental aims (see Table 7.1 for details).

2.2.2.3 Tissue Processing

The isolated brains were post-fixed in 4% PFA in PBS for 24 h at 4°C and then sliced into 200 µm sections on a SLICER HR2 vibratome (Sigmann-Elektronik). The MNTB region was excised and transferred into cryo-protection buffer (2.1 M sucrose in 0.1 M cacodylic acid buffer (pH 7.4)) for a minimum of 1 h at RT.

2.2.2.4 Cryo Sectioning

Freeze-protected tissue blocks were placed on sample holders, shock-frosted in liquid nitrogen and ultra-sectioned into ~300-400 nm thick slices on an Ultracut S cryo-ultramicrotome (Leica), following the procedures established by Heinz Horstmann[152,153], a modification of the Tokuyasu technique[154,155]. Slices were picked up with a metal loop in 1.15 M sucrose and 1% methylcellulose in 50 mM cacodylic acid buffer, transferred onto coated glass bottom dishes (see 2.2.2.1) and stored at 4°C until use.

2.2.2.5 Staining

Staining was performed at room temperature and samples were imaged immediately after preparation or stored in PBS at 4°C for a maximum of 24 h. Samples were washed with PBS three times for a minimum of 15 min each to remove the sucrose/cacodylic acid storage buffer and an additional three times for 5 min each between all consecutive steps. Since our ultra-sectioning[92,152]technique ensures sufficient access to the lumen of Calyx neurons, an initial permeabilisation step is not required[153]. Blocking buffer (5% FCS in PBS) was applied for 20 min, followed by the pAB and sAB dilutions in 0.5% FCS in PBS for 45 min, each. AB combinations were chosen according to experimental aims (see Table 7.2 - Table 7.4 for details).

2.2.3 GFP Transductions

2.2.3.1 Animal Experiments

Experiments in this section were performed in compliance with German animal welfare guidelines as approved by the Regierungspraesidium Karlsruhe under animal grant 35-9185.81/G-196/21.

At P2 the sinistral VCN of Spraque Dawley rats (Charles River) was injected with a total of 2 µl of pAM-AAV-CAG-eGFP solution at 5 injection sites following the procedures established in Wimmer *et al.,* Pfluegers Archive, 2004[156]. Injections were performed by Marion Schmitt. Animals were transcardially perfused at P13 and samples were generated as described in 2.2.2.2ff. Injection coordinates are provided in Table 2.4:

Table 2.4 Viral injection coordinates

x	-y	z	depth
0.7	7.2	0.3	6.5
0.7	6.8	0.3	6.4
0.7	6.4	0.3	6.5
0.9	6.6	0.35	6.5
0.9	7.0	0.35	6.5

2.2.4 Imaging

2.2.4.1 Widefield Microscopy

Whole-slide images of brain sections from GFP-transduced animals were screened on a Leica DM6000B widefield microscope, equipped with an Andor-Neo-SCC02104 sCMOS camera and HC PL FLUOTAR 1.25x/0.04 DRY objective. Samples were excited by LED at 470 nm and images were acquired in the 525/50 nm emission channel. Excitation intensity and exposure times were matched to the sample's GFP expression level. Pixel size was 6.5x6.5 µm.

2.2.4.2 massSTORM Microscope

For dSTORM experiments the maS³TORM microscope, which was developed and built in-house and is published in Klevanski, Herrmannsdoerfer, Sass *et al.,* 2020[92] (for further details see Herrmannsdoerfer, 2017[157]), was used. The microscope is equipped with four laser lines (405 nm, 488 nm, 561 nm and 661 nm) which will be referred to accordingly. The corresponding emission channels will be addressed as follows (Table 2.5):

Table 2.5 maS³TORM emission channels

Channel designation	Filter properties
Green	525/45
Orange	605/50
Red	700/75

The layout and major components are described in Figure 2.1. The microscope is controlled by a three-part software: the pipetting robot is operated by its commercial Chronos™ software package and the optical components are controlled via micromanager 1.4.22[158]. To enable communication

between these two layers and to allow multiplexed experiment automation, a Java (Sun Microsystems) -based GUI and experiment editor was created by Frank Herrmannsdoerfer[157].

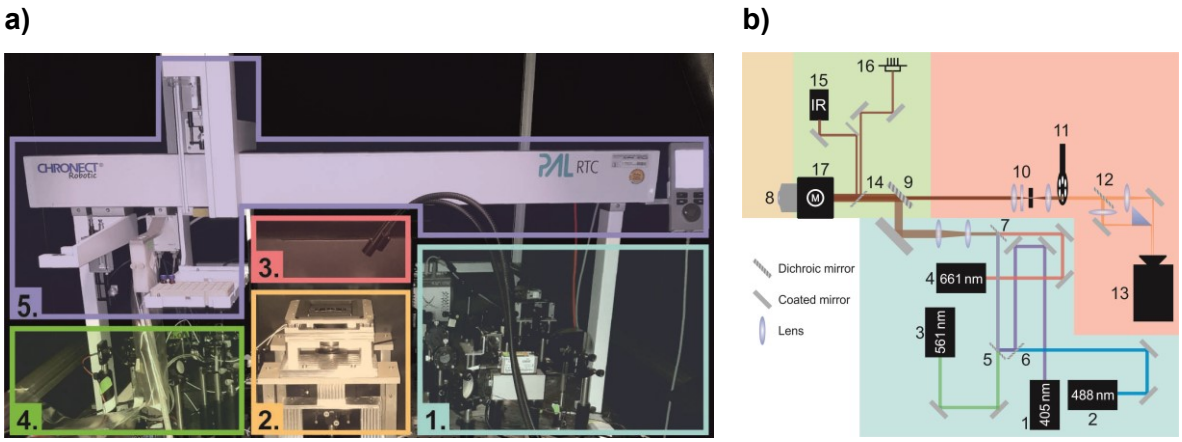

Figure 2.1 maS³TORM microscope overview. The maS³TORM microscope integrates two main functionalities into a coordinated setup: a free-space *d*STORM microscope (**a**, 1-4) and a pipetting robot (**a**, 5). The excitation part (**a**, 1) consists of a four-laser excitation pathway (405 nm, 488 nm, 561 nm, 661 nm; **b**, 1-4) which is conjoined using a series of dichroic mirrors (**b**, 5-7) and focused onto the back focal plane of a UAPON 100x OTIRF oil immersion objective (Olympus; **b**, 8). Underneath the sample stage (**a**, 2) a quad-bandpass filter (**b**, 9) separates the excitation light from the emission signal, which is then guided into the emission box (**a**, 3). Here, the signal passes through an aspherical lens (**b**, 10) to introduce astigmatism-based 3D resolution, the emission filter wheel (**b**, 11) as well as a second dichroic mirror (**b**, 12) that splits the emission signal onto two side-by-side areas of the EMCCD camera (**b**, 13) for ratiometric-based SD. A third dichroic mirror (**b**, 14) that is located underneath the objective is used to feed an IR beam (**b**, 15) of the focus stabilization system (**a**, 4) into the objective. The IR beam is passing through the objective in a total internal reflection configuration and therefore horizontally translates in an axial position-dependent manner. The positional shift of the exiting beam is then captured on a quadrant diode (b, 16) and provides feedback for the axial objective position piezo motor (**b**, 17) to counteract sample displacement. Incorporated into the microscope is a PAL3 RTC pipetting robot (Axel Semrau; **a**, 5), equipped with both a 100 µl and 1000 µl pipette, a washing station with access to ddH_2O and PBS, as well as a 1.5 ml vial tray with a 54 vial capacity. The vials are used to provide blocking, antibody and elution solutions as well as photoswitching buffer components during maS³TORM experiments. (modified from Klevanski, Herrmannsdoerfer, Sass et al., 2020[92])

2.2.4.3 Image Acquisition (*d*STORM)

*d*STORM imaging was conducted in photoswitching buffer consisting of 100 mM MEA in PBS (pH 8). Before each imaging session photoswitching buffer was freshly prepared from dry MEA aliquots that were stored under argon at -20°C for long-term storage, then at 4°C between imaging sessions to ensure optimal photoswitching efficacy.

To aid in region of interest (ROI) selection, a tile scan of all present tissue sections was conducted using the 661 nm excitation and red emission channel at ~30 W/cm² (1%) and a frame rate of 5 Hz. Before each *dSTORM* acquisition, using identical parameters, an additional conventional fluorescence widefield image of the respective ROI was acquired. For *d*STORM imaging the 661 nm excitation was increased to ~2.7 kW/cm² (100%) 10 seconds before the start of the

acquisition. A TIFF stack of 20 000 frames was recorded at a frame rate of 33 Hz. After each *d*STORM acquisition a widefield image series was acquired with the 561 nm excitation and the red emission channel at 0.3 kW/cm² (10%) and 5 Hz for 10 sec to generate fiducial images for ROI registration purposes. Acquiring the fiducial images in succession to the *d*STORM acquisition has the advantage that the majority of the target signal within the ROI is either bleached or remains in the dark state, thus enabling a higher SNR.

Emitter positions were analysed using an automated version of rapidSTORM 3.3[159] and saved as text files, from here on referred to as localisation files.

2.2.4.4 Multiplexing Procedures

Samples were manually stained as described in 2.2.2.5, mounted onto the microscope and 300µl of photoswitching buffer was added. ROIs were selected from the tile scan with sufficient spacing to ensure non-overlapping excitation areas (~100 µm centre-to-centre) and imported into the experiment editor. After the initial imaging round, labels were removed using SDS-mediated elution at pH 13 and the remaining IF was bleached employing both the 661 nm excitation at 2.7 kW/cm² and the 405 nm excitation at 1 kW/cm² or, if host species were not repeated in consecutive SRs, bleaching alone was used. Samples were blocked and stained with the next set of labels, supplied with photoswitching buffer and imaged again until the desired number of SRs was reached. Detailed experiment schedules are provided in Table 7.2 to Table 7.4.

2.2.5 Analysis

2.2.5.1 Image Registration and Rendering

For image registration, localisation files were further processed using an alpha version of a Matlab (MathWorks) script created by Maja Klevanski termed 3D-Transformer*. The script uses information extracted from the fiducial images created in 2.2.4.3 to align images from consecutive SRs to a common frame of reference. First, fiducial localisations are filtered to remove blinking emitters (likely not a fiducial), emitters close to the image borders (unlikely to be present in all SRs) and weak emitters (low localisation precision). The remaining fiducial positions are then tracked throughout the SRs by Nearest Neighbour matching. Matched pairs exceeding a predetermined factor of standard deviation (StD) from the Median pair distance are omitted. Transformed localisation files were saved in rapidSTORM format for compatibility with established rendering software.

*Release version will be made available at https://github.com/tkunerlab/3D_Transformer

The processed localisation files were imported into a separate Java-GUI[157] for autocorrelation-based lateral drift correction, filtering of emitters that are present in consecutive frames and ratiometric-based SD. Finally, images were rendered with a pixel size of 10 nm using Gaussian PSFs to represent coordinates.

2.2.5.2 **Resolution Estimate**

The practical resolution was assessed in Fiji using the Image Decorrelation Analysis plugin published by Descloux *et al.*, Nature methods, 2019[160]. The image stack of both the first and last ROI of each experiment was analysed and averaged.

2.2.5.3 **Manual Segmentation**

Images were opened in Fiji[151] and bundled into 32-bit TIFF stacks. Markers were merged into RGB images as summarised in Table 2.6 and served as the reference for manual freehand terminal segmentations. An example of image segmentation and distinguishable features is given in Figure 2.2.

Table 2.6 Merged markers as manual segmentation reference

Markers*	**Target**
Homer Bassoon/Piccolo	AZs
PSA WGA SNAP25	Cell membrane
SV2abc SNAP25 Synaptophysin VAMP1 VAMP2 vGluT1 vGluT2	SVs
VAMP1 VAMP2	Terminal type

*if available in respective experiment

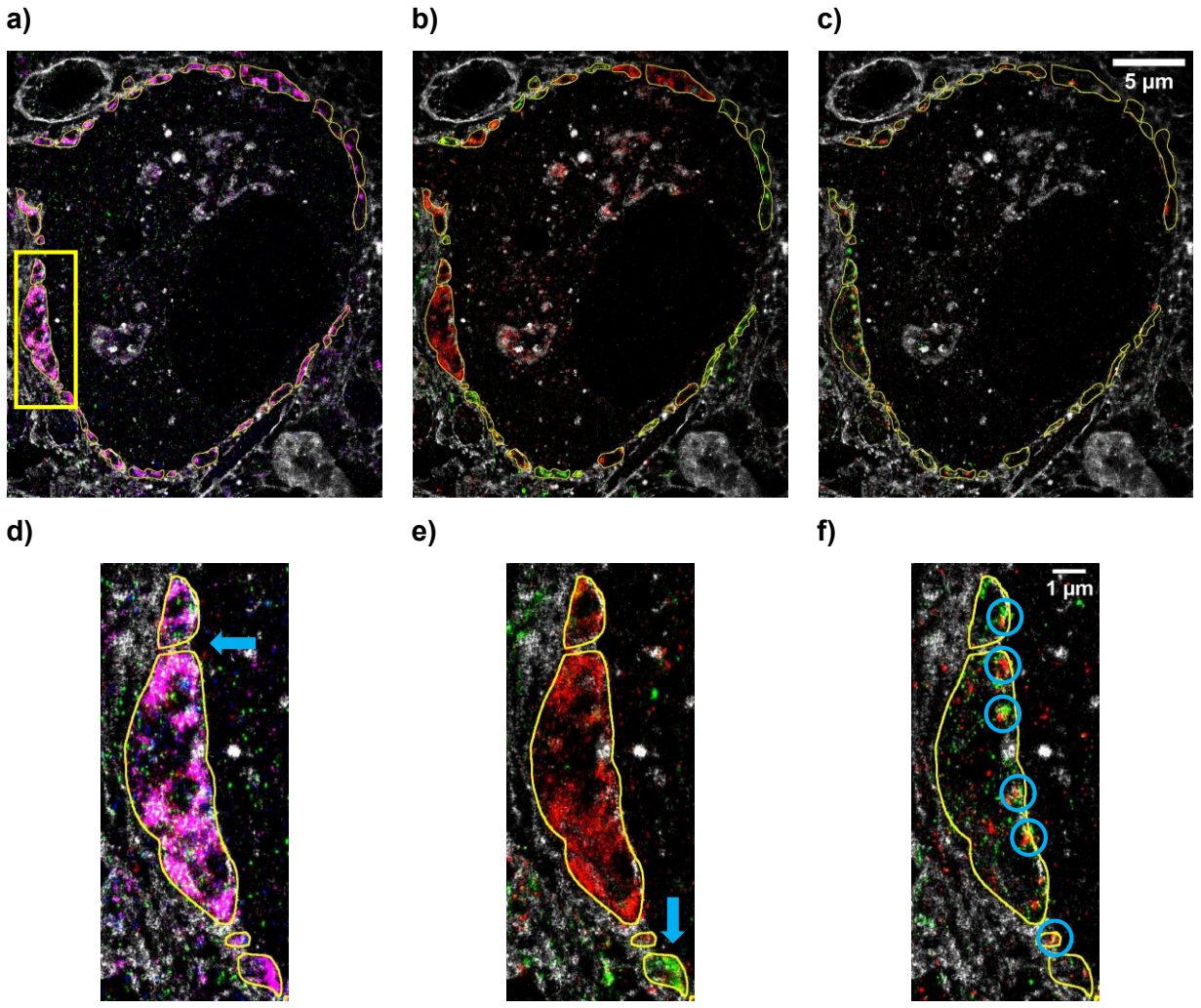

Figure 2.2 Manual segmentation of synaptic terminals. Respective images of vGluT1 (red), vGluT2 (green), SV2abc (magenta), Synaptophysin (blue) and PSA (grey; **a**), VAMP1 (red), VAMP2 (green) and PSA (grey; **b**) and Bassoon/Piccolo (red), Homer (green) and PSA (grey; **c**) are merged to aid in manual image segmentation (yellow lines). Magnifications (**d-f**; corresponding to yellow box in **a**) were used to locate borders between neighbouring terminals (**d**, arrow), extracalyceal terminals (**e**, arrow) and AZs (**f**, light blue circles).

If present, *Pisum sativum* agglutinin (PSA) or Wheat germ agglutinin (WGA) IF was used for border identification. In cases where PSA or WGA IF did not suffice to identify borders, the edges of superimposed synaptic markers were used instead (see 3.2.2).

2.2.5.4 Protein Distribution, Area and Shape Metrics

Protein distribution was assessed in Fiji as the mean grey value measured for each terminal's segmentation and protein channel. Segmentations were classified and values of a given class within a ROI were averaged per protein. Mean values of all ROIs were then averaged again to calculate an overall mean per experiment, class and protein.

Overall means for the terminal's area and shape were calculated correspondingly. Shape was assessed as circularity and calculated from the measured area and perimeter of the segmentation according to Equation 4:

$$Circ. = 4\pi\left(\frac{Area}{Perimeter^2}\right) \qquad \textbf{Equation 4}$$

Classification was dependent on the experiment type: in experiments investigating GFP-transduced tissue the classification was based on the highest GFP content that was measured within all segmentations from a single ROI, with GFP-positive being assigned to segmentations that contained >10% of the maximum GFP content and, correspondingly, GFP-negative being assigned to ≤10%. In the absence of GFP the ratio of VAMP1 contents divided by VAMP2 contents was used for classification where VAMP1-rich (calyceal) was assigned to terminals with a value of <0.5 and VAMP2-rich (extracalyceal) was assigned at a value of ≥0.5.

Statistics were calculated in Prism. Pairwise comparisons were evaluated as t-test, and one-way ANOVA was used for multiple comparisons using Šídák correction. Deviation from a normalised or averaged reference was calculated via one-sample t-test. Pairing or repeated measures was used when applicable. Significance is denoted as: $p \leq 0.05$ (*), $p \leq 0.01$ (**), $p \leq 0.001$ (***), $p \leq 0.0001$ (****).

2.2.5.5 **Mander's Co-Localisation**

Spatial relations between GFP and VAMP1/2 localisation were measured by tessellation-based Mander's co-localisation, in a total of 160 segmentations stemming from three ROIs of one animal, using Coloc-Tesseler as published in Levet *et al.*, Nature Communications, 2019[161]. Fiji segmentations were converted and exported for Coloc-Tesseler using a custom ImageJ macro script.

2.2.5.6 **Matlab Line Profile Analysis**

In Fiji, line selections were drawn parallel to the cell membrane (represented by the manual segmentation of 2.2.5.3) in areas where an AZ was located (termed accordingly) as well as SV-rich regions away from AZs (termed Off-side). AZs were identified based on the presence of Bassoon/Piccolo and Homer localisations in a sandwich-like orientation or, in ROIs exhibiting low levels of Homer staining, the correlation of defined Bassoon/Piccolo localisations and a local enrichment of PSA IF. Line selections were then rotated perpendicular to the initial selection, elongated to reach over the terminal's borders on both the proximal and distal side and set to a

width of 50 px (equalling 500 nm). Protein IF was measured as line profiles for each protein channel and selection and stored as a text file.

Data was imported into Matlab and in a first step the synaptic border was identified by fitting a Gaussian to the proximal PSA or WGA peak or, in cases of insufficient IF signal, the manual segmentation. For unscaled analysis all profiles were aligned at their Gaussian peak position and averaged into a single profile per class and experiment. For scaled analysis the distal border position was identified in the same way and profiles were scaled to the mean distance between both Gaussian peak positions before averaging, as depicted in Figure 2.3a.

Descriptive metrics were extracted from the averaged profiles using Origin 2018 (OriginLab) as depicted in Figure 2.3b-d. A Gaussian was fitted to the proximal peak of the protein distribution to assess is distance from the synaptic border (represented by the PSA/segmentation peak) and the width of distribution as indicated by the FWHM. In a second step, three consecutive integrals were applied to the profiles to compare the protein distribution in distinct sections of the terminal; to capture potential distribution patterns with a relative relation to the synaptic border, each of the three integrals spanned one-third between the proximal and distal terminal border, thus effectively covering the entire distance between borders. As distribution patterns with a distinct distance to the synaptic border or AZ are likely to be located within the framework of AZ skeleton proteins, three integrals with a width of 200 nm each were applied to the unscaled profiles, starting from the proximal border.

As educational depictions of synaptic contacts are typically oriented in a left-to-right manner from pre- to postsynaptic, this orientation was kept for the line profiles despite the non-intuitive x-scale.

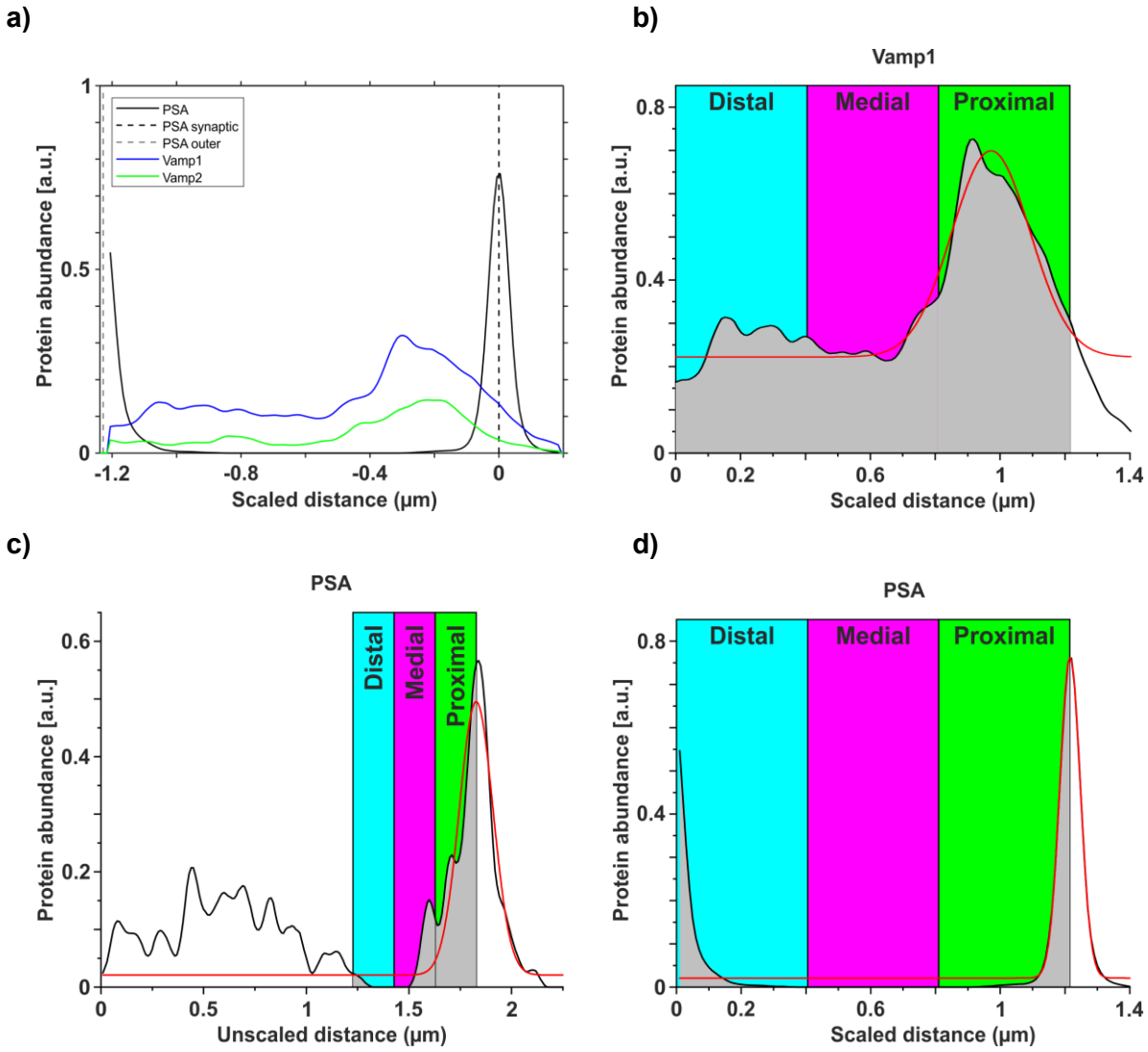

Figure 2.3 Line profile analysis in Matlab and Origin. Line profiles from Fiji were imported into Matlab, aligned at the synaptic border (0 nm) for unscaled analysis or both the synaptic as well as distal border (left axis origin) for scaled analysis and averaged (**a**). Averaged line profiles were further analysed in Origin by fitting a Gaussian (**b-d**, red curve) to the proximal (right) peak of the protein distribution (**b**) and calculating the distance to the synaptic border (**c+d**). The Gaussian's FWHM was used as an indicator for the width of protein distribution. In addition, three integrals with a width of either 1/3 (scaled, **b+d**) or 200 nm (unscaled, **c**) each were fitted to the profiles to assess protein abundance in specific sections of the terminal (blue, purple and green areas).

Profiles of sparse proteins (e.g. SNAP25) tended to be discontinuous and as a result a Gaussian fit did not accurately reflect the protein distribution in all cases (Figure 2.4). Profiles exceeding a cut-off of the Gaussian's determination coefficient (R^2) of 0.75 are therefore indicated in Figure 3.25 by hollow marks but were kept for statistical analysis due to the small sample size of 3-6 experiments.

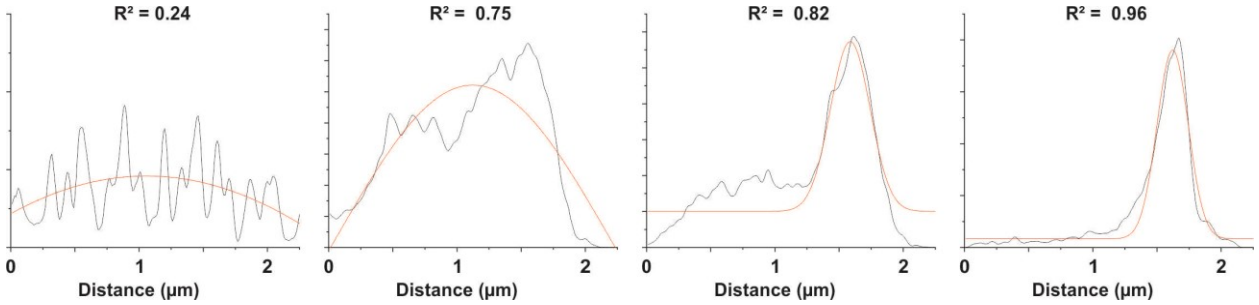

Figure 2.4 Effect of discontinuous protein distribution on Gaussian fit accuracy.

Statistics were calculated in Prism. Pairwise comparisons were evaluated as t-test and one-way ANOVA was used for multiple comparisons using Šídák correction. Deviation from a normalised or averaged reference was calculated via one-sample t-test. Pairing or repeated measures was used when applicable. Significance is denoted as: $p \leq 0.05$ (*), $p \leq 0.01$ (**), $p \leq 0.001$ (***), $p \leq 0.0001$ (****).

2.2.5.7 Micro-Segmentation Analysis

In Fiji line selections were drawn perpendicular to the long axis of AZs with a width corresponding to their size. To capture distribution effects within the periphery of the AZ, an additional set of line selections was drawn adjacent and parallel to the initial line selection either side and a width corresponding to the average AZ width (~500 nm/ 50 px). Using a Fiji script developed by Maja Klevanski, line selections were then split lengthwise into three selections of equal width and again perpendicular to the main axis into three segments of 100 nm, twice, as well as the remaining distance to the proximal border while maintaining the shape of the encapsulating segmentation, as depicted in Figure 2.5:

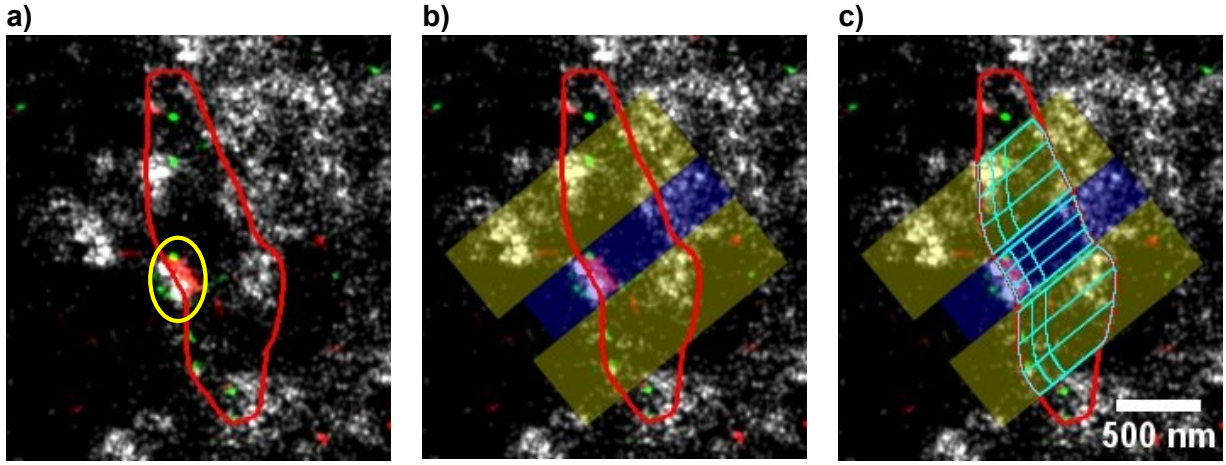

Figure 2.5 Example of micro-segmentation analysis. In Fiji image stacks and the respective manual segmentation (red line) were opened and AZs were identified (**a**, yellow circle). Line selections were drawn perpendicular to their long axis and corresponding to the width of the AZ (**b**, blue bar). Additional line

selections were added either side with a width of 500 nm (**b**, yellow bars). These three line selections were split into 9 segments each (**c**) and protein density was measured as the mean grey value per segment.

Protein density was measured as localisations per square micron, results were averaged per ROI, data per ROI was averaged per experiment. Relative protein distribution was calculated by dividing the protein content of an individual segment by the sum of all 9 segments of the respective selection.

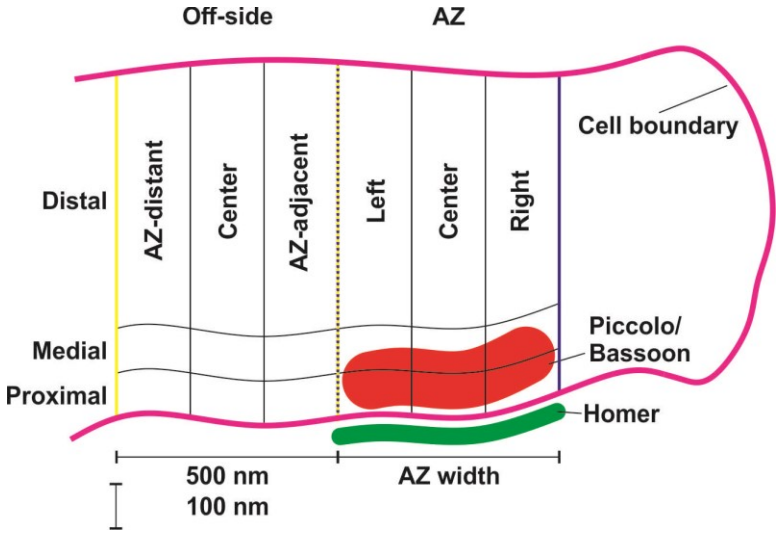

Figure 2.6 Nomenclature of sections in Micro-Segmentation analysis.

Results of individual proteins were tested for significance along each row and column, respectively, by performing one-way ANOVA in Prism. Similarly, direct comparison of VAMP and vGluT paralogs, as well as the overall protein distribution of calyceal and extracalyceal terminals was evaluated via one-way ANOVA.

As the achieved resolution did not allow identification of individual SVs, SV abundance was estimated by averaging the relative abundance of SV proteins vGluT1 and vGluT2, VAMP1 and VAMP2, SV2, SNAP25 and Synaptophysin in each section. Deviation of the protein distribution from the SV abundance was tested in Prism using a one-sample t-test against the average of the respective section. Pairing or repeated measures was used when applicable. Significance is denoted as: $p \leq 0.05$ (*), $p \leq 0.01$ (**), $p \leq 0.001$ (***), $p \leq 0.0001$ (****).

3. Results and Discussion

3.1 Development of Fiducial Strategy

In this section I will explain my choice of nanodiamonds as fiducials, the development of an immobilisation strategy for carboxylated fiducials in general and the benefits and pitfalls of its application to Nanodiamonds in particular.

3.1.1 Performance of Different Classes of Fiducials

As microscopy methods are gaining in complexity and resolution, the importance of fiducials becomes increasingly apparent. For example, multiplexed imaging approaches require registration of its sequential acquisitions to a common frame of reference[134]. Equally, the mitigation of chromatic aberrations[162], longitudinal study designs[163] or correction of the various forms of drift in lengthy acquisition techniques such as *d*STORM, PALM or PAINT[164] rely on a consistent reference. On top of general requirements like (photo-) physical stability and spectral suitability[165], ideal fiducials also need to fulfil two diametric criteria: they need to be bright enough to allow precise localisation of the fiducials for image registration purposes, but should not interfere with the recording of target signal. An often overlooked issue is that standard localisation algorithms, e.g. rapidSTORM, only locate the brightest emitter within a certain, often intensity-dependent perimeter to avoid double-sampling. Overly bright fiducials therefore cause a localisation-devoid halo around themselves that necessitates additional postprocessing steps. Camera saturation needs to be completely avoided as it impedes precise localisation of the fiducials and reduces the information content that can be sampled from surrounding areas. Successful implementations have been reported for various microscopy techniques[164–166] but were unsuited for our maS³TORM approach. Due to the multiple ROIs that were imaged for the experiments presented in this thesis, the sample disturbance caused by the pipetting robot in between imaging rounds and the before-mentioned general effects of drift on *d*STORM imaging, the development of a reliable fiducial strategy was of utmost importance for the success of the experiments presented here, though (Figure 3.1a).

I tested three categories of potential fiducials: NV^--centre nanodiamonds (ND) (Figure 3.1b), fluorophore-containing polystyrene beads represented by Tetraspecks (TS) (Figure 3.1c) and two variants of gold beads (GB; Figure 3.1d). In line with the different phenomena that cause their luminescence, the excitation and emission spectra of these types of fiducials also differ. While

the NV$^-$ centre of ND shows a large offset between excitation and emission peaks (Figure 3.1e), the far-red fluorophore of TS with its moderate Stokes shift of ~20 nm is characteristic for synthetic fluorophores. As a consequence, both ND and TS can be recorded in the red emission channel of the maS^{3}TORM microscope, but the excitation efficiency from 561 nm and 661 nm is contrary (Figure 3.1e,f). GB, on the other hand, in our measurements displayed predominantly scattering effects and therefore needed to be recorded in the emission channel corresponding to the respective laser line (Figure 3.1g). For GB, but to some extent also for other shapes of gold nanoparticles (e.g. nanorods), the ratio of absorption to scattering shifts towards scattering with increasing particle size and becomes dominant from a GB diameter of ~100 nm[167].

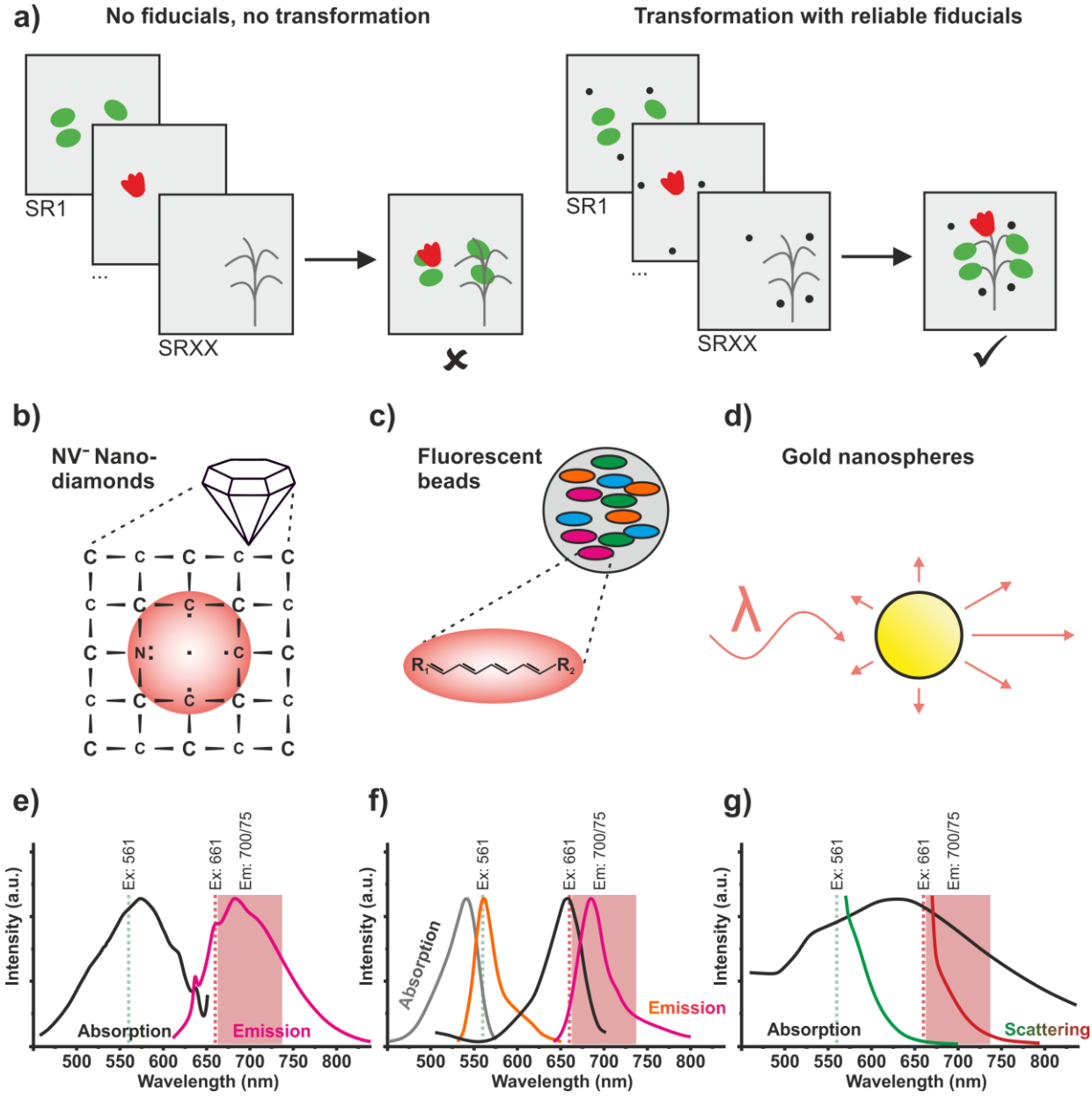

Figure 3.1 Purpose and characteristics of common fiducials. Drift, chromatic aberrations and other types of image offsets are detrimental to multiplexed imaging approaches and need to be counteracted by utilising reliable fiducials to allow faithful correlation between channels (**a**). Established options are ND with a NV^--centre point defect (**b**), polystyrene beads that contain organic fluorophores (e.g. TS, **c**) or various shapes and sizes of GB (**d**). Generally, all three options exhibit luminescence in the red emission channel of our maS³TORM microscope (**e-g**, pink area), but the brightness strongly differs depending on the excitation wavelength. (**b** shows a simplified 2D representation of the 3D diamond lettuce; for assumptions on **d** see main text.)

Due to the four fluorophore types present in TS, a moderate signal of 0.232 ± 0.126 a.u.(arbitrary units) was recorded when 561 nm excitation was paired with the orange emission channel, which exceeded ND and GB_{100} under the same conditions (0.084 ± 0.055 a.u. and 0.019 ± 0.013 a.u., respectively; Figure 3.2a). However, on the maS³TORM microscope fiducial recordings from the orange emission channel harbour the risk of chromatic aberrations when applied to *d*STORM images, which are recorded in the red emission channel. Irrespective of the excitation wavelength, GB_{100} also appeared comparably dim in the red emission channel (0.023 ± 0.01 and 0.07 ± 0.051 at 561 and 661 nm excitation, respectively). TS were ideally excited at 661 nm (0.129 ± 0.085 and 0.635 ± 0.303 at 561 and 661 nm, respectively) and therefore, especially during the first minutes of a *d*STORM acquisition, typically appeared ~10-fold brighter than the PSFs of fluorophore labels used to image target molecules, which can interfere with the ability to track target IF in the direct vicinity of TS. At the same time, because TS were prone to bleaching, they lost ~70% of brightness throughout a typical *d*STORM acquisition (30 sec average at 0 min: 142 588 ± 11 751 A/D counts, 10 min: 42 030 ± 2 933 A/D counts; Figure 3.2b) and dropped to ~10% in under 1 h of constant illumination (30 sec average at 1h: 13 978 ± 868). In line with the decline in brightness, the localisation precision dropped from 3.8 ± 2.4 nm at the beginning of the recording to 16.5 ± 9.9 nm during the last 30 sec.

Since at moderate excitation levels the scattering effect of noble metal nanoparticles is not subject to bleaching[168] and GB_{150} were generally significantly brighter than GB_{100}, the brightness of GB_{150} remained at a high level throughout the recording (500 123 ± 68 955 A/D counts), therefore creating similar tracking issues in their vicinity as TS. In addition, GB showed strong brightness fluctuations during the first half of the recording (min/max: 271 599/797 524 A/D counts), a phenomenon that is still poorly understood[169]. These changes in PSF intensity are reflected by a lower initial localisation precision compared to the end of the recording (first 30 sec: 6.4 ± 6.1 nm, last 30 sec: 2.7 ± 1.9 nm). As a result of the wide spread between the excitation and emission peak of ND and the correspondingly high excitation efficiency at 561 nm, ND measured 20-fold brighter under these conditions compared to an excitation at 661 nm (0.6 ± 0.213 and 0.03 ± 0.036, respectively; ~0.3 kW/cm², 5 Hz, each; Figure 3.2a). Under *d*STORM conditions this

resulted in a brightness of 44 683 ± 1 349 A/D counts (Figure 3.2b). The remarkably low StD of ND was also apparent from the steady localisation precision of 6.2 ± 3.6 nm during the first, and 6.3 ± 3.8 nm during the last 30 sec of the recording.

The spectral properties of ND allow an imaging approach where the tasks of drift correction and image registration are sequentially accomplished as separate recordings. The comparably moderate ND signal under *d*STORM conditions is sufficient for lateral drift tracking without adverse effects on the detection of target IF. After the *d*STORM recording, a dedicated fiducial image is acquired using 561 nm excitation and the red emission channel, which provides bright fiducial PSFs that allow for superior localisation precision. Negative effects of remaining target IF are avoided due to the low excitation efficiency of AF647 and CF680 under these excitation conditions, simultaneously chromatic aberrations are circumvented by recording both steps from identical imaging channels. Combined with the ND's stable emission and resilience against bleaching[170] they represent ideal fiducials for the use case of our maS³TORM microscope.

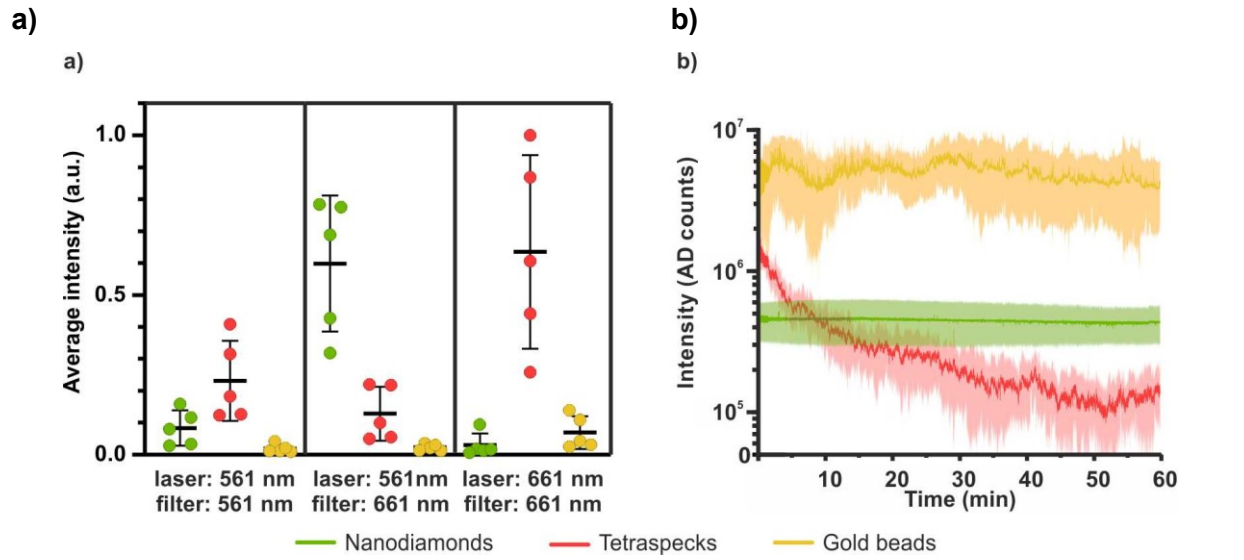

Figure 3.2 Average fiducial intensity in different excitation/emission conditions and over time. GB_{100} showed comparably low brightness levels irrespective of the combination of excitation and emission channel (**a**). ND displayed the highest intensity in the red emission channel when excited at 561 nm, TS brightness peaked under 661 nm excitation. At the beginning of a 1 h *d*STORM recording, TS presented noticeably brighter than ND (**b**). TS are lost ~90% of intensity over the course of the recording due to bleaching. Bleaching did not affect ND or GB_{150}. ND outperformed both TS and GB in terms of emission constancy.

3.1.2 EDC-Mediated Fiducial Immobilization

The main purpose of fiducials is the possibility to re-identify a certain position within a sample, ideally with a precision that exceeds the resolution of the microscopy technique they are used with to enable aberration-free registration of consecutive images. To accomplish this, loss or

movement of fiducials needs to minimised. Carboxylated fiducials, e.g. ND and GB_{100}, become negatively charged in an aqueous environment and therefore electrostatically attach to positively charged poly-lysine-coated surfaces (Figure 3.3a,b). However, we found that due to the mechanical forces generated by the fluid exchanges during maS³TORM experiments, electrostatic forces alone were not sufficient to prevent movement or loss of fiducials. The EDC coupling reaction offers a solution to this issue by covalently binding the carboxyl group of a respective fiducial to the primary amine found in the poly-lysine coating through an amide bond[171] (Figure 3.3c). The by-product urea can easily be removed from the treated glass surface by rinsing with ddH_2O, which makes this approach suitable for cell culture experiments. We found that an additional blocking step with FCS before the cells are seeded is beneficial for cell survival (data not shown).

Since, to my knowledge, EDC coupling of fiducials to lysine-coated glass surfaces had not been published, I used the Merck-Millipore Application Note for Microsphere Coupling[149] as a point of reference. The protocol that I derived from the application note (see 2.2.1.2) used a solution with a high ionic strength for the initial fiducial seeding step as well as the main bonding phase and caused the ND to form large, irregularly shaped clusters that were incompatible with Gaussian-based localisation methods (Figure 3.3, top panel). Balinovic *et al.* have reported similar issues about the use of ND as fiducials[165]. Reducing the ionic strength by seeding the fiducials in ddH_2O and optimising the buffer composition for the bonding phase (see 2.2.2.1) proved to be highly efficient to ensure a singularised distribution of fiducials (Figure 3.3d).

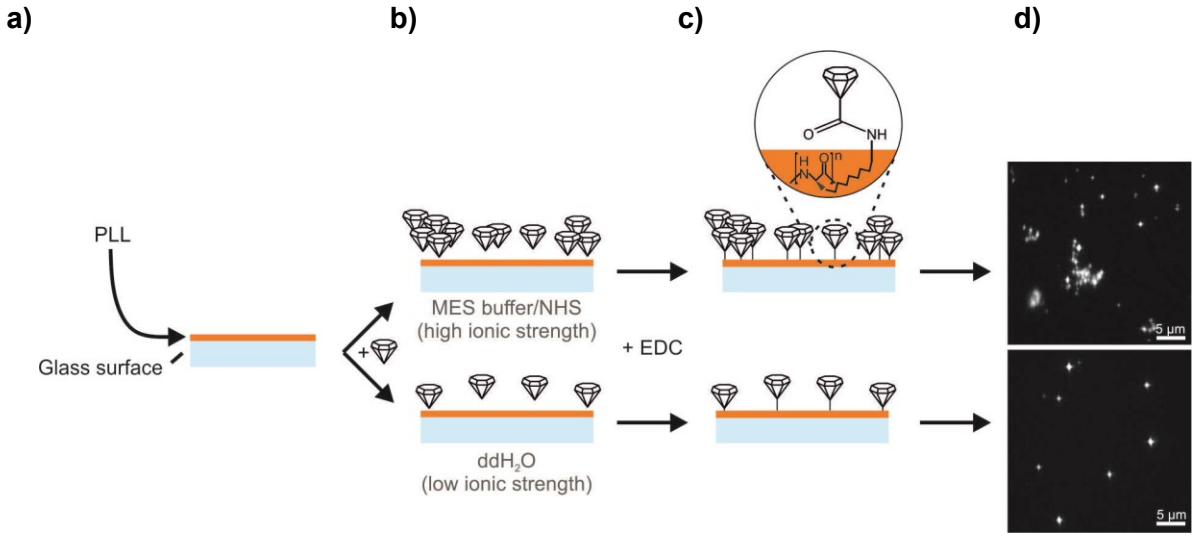

Figure 3.3 Development of the EDC-mediated fiducial immobilization approach. Poly-(L)-lysines are routinely used as glass surface coatings and provide primary amino groups (**a**). Carboxylated fiducials (e.g. ND) can be sedimented and covalently attached onto these surfaces by using the EDC coupling reaction (**b**), which forms an amide bond between the two reactive groups (**c**). The high ionic strength of buffers that

are used in established coupling protocols can facilitate clustering of the fiducials (**top panel**), which is especially pronounced when using ND (**d, top**) and impedes precise localisation. By optimising the coupling protocol to a lower ionic strength, I achieved a predominantly singularised distribution of fiducials (**bottom panel**).

Using the initial coupling protocol, cluster sizes exceeding 40 particles could be observed for ND with an average cluster size of 2.74 ± 5.7 particles per cluster and 21.6% of clusters consisting of three or more particles (Figure 3.4a). The optimised protocol yielded 1.12 ± 0.72 particles per cluster and a maximum observed cluster size of ~3 particles per cluster. The approach was also applicable to GB_{100} and TS with near-identical results (GB_{100}: avg. 1.12 ± 0.65, max. 2.9; TS: 1.11 ± 0.58, max. 2.7).

For optimal registration results it is beneficial to have multiple fiducials available within a ROI. This ensures that loss of a fiducial can be compensated and improves registration precision by averaging optical aberrations and localisation deviations. For the maS³TORM microscope's FOV of ~2050 µm² (512*256 px per SD channel) I have found ~12 ND fiducials to be a practical density which equates to a dilution of 1:8 000 (Figure 3.4b).

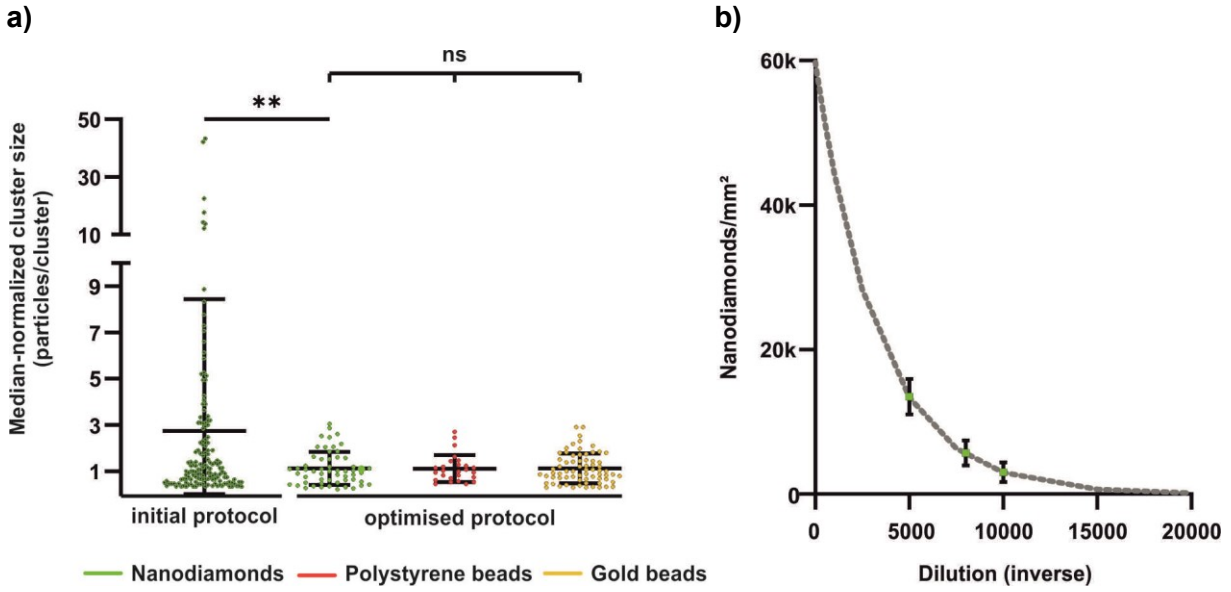

Figure 3.4 Effect of EDC coupling protocol on clustering behaviour of fiducials. Reducing the ionic strength of the buffers employed in the EDC coupling protocol significantly reduced the tendency of ND to form clusters, was also applicable to GB_{100} and TS (**a**) and allowed ND to be applied at a controlled density (**b**).

Compared to the fiducial approach from our original publication reporting on the maS³TORM microscope[92], which was relying on non-immobilised TS, the EDC coupling approach eliminated the loss or relocation of TS and ND fiducials even after an extended amount of sample washing repetitions (Figure 3.5a). The approach was also tested with GB_{150} and, in line with expectations,

did not prevent particle loss or relocation as the GB_{150} used here do not possess carboxylic functionalisation. Accordingly, the registration precision that was achieved with GB_{150} (12.3 ± 11/18.4 ± 12.5 nm) was not significantly different from non-immobilised TS (15.4 ± 12.3/17.4 ± 15.8 nm) both in lateral and axial directions, respectively (Figure 3.5b). In the case of non-immobilised TS, of the 5 ROIs that were imaged over 10 rounds a total of 40% of the resulting images could not be registered successfully. In the case of $GB_{150,}$ 14% of images were lost for subsequent analysis due to insufficient fiducial coverage. In the lateral direction, immobilised TS performed significantly better than their non-immobilised counterpart with no losses and a registration precision of 5.5 ± 1.5 nm, however, only minor improvements were measured in the axial direction with a precision of 15 ± 6.6 nm. This is noteworthy as polystyrene as a material does not contain carboxyl groups and TS in particular are not claimed to be surface-functionalised. Yet, in contrast to GB_{150} which also lacked appropriate surface modifications, TS responded well to the EDC immobilisation. Immobilised ND performed gradually better in lateral direction (2.7 ± 1.8 nm) than immobilised TS and ranked significantly superior for axial registration precision (4 ± 2.5 nm).

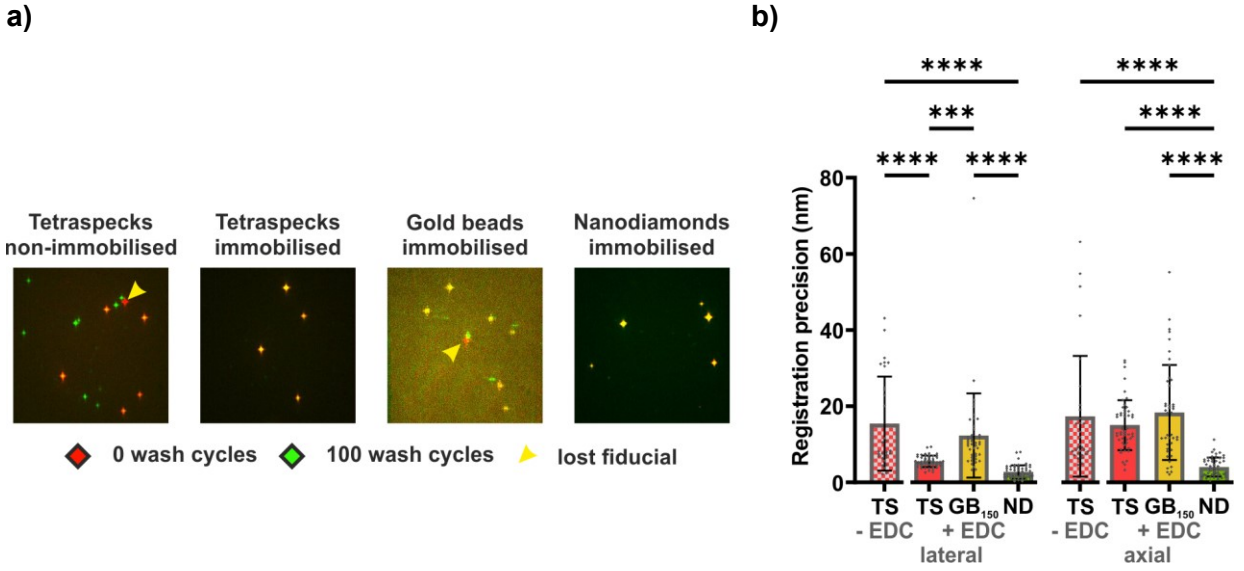

Figure 3.5 EDC-mediated immobilisation of fiducials improves registration precision. Fluid exchange-induced relocation or loss of non-immobilised and covalently bound fiducials (**a**). This approach fully eliminates loss of particles and has the potential to significantly improve registration precision up to a range of a few nanometres (**b**, ND).

The combination of the spectral properties, the stable emission and the possibility for covalent immobilisation rendered ND the superior fiducial choice for maS³TORM imaging. In comparison to the registration precision that was achieved in earlier experiments which were employing non-immobilised TS, immobilised ND provided a 6.6-fold increase in precision (25.1 nm and 3.8 nm,

respectively) and drastically improved the reliability on an image-to-image basis as is apparent from the ~8.7-fold decrease of the StD (15.1 nm and 1.7 nm, respectively; Figure 3.6).

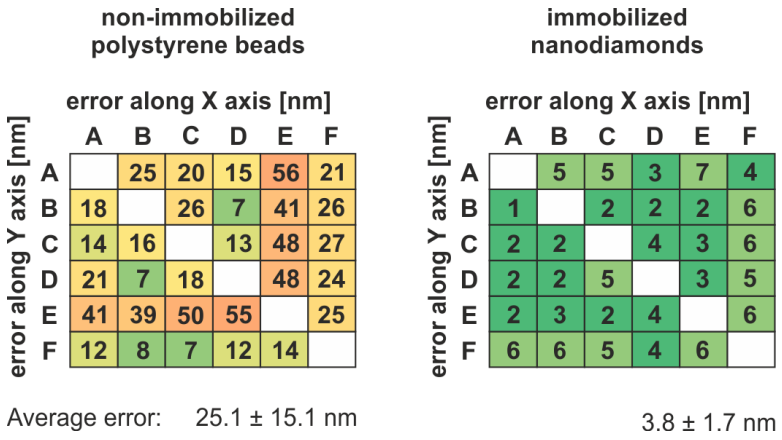

Figure 3.6 Comparison of registration precision. Compared to immobilised ND, in a practical use case non-immobilised TS showed a higher registration error between SR and an elevated inconsistency (data and template modified from Maja Klevanski).

3.2 MaS³TORM Experiment Evaluation

In this section, I will demonstrate the experimental limitations of the maS³TORM experiments that were conducted by myself and explain its implications for the analysis if the data.

3.2.1 Achievable Resolution and Limitations

In single-molecule imaging, resolution refers to the precision with which the position of a target molecule can be determined[104]. It can be theoretically calculated as the product of the localisation uncertainty and the linkage error (see 1.2.2.5) or estimated from existing data sets using several approaches[172]. In the lateral plane a practical resolution of 28.6 ± 3 nm was measured via decorrelation analysis[160], which is in line with the results from our previous publication (see Klevanski *et al.,* Suppl. Fig. 10)[92] and accounts for the mostly indirect IF approach that was used here. Axial resolution is difficult to determine from practical localisation data but has been reported in a range of ~50-70 nm for comparable *d*STORM setups[123,133]. At this resolution, calyx of Held synapses could be identified in tissue sections with ease (Figure 3.7a) and separate terminals were clearly discriminable through their encompassing membrane signal. While larger structural features such as SV clouds and AZs were also visually identifiable (Figure 3.7b), in line with Nyquist's Theorem[125], at the achieved resolution it was not possible to distinguish individual SVs (Figure 3.7c), given their size of around 40 nm[88,173] and the multitude of SVs staggered at random throughout the depth of each tissue section. For this reason, protein distribution was assessed at the SV population level using a terminal-wide, a line profile-based and a micro-segmentation analysis. Potential future avenues that would allow to resolve individual SVs even in densely populated tissue areas are briefly discussed in chapter 5.

As expected, the presynaptic terminals that were found in contact with the principal cell consisted of a small number of large, elongated compartments likely representing calyceal digits that were sectioned lengthwise[73,88], as well as numerous smaller compartments that varied in shape, size and expression pattern[75].

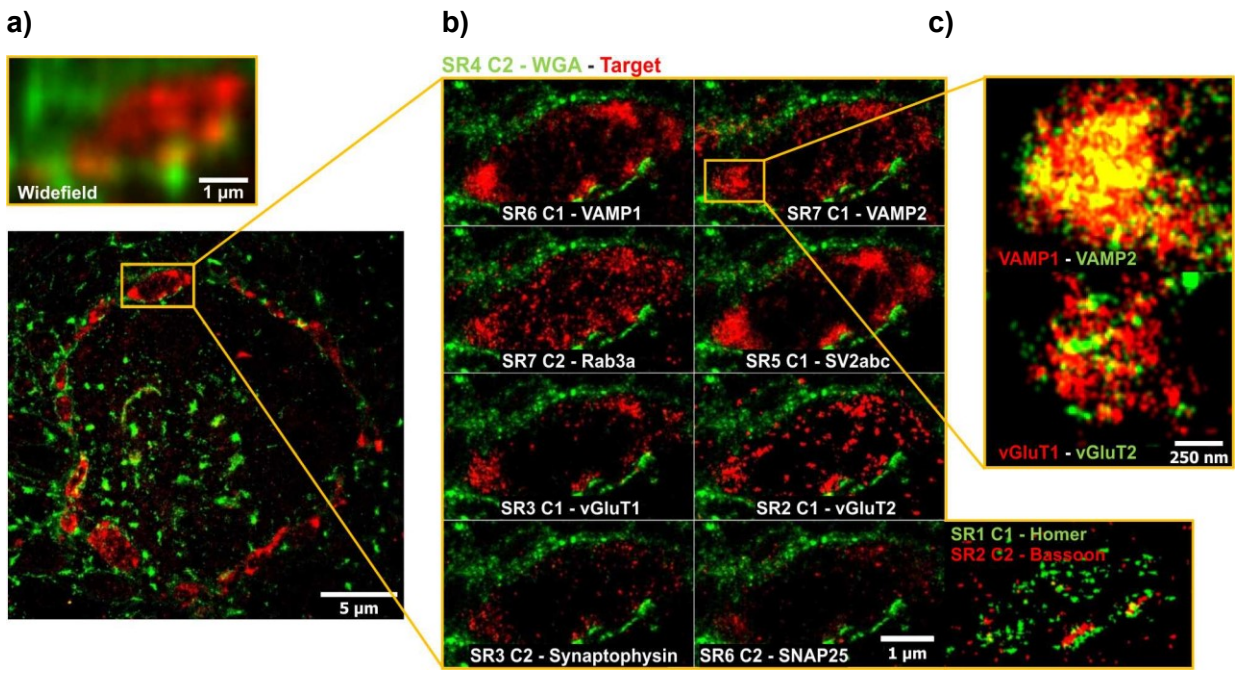

Figure 3.7 maS³TORM imaging of the calyx of Held at increasing magnification. While calyx of Held terminals as a whole, due to their size of ~20 µm, can be identified in tissue sections even with diffraction-limited microscopy techniques, delineating individual terminals required super-resolved imaging (**a**). At <30 nm of lateral resolution, sub-cellular features like SV clouds and AZs were identifiable and gave excess to terminal-wide protein distributions (**b**). However, the combination of achieved resolution and axial tissue depth did not allow identification of single SVs (**c**). [SR: Staining Round; C: Channel]

3.2.2 Constraints of Membrane Staining

At young age, 40%-50% of the principal cell's surface is encompassed by calyx of Held protrusions. The remaining part of its circumference is occupied by passing axons, glial cells and other non-calyceal components[88,174]. Due to the increasing level of fenestration around and after the onset of hearing[73,175], it is supposable that at the age studied here (P12-P21) the proportion of presynaptic terminals to other cellular compartments was further reduced[77]. Therefore, it was important to be able to identify the boundaries of individual cell compartments to unambiguously investigate cellular features and average structural data without accidental intermixing of cell types.

Since the lipid fraction of cell membranes lacks epitopes for antibody recognition and intercalating dyes are unsuited for maS³TORM experiments with its detergent-based elution approach, the fluorophore-labelled plant lectins PSA and WGA were used to track cell boundaries (Figure 3.8a). These lectins target the (posttranslational) glycosylation of lipids and proteins that are located predominantly in plasma membranes[92]. For unobtainable reasons, the performance of both lectins

was highly variable in the present experiments and superimposed projections of several synaptic markers (e.g. VAMPs, vGluTs, SV2 and Rab3a) in combination with SNAP25 as an SV- and cell membrane-specific marker were used for compartment segmentation in some instances (Figure 3.8b). We found that targets of both lectins, but PSA in particular, were enriched in the area of the synaptic cleft (Figure 3.8c; for a detailed analysis see Schroeter *et al.,* 2024 – manuscript under preparation), which was used as an additional cue to identify AZs in cases where IF of one of the AZ-specific markers (Bassoon/Piccolo or Homer1bc) was inconclusive (Figure 3.8d).

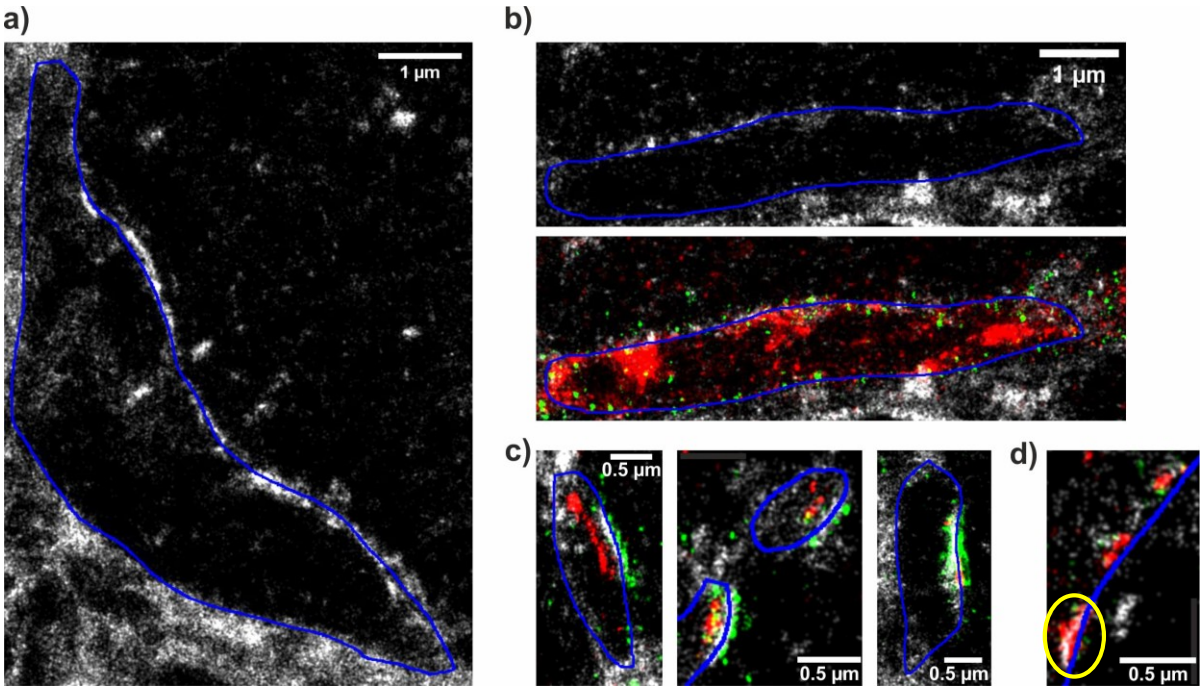

Figure 3.8 Plant lectins PSA and WGA as membrane and AZ markers. Samples for maS³TORM imaging were stained with fluorophore-conjugations of PSA and/or WGA for membrane tracking to aid in manual cell segmentation (**a, segmentation in blue**). In cases of limited performance, a projection of synaptic markers (e.g. vGluTs, VAMPs, SV2, Rab3a; **red**) along with SNAP25 (**green**) were complementarily used (**b**). Both lectins were enriched in the synaptic cleft (**c**) and served as additional cues to identify AZs (**d, yellow circle**).

3.3 Identification of Extracalyceal Terminals

In the following section, I will illustrate the importance of unambiguous neuron type identification in the MNTB and introduce an approach that allows the discrimination of projections with similar appearance to the MNTB principal cell based on endogenous protein expression.

3.3.1 Distinct VAMP1/2 distribution at the calyx of Held

Dual-colour projections of VAMP1 and VAMP2 revealed a distinct distribution of the two VAMP paralogs between individual presynaptic terminals (Figure 3.9). While the exact expression levels of VAMP1 and VAMP2 cannot be determined from this data due to the unknown performance of the respective ABs, a comparison of abundance levels between distinct areas of a given ROI can be conducted without detailed knowledge of binding characteristics or amplification levels. Segmentation analysis (details below) revealed that the majority of terminals contained predominantly VAMP1 at a ~4:1 ratio over VAMP2, which were termed “VAMP1-rich” accordingly. The second type was characterised by containing VAMP2 at exceptionally high levels while VAMP1 was observed at levels comparable to the IF obtained within the nucleus of the principal cell (data not shown), which indicates that the latter can be regarded as background signal. A VAMP1/VAMP2 ratio of ~ 1:10 was measured in this terminal type, hence termed “VAMP2-rich”.

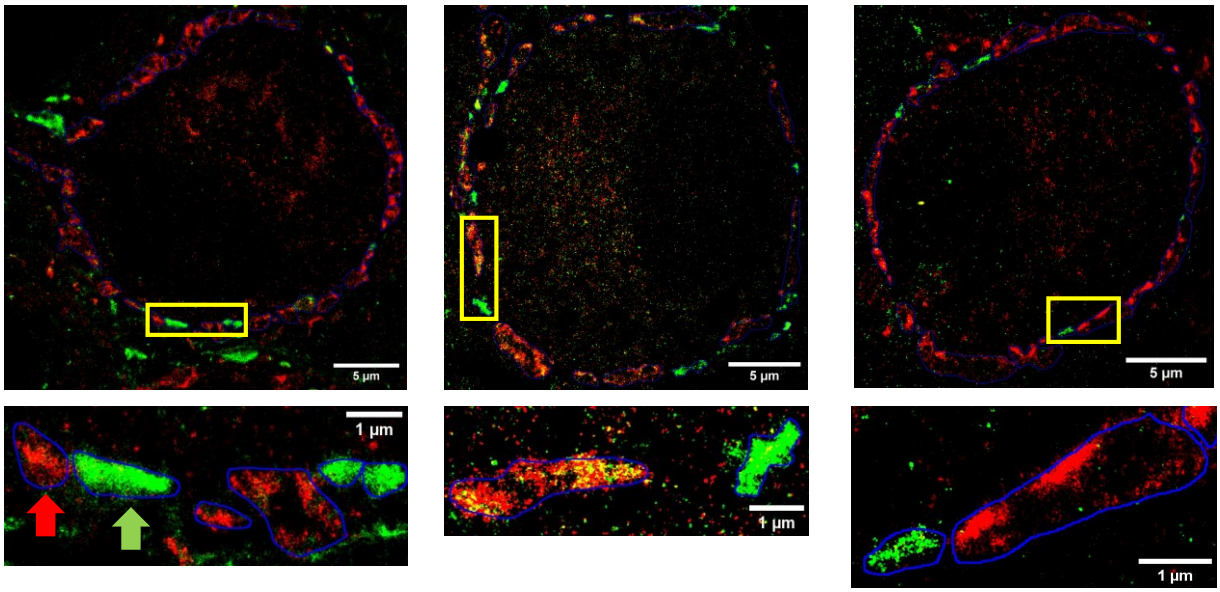

Figure 3.9 Distinct distribution of VAMP1 and VAMP2 between individual presynaptic compartments. Contrast-matched dual-colour maS³TORM projections of VAMP1 (**red**) and VAMP2 (**green**) IF images from P12-13 rats revealed a differential distribution between presynaptic compartments in contact with the principal cell. VAMP1-rich terminal are indicated by a **red arrow**, VAMP2-rich by a **green arrow**. Magnifications correspond to areas marked in **yellow**. Examples represent individual animals.

The underlying causes of these striking differences in protein layout needed to be clarified to ensure meaningful interpretation of the subsequent analyses. Multiple explanations appeared plausible: 1) there is evidence that in the calyx of Held the VAMP composition changes during the onset of hearing[176]. This change could happen at different rates in different regions of the calyx. Alternatively, it is debated that at prenatal age the principal cell is innervated by multiple GBC projections which, by the onset of hearing, mostly deplete to a single input, potentially in a competitive fashion[68,69]. The differences in VAMP employment could therefore also stem from individual GBC projections in different states of competition or development[78]. 2) It is well documented that the principal cell receives additional non-calyceal (bouton-type) inputs, however, the exact nature of these inputs is still under debate[77,78]. Precalyceal collaterals, i.e. afferents that branch from the GBC axon before the arborisation into the calyceal terminal and contact neighbouring principal cells, have been described but their frequency remains elusive[76,78,79,156]; evidence pointing towards them being sparse[177]. Yet, non-calyceal excitatory inputs have been described as frequent and unequivocally distinguishable from calyceal inputs by electrophysiological characteristics[81]. In addition, inhibitory projections are claimed to be covering up to 20% of the principal cell's surface[77] with a smaller subset of the inhibitory projections being glycinergic[77,178], whilst the majority was identified as being of GABAergic nature[77,82]. This implies the existence of substantial non-GBC input to the principal cell of the MNTB, which we termed extracalyceal[176,179]. 3) AZs in the calyx of Held are known to have a comparably low P_R but arriving stimuli are relayed to the principal cell with high fidelity nevertheless[89,91]. This is achieved by the large number of AZs[88,89,180] and the complex geometry of the calyx which ensures that only a small subset of AZs is responding to each individual action potential[90,181,182]. Since the VAMP paralogs are associated with different release kinetics[54,55] it is conceivable that the two terminal types represent the extremes of a differential expression pattern that is contributing to the structural diversity of the calyx and thus preventing synaptic depression[89,183].

3.3.2 Investigation of Developmental Effects on VAMP Distribution

First, I investigated hypothesis 1) by comparing morphological and protein density metrics of tissue samples generated from P21 rats to the samples presented in 3.3.1 which were obtained at the onset of hearing (P12/13). If the differential expression pattern in terminals surrounding the principal cell is an effect of developmental processes, changes in the expression profile should be visible at condign distance to the onset of hearing[184].

Regarding morphological features, no relevant changes were observed between the two time points (Figure 3.10). Likely due to the effects of fenestration, the size of VAMP1-rich terminals

was marginally reduced (Figure 3.10a) and the circularity of both terminal types was (significantly) increased at higher age. However, a reduction in VAMP2-rich terminals, as it would be expected if the expression pattern was an effect of the developmental change of the VAMP paralog expression in the calyx, was not observed; if at all, an insignificant increase in the number of VAMP2-rich terminals could be noted (Figure 3.10c).

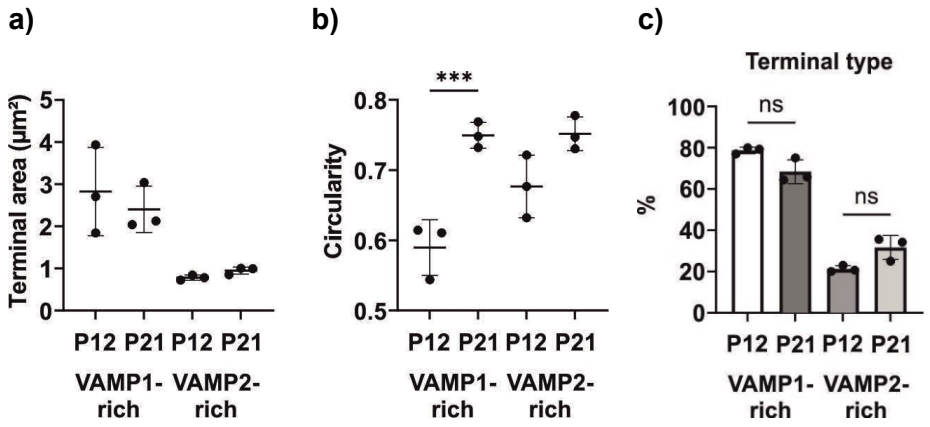

Figure 3.10 Developmental effects on morphological features of two presynaptic terminal types. Irrespective of VAMP composition, presynaptic terminals contacting the principal cell did not substantially change in size within a week after the onset of hearing (**a**), but appeared (significantly) more globular at P21 (**b**). The ratio of VAMP1- and VAMP2-rich terminals did not change significantly, but showed a minimal visual shift towards VAMP2-rich terminals with age (**c**). Data points represent individual animals; Mean ± StD; for statistics see Table 7.1.

Likewise, no significant differences were obtained for the VAMP content of the two terminal types (Figure 3.11). While there was an non-significant increase in VAMP2 expression in VAMP2-rich compartments at older age, the VAMP1 protein density remained unchanged. Rab3a was also without significant changes in expression profile. However, a significant increase in protein density in VAMP1-rich terminals was obtained for vGluT1. An age-dependent upregulation of vGluT1 expression has been observed by others as well[185], also in the context of the MNTB[58]. Since a reduction of P_R has been reported for the mature calyx[91], the upregulation of vGluT1, which is associated with a lower P_R than vGluT2[56], aligns with expectations. The consistently low level of IF signal of vGluT1 in VAMP2-rich terminals might be indicative of a detection of background signal again. Lastly, a strong and significant increase in the detection levels of SNAP25 was observed in both terminal types (illustrated by Figure 3.11, inset), which could be linked to the effect of SV pool maturation[41].

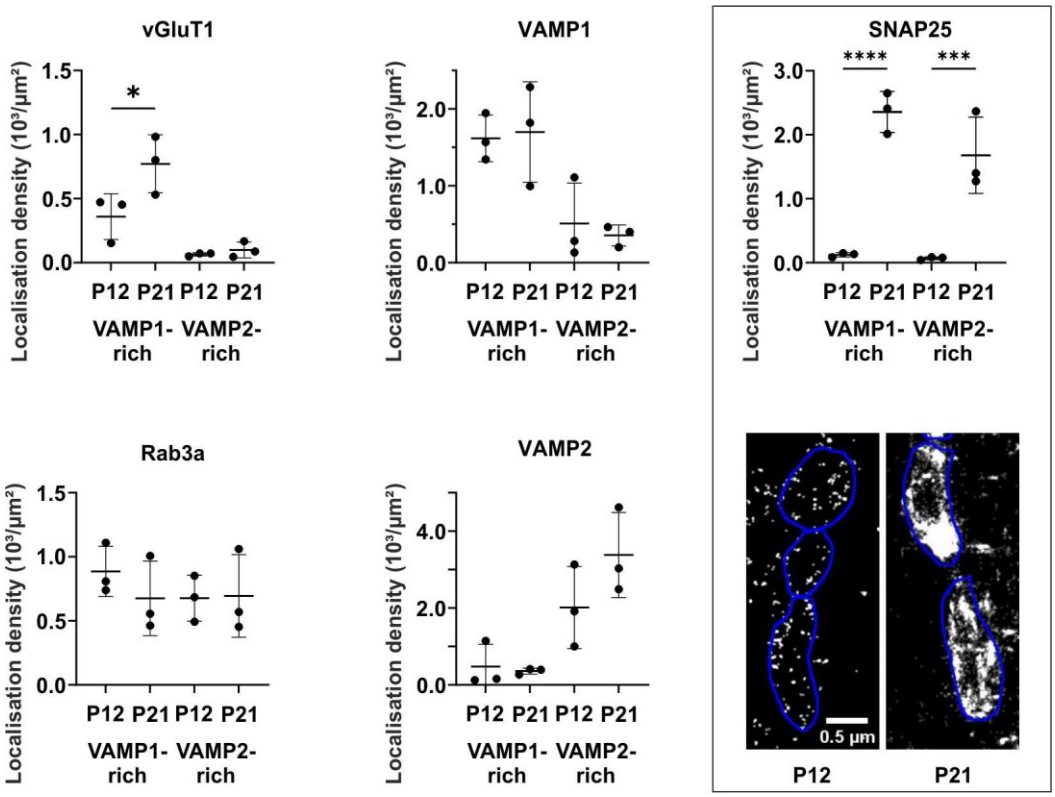

Figure 3.11 Developmental effects on protein expression of two presynaptic terminal types. Protein density was measured from segmented maS³TORM images and no significant changes were observed for major synaptic proteins between P12/13 and P21 except for a drastic increase in SNAP25 levels at older age, indicating that the distinct VAMP distribution is not a developmental effect. SNAP25 inset shows maS³TORM images and that are matched in contrast levels. Data points represent individual animals; Mean ± StD; for statistics see Table 7.1.

To exclude MNTB-wide expression trends and instead focus on local changes of expression pattern, protein density was normalised to the age-related protein density in VAMP1-rich terminals. This confirmed the significant but age-unrelated expression pattern of VAMP1 and vGluT1, both being reduced in VAMP2-rich terminals (Figure 3.12, also see inset). A similar relation was visible for SNAP25, although with less significance. On the other hand, the elevated expression level of VAMP2 in VAMP2-rich terminals was preserved as well. Interestingly, after normalisation, an age-related increase was also observed for Rab3a in VAMP2-rich terminals, which was not apparent from absolute measures (compare Figure 3.11). Since a Rab3 knockout reduces P_R[61,186], its upregulation should favour synaptic reactivity. This ties well into the context of a VAMP2- and vGluT2-rich synaptic terminal (details below), as both are also associated with a heightened P_R (see [54] and [56,57], respectively), which contrasts with the generalised view of the calyx being characterised by a remarkably low P_R[89–91,182].

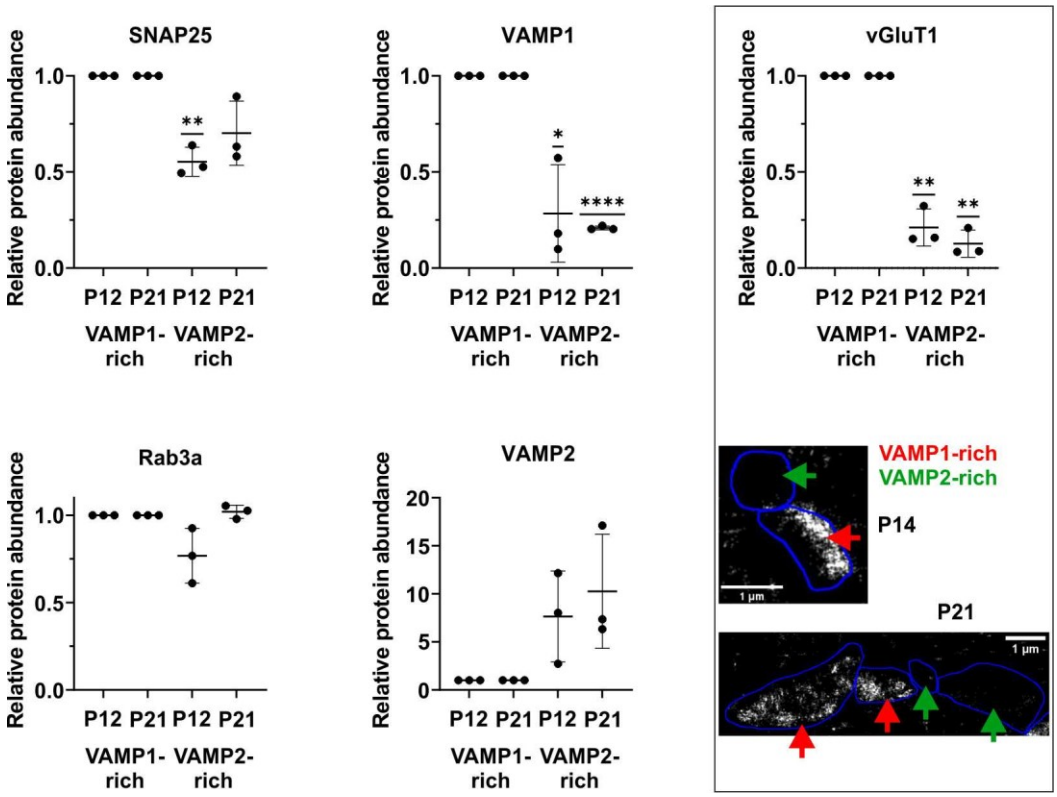

Figure 3.12 Normalised developmental changes of protein distribution in two presynaptic terminal types. Normalisation was used to separate local differences in protein expression from general developmental effects and confirmed that the VAMP ratio as well as vGluT1 expression levels did not significantly change with age. The examples show maS³TORM images of vGluT1 in VAMP1- and VAMP2-rich terminals at P12 and P21, respectively. Data points represent individual animals; Mean ± StD; for statistics see Table 7.1.

Overall, the presented density data contradicted a developmental effect on the VAMP expression profile in MNTB presynaptic terminals and painted a picture of two functionally, and therefore likely also spatially, distinct synapse types. The difference in size and shape of the terminals further underlined this assumption[75].

3.3.3 Confirmation of Extracalyceal Inputs to the Calyx of Held

Since the VAMP expression profile showed insignificant dependence on age, next I tested for an extracalyceal origin of MNTB terminals as an explanation for the VAMP distribution discrepancy. P2 rats were injected with a viral expression system (pAM-AAV-CAG-eGFP) into the left VCN to trace its GBC projections to the contralateral MNTB[156]. Tissue was generated at P13 and checked for successful targeting of the VCN and sufficient GFP expression to allow delineation of the full GBC axon trajectory via widefield fluorescence microscopy (Figure 3.13). Of the animals that survived the mother's petulance, the success rate of targeting the VCN was 100% (data not shown).

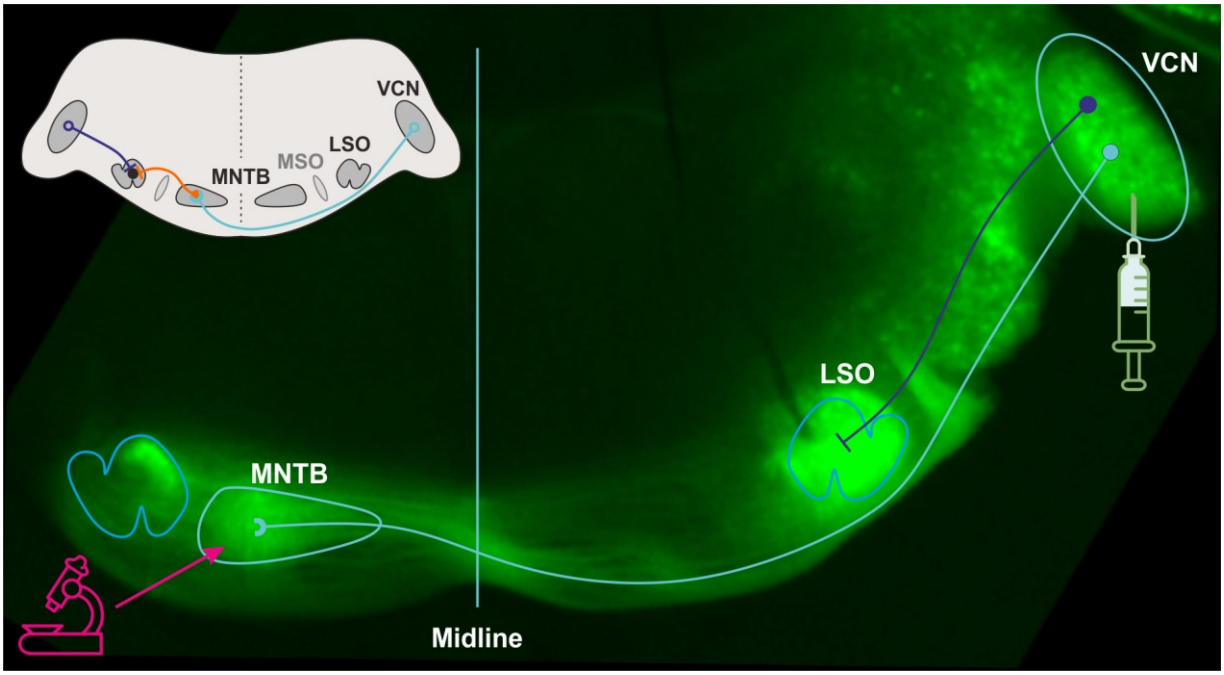

Figure 3.13 Top view onto a semi-coronal section of GFP-transduced rat brain stem. The sinistral VCN of P2 rats was transduced with GFP via retroviral gene transfer for anterograde tracing of its GBC projections to the contralateral MNTB. Results were verified by fluorescence imaging on a Leica DM6000 widefield microscope at P13 and showed the successful labelling of the respective neuronal pathway (**light blue line**), including the ipsilateral lateral superior olive (LSO) (**dark blue line**).

As a result of the targeted injection of the AAV-GFP viral particles into the VCN, only presynaptic terminals stemming from GBC projections, that is calyceal terminals and precalyceal boutons, were labelled by GFP. Thus, assuming 100% infection efficacy, an extracalyceal origin of presynaptic terminals would be marked by the absence of GFP IF from the respective terminal. While infection rates are unlikely to reach 100%, I did not observe any calyces that were marked by complete absence of GFP IF, which would indicate failure of infection in a specific GBC projection.

To probe for GFP co-localisation, ultra-sections of the GFP-transduced tissue were generated and used for maS³TORM imaging. Dual-colour projections of VAMP1 and VAMP2 showed the aforementioned characteristic distribution pattern (Figure 3.14, left). In the overlay with GFP IF, compartments containing GFP signal overlapped well with VAMP1-rich areas (Figure 3.14, centre), while VAMP2-rich compartments were mostly devoid of GFP signal (Figure 3.14, right). This visually confirms the previous assumptions about an extracalyceal origin of the VAMP2-rich terminals.

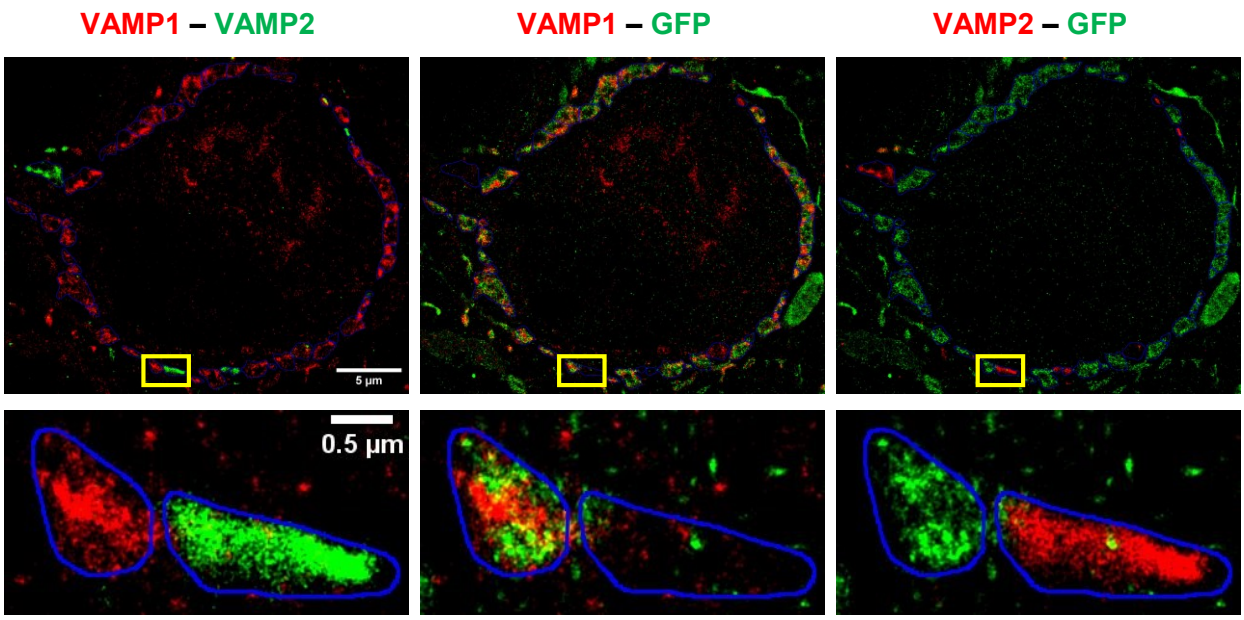

Figure 3.14 GFP-transduced terminals co-localise with VAMP1-rich areas. GFP-transduced tissue sections were imaged on the maS³TORM microscope for both VAMP1 and VAMP2 (**left**). Dual-colour projections revealed that the terminals that were labelled by GFP – and therefore of verified calyceal origin – coincided with VAMP1-rich areas (**centre**) and showed little to no overlap with VAMP2-rich areas (**right)**. Magnifications show regions denoted in yellow.

To support the visual determination, co-localisation in the form of the Mander's coefficient[187] was measured, which ranges from 0 (no overlap) to 1 (perfect overlap). Because super-resolved microscopy allows for a resolution at the scale of proteins, direct co-localisation of protein targets is impossible in this context as two proteins cannot coexist within the same space[188]. The combined effects of localisation uncertainty and linkage error as well as the axial superposition of a 3D sample when reduced to a 2D projection partially negate this effect, still, specialised tools should be used to accurately calculate the spatial relationship of two or more targets from localisation data. A promising avenue for arbitrarily distributed or non-clustered target proteins is tessellation-based co-localisation where space is divided into Voronoï diagrams that span between the half-way points of neighbouring localisation coordinates. Overlap of the resulting planes (2D) or polyhedrons (3D) of different targets can be calculated with high precision[161,189,190]. It revealed a median Mander's co-localisation coefficient of 0.68 between VAMP1 IF and GFP occupancy as the calyceal marker, which proves that VAMP1-rich terminals are of calyceal origin. On the other hand, a median overlap of 0.11 was measured between VAMP2 and GFP IF which further validates the extracalyceal origin of VAMP2-rich terminals. The skew of the VAMP2 results towards larger Mander's coefficients (average: 0.24 ± 0.25) can be explained by the coexistence of both VAMP paralogs in VAMP1-rich terminals. Visual inspection of the entire data set confirmed the exclusive nature of VAMP2-rich terminals and GFP labelling without exceptions.

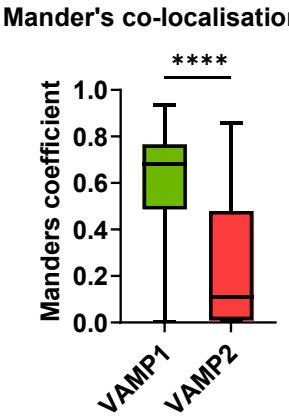

Figure 3.15 Mander's analysis confirmed co-localisation of GFP-labelled terminals and VAMP1 IF. Tessellation-based Mander's co-localisation analysis of 160 terminals from three individual ROIs validated a strong overlap of areas containing VAMP1 IF signal with GFP-labelled terminals (calyceal terminals). In comparison, the median co-localisation of GFP and VAMP2 immunofluorescence was significantly reduced.

Accordingly, from here on VAMP1-rich terminals and VAMP2-rich areas will be addressed as calyceal and extracalyceal terminals, respectively.

While the extracalyceal origin alone does not allow to speculate on the characteristics of the respective terminals, the dominance of vGluT2 (details below) in these terminals pointed towards glutamate being the sole or at least one of a combination of neurotransmitters in this type of terminal. At first glance, this rules out the possibility that the extracalyceal terminals described here are identical to the VAMP2- and VGAT-positive - and therefore inhibitory - extracalyceal inputs that were identified by Schulz[176]. However, VGAT and vGluT2 double-positive neurons that co-release glutamate and GABA have been described [191,192], as does evidence that implicates glutamate in inhibitory signaling[193,194]. Unfortunately, vGluT2 IF was not probed in the work of Schulz and the anti-VGAT antibody that I tested did not give rise to any discernible presynaptic signal around the principal cell (data not shown). Therefore, it was not feasible to test whether the extracalyceal terminals at question are identical.

3.3.4 Validation of the VAMP1/VAMP2 Ratio as a GFP Proxy

To avoid the time and effort that is necessary to generate GFP-transduced MNTB tissue and comply with the 3R principle[195], I tested whether the ratio of the two VAMP paralogs within a terminal could serve as a GFP proxy to identify the identity of a respective neuron in the absence of GFP, e.g. in wild-type tissue. Based on the visual classification of terminals a VAMP1 to VAMP2 ratio of 6.59 ± 5.27 and 0.42 ± 0.09 was measured for calyceal terminals and extracalyceal terminals, respectively. The latter was rounded to 0.5 and used as an initial threshold to classify terminals of GFP-containing tissue. A GFP content of 11.5 ± 10.3% (compared to the GFP-richest terminal) was obtained for extracalyceal terminals and rounded to a potential cut-off value of 10% (data not shown). Both classification methods were applied to identical data and showed no

significant differences in the average protein density of calyceal and extracalyceal terminals (Figure 3.16):

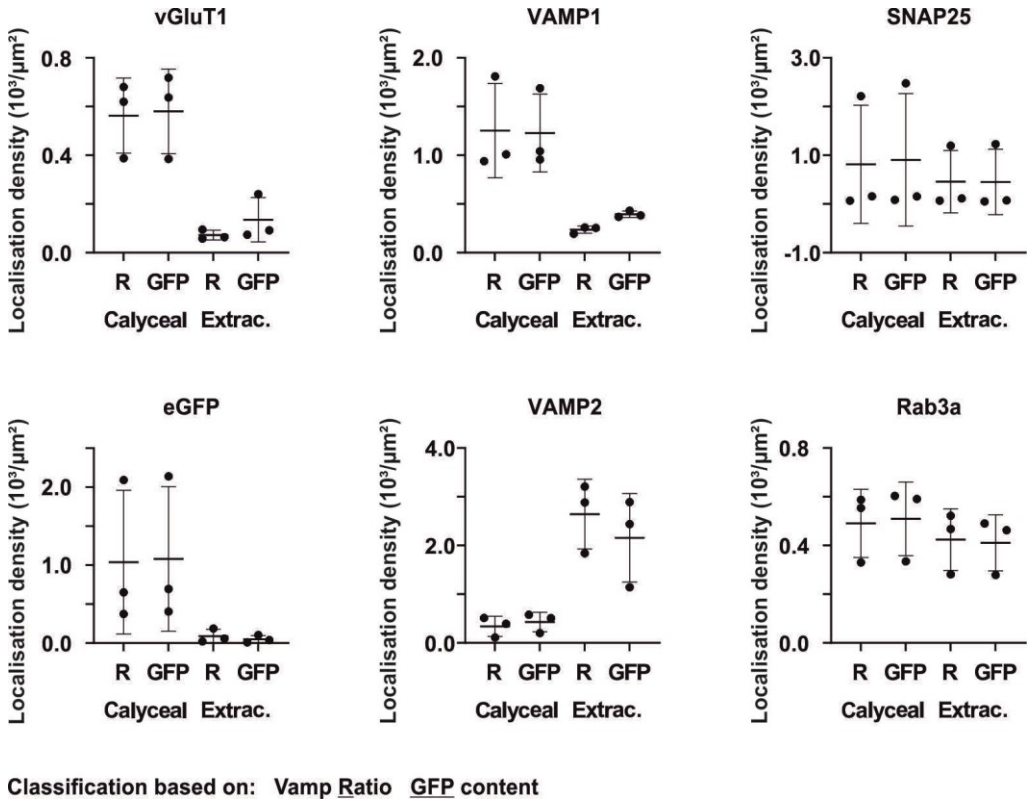

Figure 3.16 Comparison of terminal classification via VAMP ratio and GFP content. As a substitute for GFP labelling of calyceal projections, the ratio of VAMP1 and VAMP2 was evaluated as a means to distinguish calyceal from extracalyceal terminals. Both methods detected no significant differences in the protein expression patterns obtained. Data points represents individual animals; Mean ± StD; for statistics see Table 7.1.

Since the StD between individuals was in the same order of magnitude as the effect size of protein density differences between terminal types, normalisation to the respective calyceal protein density was performed to obtain a more faithful depiction of density differences (Figure 3.17). Irrespective of the classification method the density differences of vGluT1, VAMP1 and, importantly, GFP remained significant and showed minimal deviation. Due to a high StD stemming from a common experiment, the ratio-based density of SNAP25, VAMP2 and Rab3a in extracalyceal terminals was not significantly different to the protein density in calyceal terminals but grouped closer to the results obtained for extracalyceal terminals.

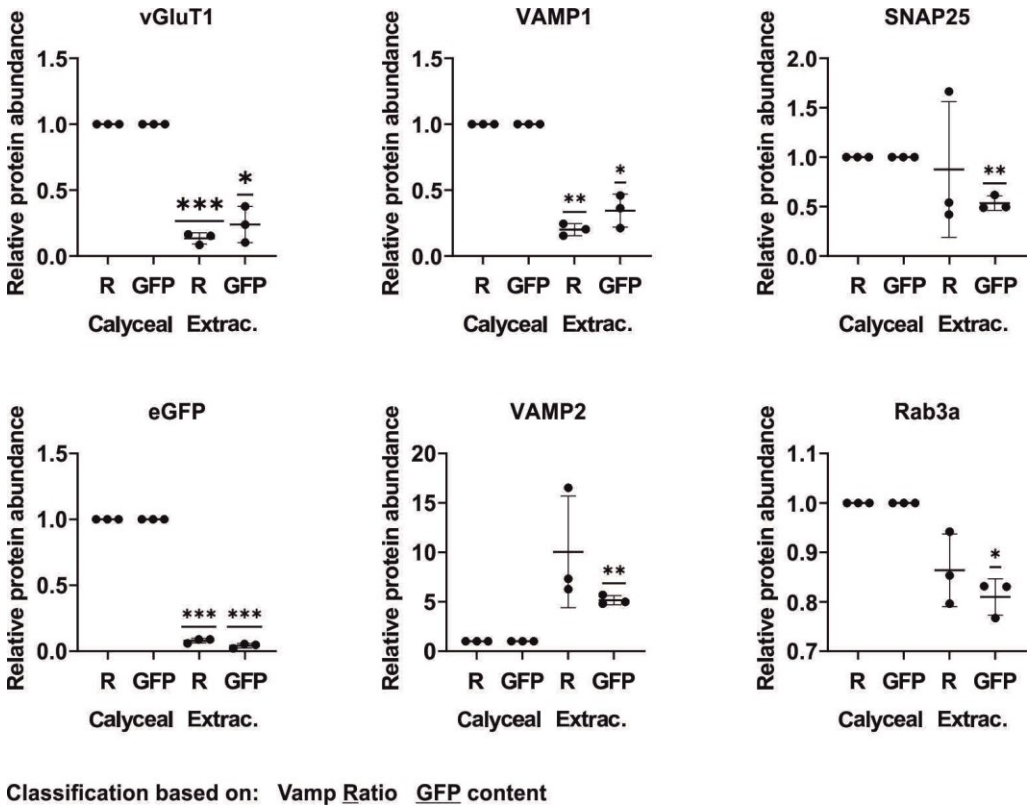

Figure 3.17 Normalised comparison of terminal classification via VAMP ratio and GFP content. Classification differences were uncoupled from the variance between individual animals by normalisation of the data to calyceal protein densities. Protein expression levels were consistent with both methods, except for SNAP25, VAMP2 and Rab3a results from a common experiment. Data points represent individual animals; Mean ± StD; for statistics see Table 7.1.

Taken together, the VAMP ratio is not a perfect GFP substitute on the level of single terminals yet allows for a terminal classification with minimal effect on protein distribution results when larger datasets are pooled. This is reflected by the frequency of terminal types, of which a portion of 64.9 ± 9.4% of terminals was identified as both calyceal and GFP-positive, 22.6 ± 1.9% of terminals as extracalyceal and GFP-negative, a subset of 9.7 ± 8.1% as calyceal but GFP-negative, and only a minor fraction of 2.8 ± 1% was identified as extracalyceal and GFP-positive (Figure 3.18). This would imply a margin of error of 12-15% which needs to be taken considered when assessing effect sizes. With this in mind, the VAMP ratio was used for all subsequent analyses.

For future endeavours, precise thresholds might need to be evaluated on a case-by-case basis due to varying antibody characteristics and sample preparations.

Figure 3.18 Dependence of terminal type frequency on identification method. The majority of terminals were identified unambiguously, irrespective of the classification method. Data points represent individual animals; Mean ± StD; for statistics see Table 7.1.

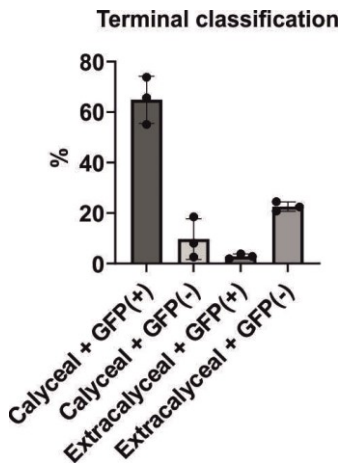

3.4 Comparison of Calyceal and Extracalyceal Terminals

The existence of calyceal and extracalyceal terminals that are both glutamatergic in nature and contacting the same postsynaptic entity provided the unique opportunity to study glutamatergic signalling architecture of different neuronal cell types within the same frame of reference. It allowed to compare protein expression levels, synaptic organisation and cellular geometries in the absence of experimental variables such as antibody performance, tissue preparation or biological context. To compensate for the margin of error described in 3.3.4, for the subsequent analyses data from the maS³TORM experiments using untreated and GFP-transduced animals was pooled where feasible. To account for possible effects of the GFP expression on protein distribution and density, experiments of tissue with and without GFP content are indicated by green and black symbols in the following figures, respectively.

Across the 6 experiments, 76.6 ± 2.7% of terminals were identified as calyceal terminals, whereas 23.4 ± 2.7% displayed a VAMP ratio indicative of extracalyceal terminals (Figure 3.19a). Calyceal terminals were significantly larger and more variable in area than extracalyceal terminals (2.16 ± 0.98 µm² vs. 0.79 ± 0.07 µm², respectively; Figure 3.19b) and more elongated as is indicated by the circularity (0.65 ± 0.07 vs. 0.72 ± 0.06, respectively; Figure 3.19c). This reflects the morphological differences of the digit-like calyceal stalks and swellings, present in these tissue slices at random cross-section angles, compared to the classic bouton-shape of the extracalyceal terminals (Figure 3.19d).

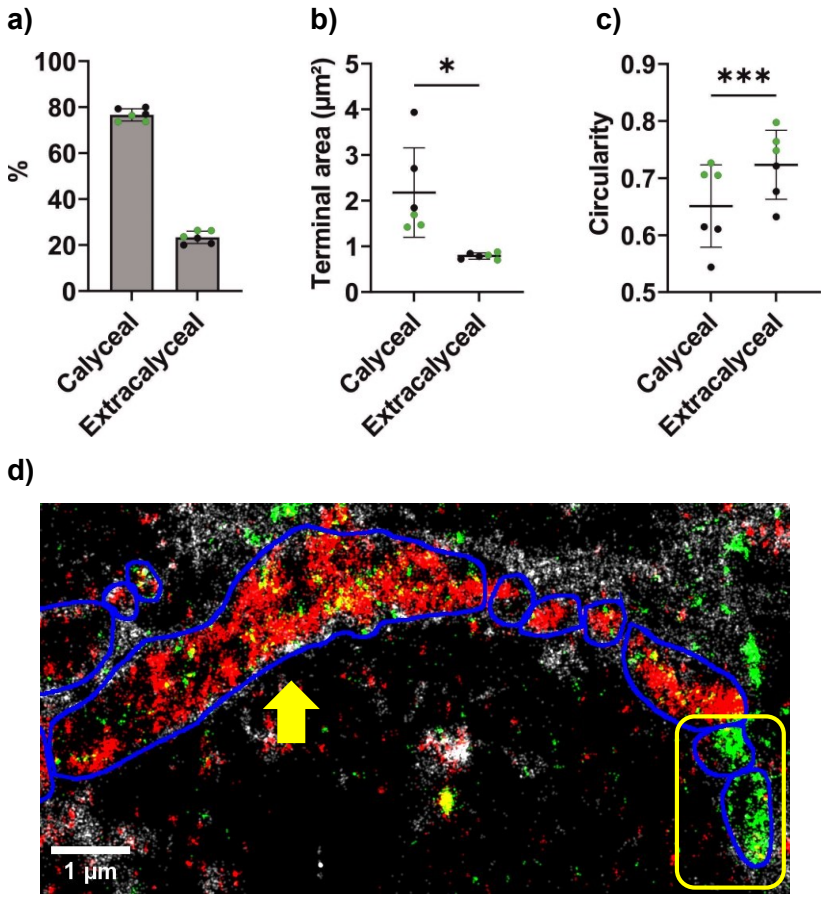

Figure 3.19 Calyceal terminals are more abundant and morphologically divers. Nearly 80% of terminals in contact with the principal cell were identified to be calyceal terminals (**a**), which were larger and more variable in size (**b**) and less compact than extracalyceal bouton-type terminals (**c**). Example of calyceal stalk and swellings as well as extracalyceal terminals (**d**). Merged MaS³TORM images of VAMP1 (**red**), VAMP2 (**green**) and WGA (**grey**) as well as terminal segmentation (**blue**). The elongated calyceal stalk (**arrow**) is clearly distinguishable from smaller terminals by its morphology. Extracalyceal terminals (**box**) closely resemble calyceal swellings in shape and size. Data points represent individual animals; Mean ± StD; for statistics see Table 7.1.

As I have shown above, calyceal terminals were rich in VAMP1 (0.14 ± 0.04 a.u.) and co-expressed VAMP2 at low levels (0.04 ± 0.04; Figure 3.20). Conversely, high amounts of VAMP2 (0.23 ± 0.09) were found in extracalyceal terminals with VAMP1-levels (0.04 ± 0.04) not exceeding those found in the postsynaptic nucleus (data not shown). vGluT2 was expressed in the two terminal types at similar levels, while vGlut1 was exclusively found in calyceal terminals (0.05 ± 0.02 vs. 0.01 ± 0.002). The expression of a variable composition of the two VAMP paralogs as well as both vGluT paralogs in calyceal terminals might be a means of the aforementioned structural diversity of the calyx which is hypothesised to disperse arriving actions potentials between AZs of low P_R (~25-40%[196]) to ensure sustained fidelity[181]. On the other hand, the extracalyceal terminals are likely of modulatory function where short-term depression might be employed as a form of input integration[197]. This synapse type is typically characterised by a higher

P_R of which the expression of VAMP2 and vGluT2 is indicative for[54,56]. Fittingly, a transmission success rate of >50% has been reported for excitatory extracalyceal terminals[81] and a matching expression pattern is evident from my data. In agreement with Figure 3.12, Rab3a was mildly but significantly reduced in extracalyceal terminals (0.07 ± 0.03 vs. 0.06 ± 0.02). No significant differences were detected for Synaptophysin, SNAP25 and SV2abc. Generally, protein expression levels appeared to be independent of GFP expression, with the possible exception of Rab3a which showed a tendency towards lower expression levels in both terminal types. Normalisation of the data eliminated this tendency (compare Figure 3.21).

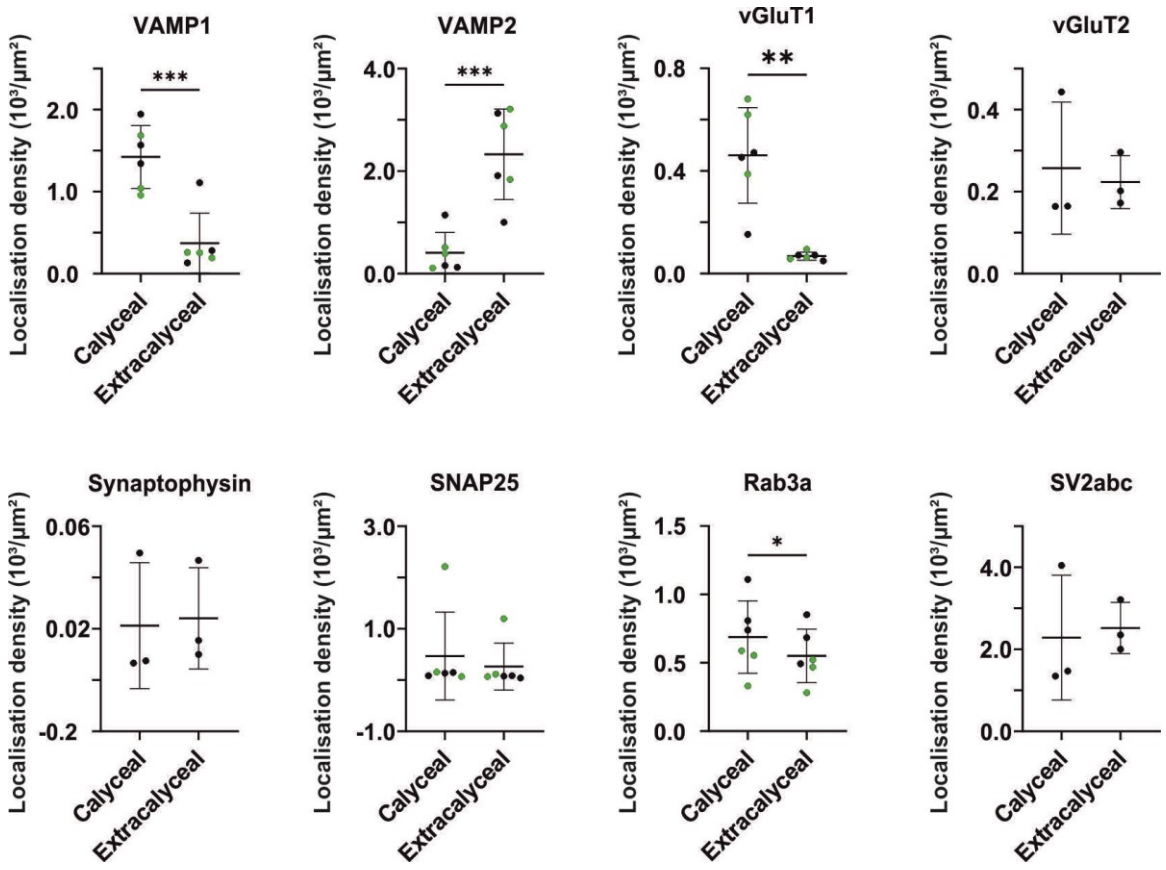

Figure 3.20 Protein density differences of calyceal terminals and extracalyceal terminals. Expression levels of VAMP1 and VAMP2 as well as vGlut1 drastically deviated between terminal types, indicating functional differences. Data points represent individual animals; Mean ± StD; for statistics see Table 7.1.

Normalisation of the data set to calyceal expression levels confirmed VAMP1 to be present in terminals at a significant ~4-fold higher abundance, whereas VAMP2 in extracalyceal terminals exceeded calyceal levels by a factor of ~8.8 (Figure 3.21). vGluT1 in extracalyceal terminals was reduced 5.6-fold and Rab3a reached 82 ± 12% compared to the expression level in terminals. The elevated levels of Rab3a in calyceal terminals could ensure the fast recovery of AZs by

release of SVs from the reserve pool[198] or elevated SV priming[61], but expression differences were equalised by P21 (compare Figure 3.12). Insignificant deviation towards higher protein expression levels was measured for Synaptophysin and SV2abc in extracalyceal terminals, whereas SNAP25 showed the opposite distribution. The increased levels of SV2abc in extracalyceal terminals might be a hint towards an inhibitory function of these terminals, as Bae *et al.*[199] found ~20% higher levels of SV2a in inhibitory terminals of hippocampal cell cultures, which is in line with the 10.2% to 29.4% (total vs. normalised, respectively) higher levels in extracalyceal terminals measured here.

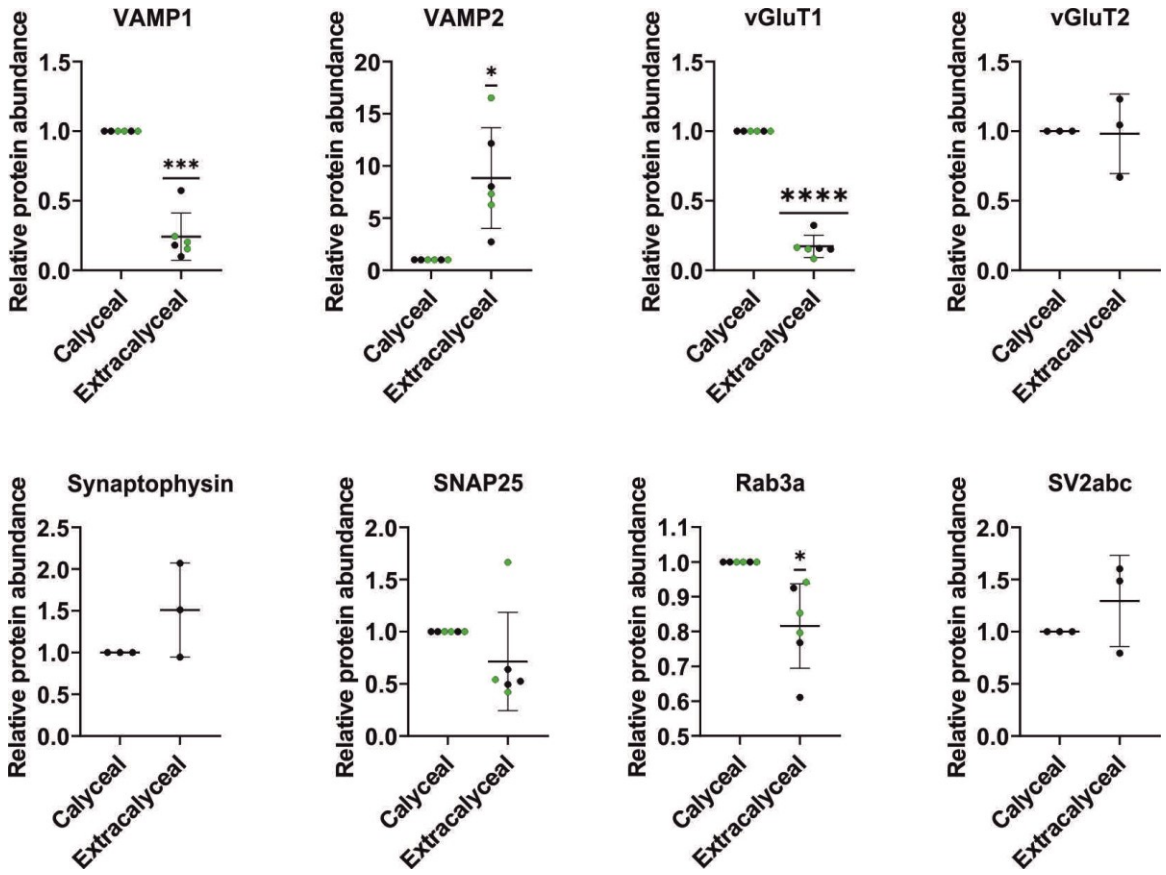

Figure 3.21 Normalised protein density differences of calyceal terminals and extracalyceal terminals. Classification differences were uncoupled from the variance between individual animals by normalisation of the data to calyceal protein densities. Data points represent individual animals; Mean ± StD; for statistics see Table 7.1.

Examples for the differences in distribution of VAMP1, VAMP2, vGluT1 and Rab3a between calyceal and extracalyceal terminals are shown in Figure 3.22.

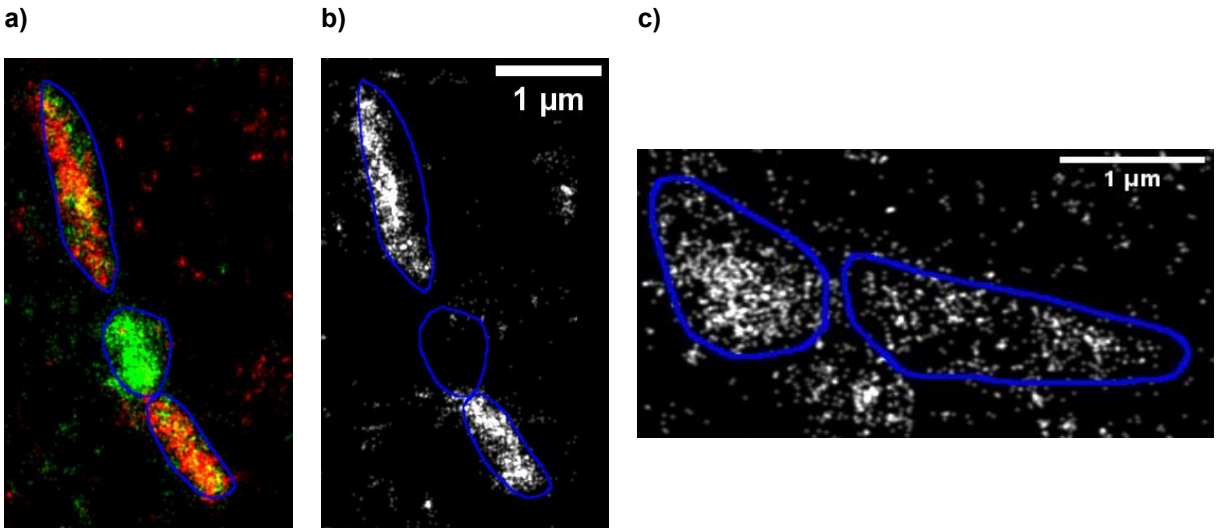

Figure 3.22 Examples of protein expression differences in calyceal and extracalyceal terminals. MaS³TORM images of VAMP1 (red) and VAMP2 (green) in calyceal (top and bottom) and extracalyceal (middle) terminals (a), vGluT1 (grey; b; FOV corresponding to a), Rab3a in calyceal (left) and extracalyceal (right) terminals (c).

In summary, the presented data paints the picture of two distinct types of synaptic contacts. I have shown that they differ in origin as well as morphological and protein appearance, which likely represents adaptations to distinct functionality. It will be interesting to see if future combinations of labelling, serial sectioning and/or imaging techniques will allow to pinpoint the exact origin(s) of these extracalyceal inputs. Complete identification of the neurotransmitter(s) that are released by this terminal type will be a first step towards the validation of whether the extracalyceal glutamatergic terminals characterised here are identical to the inhibitory inputs emerging from the VNTB that were identified by Albrecht *et al.*[80] or the projections of undefined origin described by Schulz[176].

3.5 Insights into the Glutamatergic Protein Distribution and Consequences for SV Pool Considerations

In this section, I will analyse the multiplexed data sets that were acquired with the maS³TORM microscope with regard to structurally distinct SV pools. Protein distribution perpendicular to the synaptic border are investigated using Line profiles, which were obtained from synaptic locations both with and without the presence of an AZ as well as calyceal and extracalyceal terminals. The line profiles are investigated by Gaussian approximation and by integration of the profiles over specific segments. Distributions lateral to the synaptic border are examined with a micro-segmentation approach.

3.5.1 Averaged Line Profiles provide a Cross-Section of Protein Distribution

To get an initial impression of the protein distribution along the orthogonal vector to the proximal border, line profiles from multiple line selections per category and experiment were averaged in Matlab to investigate generalised characteristics of the protein distribution. Examples are shown in Figure 3.23. SV proteins were noticeably enriched in the proximity of calyceal AZs. As demonstrated before, extracalyceal terminals were significantly smaller and as a result the bias of SV proteins towards the AZ was less pronounced. Conversely, likely due to the larger diameter of calyceal terminals, the enriched section was followed by a segment of lower but steady protein density towards the distal border of the terminal. In both terminal types the enriched segment trailed off ~400 nm inwards from the proximal border. Off-side of calyceal AZs the protein density lacked the bias towards the proximal border and resembled levels comparable to the distal end of the respective AZ-attached distribution. As expected from the previous section, vGluT1 and VAMP1 were measured at minimal levels in extracalyceal terminals, both in the presence and off-side of AZs. Upon visual inspection, VAMP2 levels in extracalyceal terminals closely resembled the distribution of VAMP1 in calyceal terminals, suggesting that they might serve similar roles in their respective terminal type. Little difference was found for the distribution of Rab3a between AZ- and off-side areas, both in calyceal and extracalyceal terminals. Lastly, the difference of peak levels of SV2abc between AZ- and off-side areas was markedly more pronounced in calyceal than extracalyceal terminals.

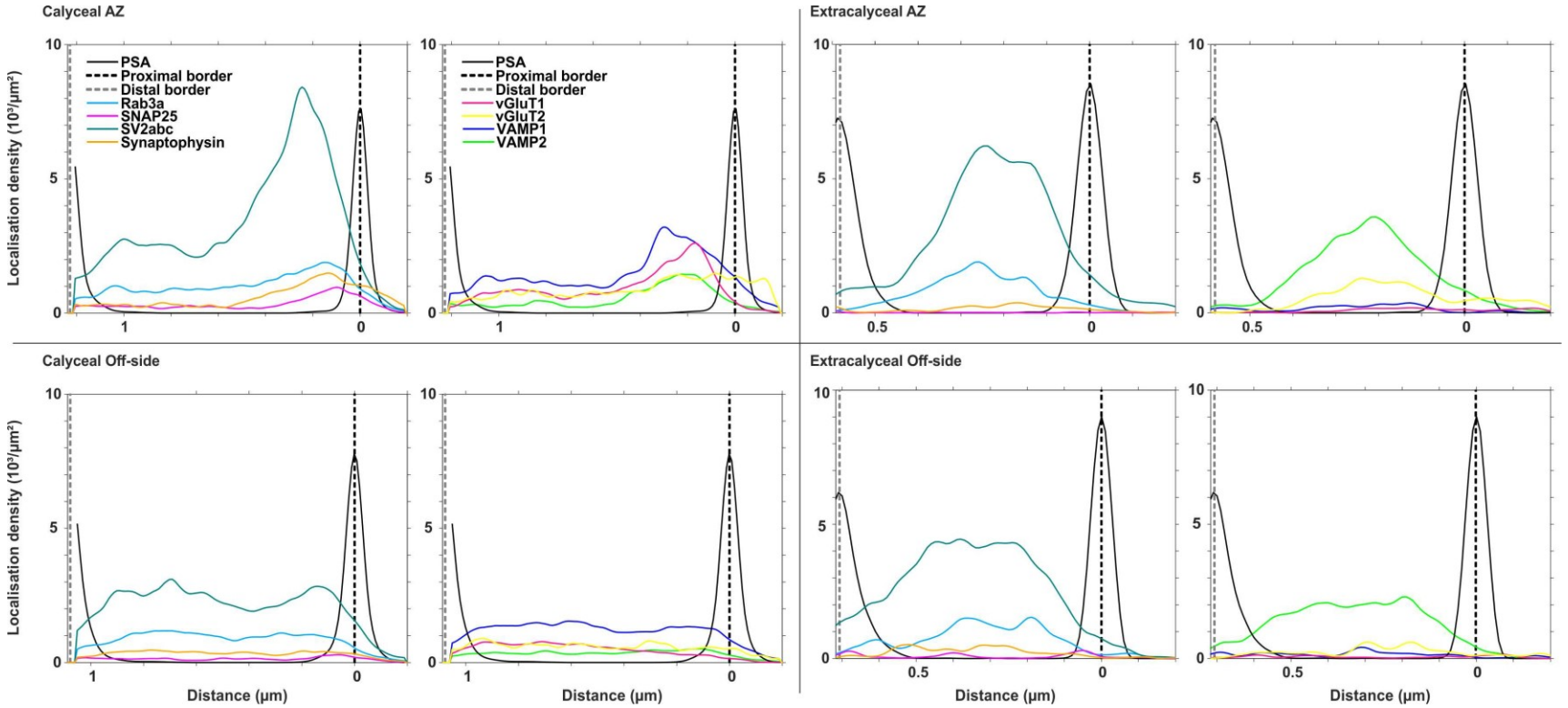

Figure 3.23 Examples of averaged and scaled line profiles from two types of presynaptic terminals. MaS³TORM images were generated from P12 tissue and terminals were segmented. Line selections were drawn through SV clouds attached to AZs and off-side of AZs (see right-hand side comic). Resulting protein distribution line profiles were aligned at the proximal (synaptic) and distal terminal borders and averaged. Example profiles shown here were averaged from 68 (calyceal AZ), 8 (extracalyceal AZ), 54 (calyceal off-side) and 10 (extracalyceal off-side) individual profiles of one animal. Detailed statistics are provided in Table 7.1.

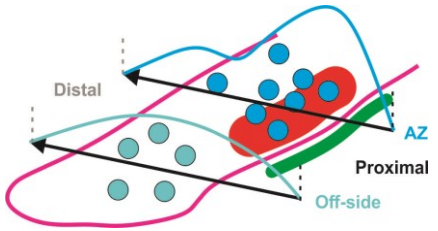

In many cases, AZs were easily identifiable by the enriched IF presence of the synaptic cytomatrix proteins Bassoon/Piccolo and Homer1bc on one side of the presynaptic cleft, each, as seen in Figure 3.24. While Bassoon/Piccolo was confined to presynaptic terminals in the majority of cases, to our surprise Homer1bc frequently appeared on both sides of the presynaptic cleft, although usually at lower quantities than in the principal cell. This could be an effect of non-orthogonal viewing angles or tissue-cutting artefacts. However, IF of both Bassoon/Piccolo and Homer1bc was also found throughout the entire presynaptic terminal, again at low quantities. Whether this was the result of a yet undefined pool of proteins of unknown presynaptic function, protein that is trafficking to its target location, or displayed unspecific background could not be determined.

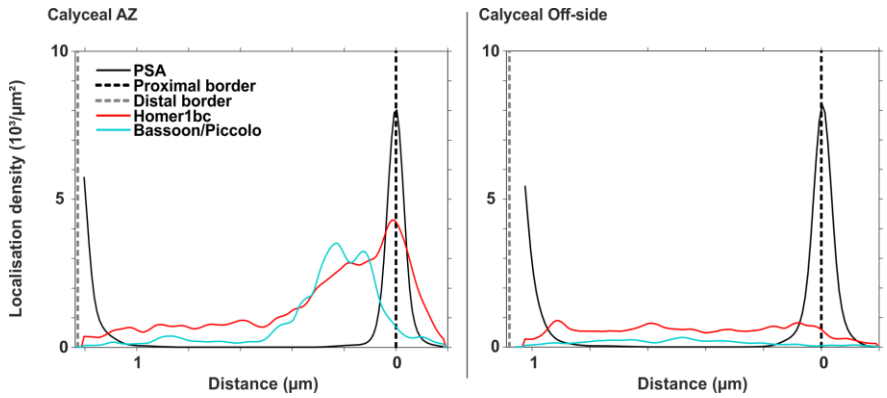

Figure 3.24 Immunofluorescence of synaptic cytomatrix proteins Bassoon/Piccolo and Homer1bc was strongly enriched at calyceal AZ positions. Areas off-side of AZs did not show an enrichment of cytomatrix proteins, but low levels of Bassoon/Piccolo and Homer1bc IF were widespread.

In summary, the line profile analysis revealed an AZ-dependent enrichment of SV proteins within the initial ~400 nm from the proximal border, along with a more generalised, evenly distributed ("basal") presence of SV proteins both in the distal parts of the calyx and off-side of AZs. Presumably due to their smaller size, the basal protein presence was not observed in extracalyceal AZ segments.

3.5.2 Protein distribution visualized by Gaussian Analysis

As mentioned, the distribution curves displayed above (Figure 3.23) showed a bell curve-like enrichment with a bias towards the proximal border for most proteins investigated here. A frequently used method to analyse protein distribution curves is approximation by a Gaussian fit (Figure 2.5). Distance of Gaussian centres from the proximal border and the FWHM as a measure of dispersion are shown in Figure 3.25.

As expected, Homer1bc as a postsynaptic density protein was predominantly located close to the proximal border (61.7 nm and 8.2 nm for calyceal and extracalyceal terminals, respectively) with IF signal extending to both sides of the border. The combined IF signal of the presynaptic cytomatrix proteins Bassoon and Piccolo was found only 117.4 nm and 72.5 nm (calyceal and extracalyceal terminals, respectively) inwards of the proximal border. This equates to a peak-to-peak distance of Homer and Bassoon/Piccolo of ~60 nm, which is significantly less than the ~140 nm that we have reported previously using DNA-PAINT[136]. In contrast, the FWHM of Homer1bc and Bassoon/Piccolo profiles was measured at 278.4 nm/167.5 nm and 181.3 nm/219.2 nm (calyceal/extracalyceal, respectively) which is at least twice the dispersion that we have previously found based on DNA-PAINT (82 nm and 85 nm for Bassoon and Homer, respectively)[136]. A possible explanation could be that the AZs that were analysed here differed in orientation with respect to the imaging plane. In addition, the line selections might not have extended over the proximal border and into the postsynaptic space sufficiently to capture the main peak of the Homer1bc distribution along this vector. The typical sandwich appearance of Homer and Bassoon/Piccolo with its highly conserved spacing in between[136,200,201] might have been missed due to these experimental choices. To verify this assumption and determine the exact orientation of AZs, analysis of serial tissue sections would have been necessary which was beyond the scope of this thesis. The lack of Homer1bc and Bassoon/Piccolo in regions off-side of the AZ is indicated by Homer1bc's FWHM exceeding one micrometre for both terminal types and the overall low Gaussian fit quality (Figure 3.25, indicated by hollow marks) of both protein families, caused by the low and highly dispersed IF levels found in these regions (compare Figure 3.24). Whether this represents the actual presence of the protein or background fluorescence could not be determined.

Similar complications were found for SNAP25, which was often discontinuously distributed and therefore yielded exceptionally low fit regression scores (see Figure 2.4, left graph). Nevertheless, an insignificant yet appreciable trend towards a more distal localisation of SNAP25 was visible for calyceal AZ areas.

The distribution of the remaining SV proteins was found to peak in a region between 200 nm and 300 nm from the proximal border in areas with an AZ present and FWHM of ~300-400 nm were measured. Regions off-side of AZs lacked the bias towards the proximal border and as a result the distribution peak was located further recessed and the distribution, represented by the FWHM, often appeared more disperse.

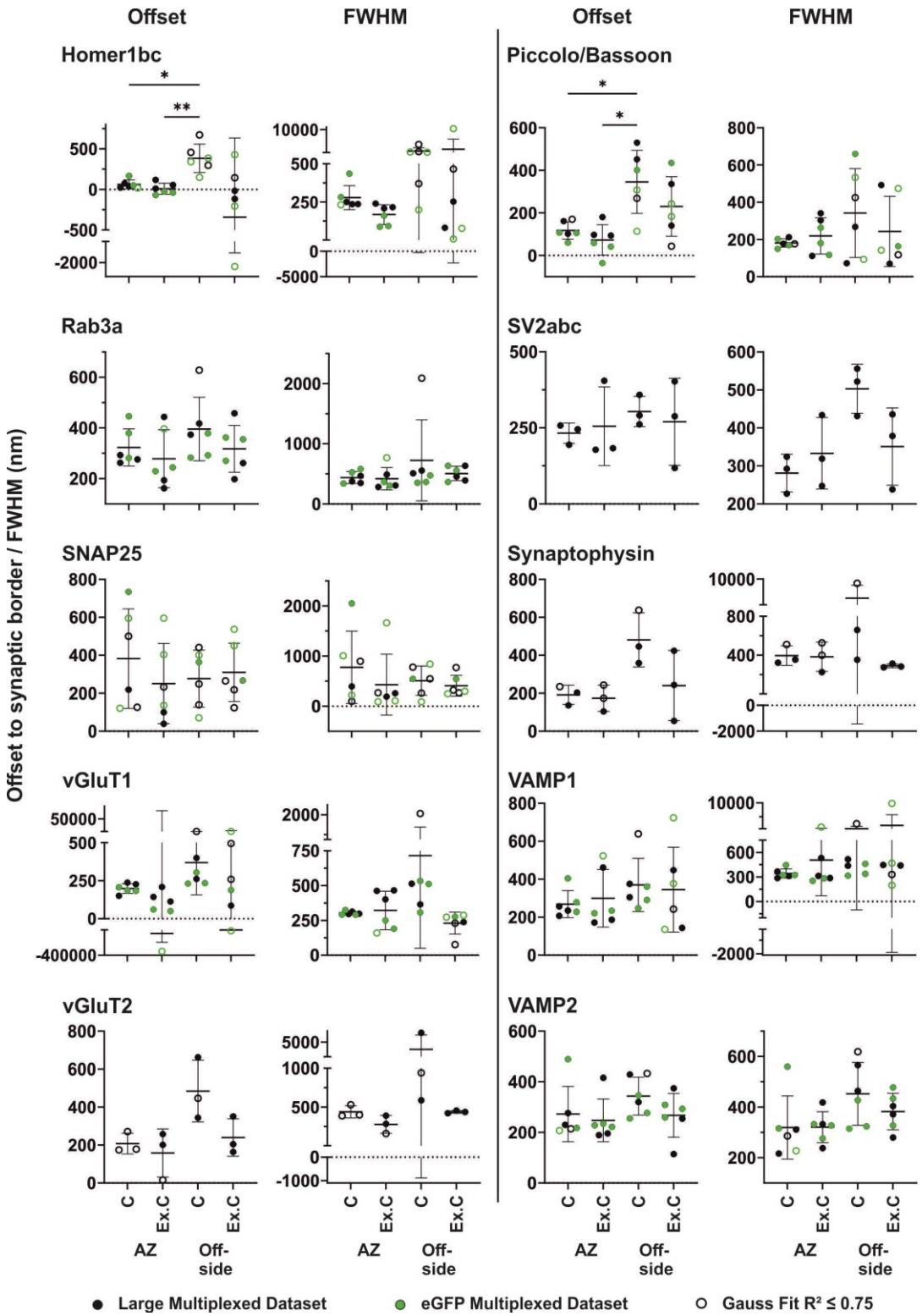

Figure 3.25 Gaussian analysis of unscaled protein distribution curves. A Gaussian approximation was fitted to the line profiles of the previous section. The offset between the Gaussian peak and the proximal border as well as the full width at half maximum (FWHM) of the distribution peak were measured as estimates of protein location and dispersion. Data points represent individual animals and code for the

experiment type and Gaussian fit score; C: Calyceal, Ex.C: Extracalyceal; Mean ± StD; for statistics see Table 7.1.

The findings above correlate well with the results that we have obtained previously in our proof-of-concept study of the maS³TORM microscope[92], where Homer signal at AZs extended over the presynaptic border as well (Figure 3.26). Bassoon (in the previous study stained for separately) peaked ~80 nm inwards from the presynaptic border and the FWHM measured ~200 nm. The enrichment of vGluT1 at the AZ reached off-side levels at a distance of ~400-500 nm inwards from the proximal border and Synaptophysin was lightly enriched in proximity of AZs but appeared throughout the entire terminal, indicating that SVs are present in higher numbers at the AZ, but not abolished at the distal end of the terminal. This distribution is also in line with EM reconstructions[202].

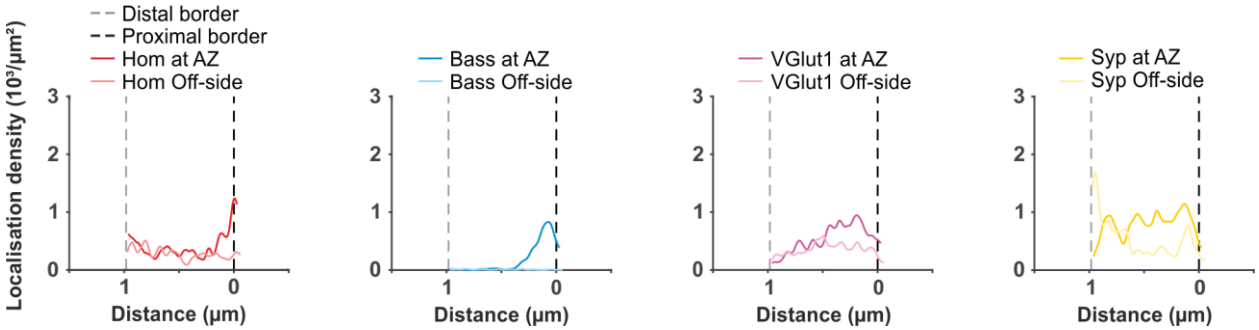

Figure 3.26 Present results agree with previously obtained protein distributions. In Klevanski *et al.* we reported similar distributions of the synaptic proteins Homer (**left**), Bassoon (**centre-left**), vgluT1 (**centre-right**) and Synaptophysin (**right**) as obtained in the presented experiments. (modified from Klevanski *et al.*[92])

In conclusion, the Gaussian analysis further substantiated the purely visual findings from 3.5.1. Except for SNAP25, a clear enrichment of all SV proteins within the initial ~350-500 nm from an AZ was measured.

3.5.3 Examination of Spatially Distinct SV Pools

Assuming that SV pools are (passively) spatially segregated, the reserve pool of SVs would be expected to be located away from the AZ. Translated to the orientation that I analysed in this study, this would equate to a position towards the distal end of a synaptic terminal. Considering the results from 3.5.1 and 3.5.2, where accumulation of SV proteins towards the AZ in conjunction with a basal occurrence of SVs was found, it was unclear whether this basal population of SV needed to be attributed to the adjacent AZ or its presence was structurally unrelated, potentially as part of the suggested super pool of SVs[40]. I therefore conducted two separate analyses: 1)

covering the entire width of the terminal and 2) confined to the SV-enriched area from previous results, which is therefore omitting the basal population.

To quantify the protein distribution in different segments of the previously introduced line profiles, I fitted three sequential integrals to the data. To account for the variable width of terminals in the first part of the analysis, I scaled the line profiles to match their proximal and distal borders. The scaled profiles were then split into three sections of equal but arbitrary size to get an impression of the relative protein architecture of the entire SV population. Synaptophysin is present on virtually all SVs[53] and was used as an SV distribution proxy. Synaptophysin IF results (Figure 3.23 and Figure 3.26) confirmed that SVs potentially span the entire presynaptic terminal from the proximal AZ to the distal border. The distributions of all investigated proteins were probed against Synaptophysin IF to reveal local enrichment or scarceness of proteins in the SV pool, which would be an indication towards specific pool markers. Generally, molecular SV pool markers might be acting in multiple ways: a marker could decrease the likelihood of an SV to participate in the SV cycle by blocking entry to the SV cycle as it was shown for SNAP25[41], which would predict a presence more distal to the AZ. Alternatively, a marker could increase the probability of release (e.g. Rab3-dependent superpriming[61]), in which case a distally reduced presence would be expected. Conversely, the absence of a marker could allocate an SV into a specific SV pool by excluding it from a certain interaction.

As expected from the previous analyses, all proteins in the calyx, except for SNAP25, were markedly enriched in proximal segments containing an AZ and significantly reduced in the distal counterpart (Figure 3.27). The bias towards the AZ was especially pronounced for SV2abc, Synaptophysin, vGluT1 and vGluT2 and, although to a lesser extent, for VAMP1 and VAMP2. The latter might be explained by their participation in the SNARE complex, which could restrict access to the epitope that is recognised by the respective pAB. The fraction of VAMP proteins that engage in SNARE complex formation compared to the total amount present on an SV (~70[53]) has not been determined, yet. In areas off-side of AZs, proteins were equally abundant in proximal and medial segments. A significant reduction in distal segments was still observed for both VAMP paralogs, vGluT1 and Rab3a.

Compared to the general SV abundance as estimated by the Synaptophysin distribution, SNAP25 was significantly reduced in segments proximal to the AZ and increased at the distal end. This finding is in line with the prediction from above (based on Truckenbrodt *et al.*[41]) and an indication that spatial sorting of SV pools might exist. However, the medial reduction in segments off-side of AZs is not readily explained by the maturing SV hypothesis. Interestingly, this spatial

organisation was also not observed in extracalyceal terminals, where SNAP25 was distributed evenly. In addition to SNAP25, Rab3a and VAMP1 were significantly less abundant in segments proximal to an AZ than the general SV population predicted. At the AZ, Rab3a in its GTP-bound form is associated with the SV membrane and involved in the initiation of SNARE complex formation[203]. Additionally, Rab3 isoforms have been reported to boost the Ca^{2+} sensitivity of a subset of SV, termed superpriming. Thus, an increased abundance of Rab3a towards the AZ appeared more likely. Equivalent to the VAMP paralogs, engagement in SV docking at the AZ might mask epitopes on Rab3a and explain the contrasting results. In addition, the employed pAB might recognise both the SV-associated and soluble state of Rab3a, which would explain the more even distribution throughout all terminal areas (also compare Figure 3.23).

SV2abc was significantly reduced in the distal parts and Synaptophysin was significantly enriched in proximal parts of calyceal AZ segments, but not off-side or in extracalyceal terminals. Synaptophysin is involved in the process of SNARE complex formation[59] as well as retrieval of VAMP2 to newly formed SVs after endocytosis[204], both of which are inherently associated with the proximal plasma membrane. Similarly, SV2 plays a role in the recruitment and regulation of Synaptotagmin which, the latter being the Ca^{2+} sensor of the SNARE complex, is also tightly linked to the AZ[64,205]. Elevated abundance of SV2 paralogs or Synaptophysin on an SV might therefore increase its probability for SNARE complex formation and subsequent release.

Irrespective of the terminal origin or the analysis approach (see Figure 3.28), vGluT paralogs were present in a significantly higher quantity proximal to an AZ compared to its distal counterpart. For vGluT1 this was also the case off-side of AZs, while vGluT2 was evenly distributed off-side in calyceal terminals and only mildly biased towards the proximal side in extracalyceal terminals. The stronger tendency of vGluT1 to be located close to AZs might be mediated by its ability to interact with Endophilin A[57], which in turn is anchored around AZs via Intersectin-1[206,207]. The same interaction has been reported to reduce the super pool of SVs[208] and causes the reduced P_R of vGluT1 compared to vGluT2 by blocking Endophilin's positive regulation of SNARE complex formation[207]. In addition, vGluT1 functions in the sorting of other SV proteins to newly retrieved SVs during endocytosis (e.g. Synaptophysin and VAMP2)[209] and recycles independent of vGluT2[210], which might explain how SV identity is maintained after exocytosis. The multitude of mechanisms in which vGluT1 is involved and the separate recycling pathways nominate vGluT1 as a prime candidate for a molecular marker, however, specific enrichment in a subpopulation of SVs was not apparent.

In contrast, VAMP1 was significantly reduced in segments proximal to an AZ compared to the general SV abundance. VAMP2, on the other hand, did not exhibit this distribution. At the calyx of Held, two distinct pools of SVs were identified based on their release kinetics after depolarisation[211]. Equally, VAMP1- and VAMP2-containing SVs have been reported to exhibit different P_R, where VAMP2 is associated with the higher P_R[54]. This is likely due to the VAMP2-Synaptophysin complex formation[59], which additionally might provide an advantage for SV docking in areas of high competition and could therefore explain the higher presence of VAMP2 in close proximity of an AZ. As a result, VAMP1-containing SVs might be located more towards the periphery of the AZ. Synaptophysin also specifically recruits VAMP2 to newly retrieved SVs[27], hence different recycling pathways could be involved[212], which might explain the different recovery rates that were reported for the slow and fast-releasing SV pool in the calyx[50]. Woelfel *et al.* hypothesised that differences in the release machinery must be causing the observed release kinetic differences[49]. Differentially regulated formation of the SNARE complex due to different VAMP paralogs would fit this model.

In extracalyceal terminals, the protein distribution did not deviate from the estimated SV population and protein distributions in areas with or off-side of AZs were closer resembled.

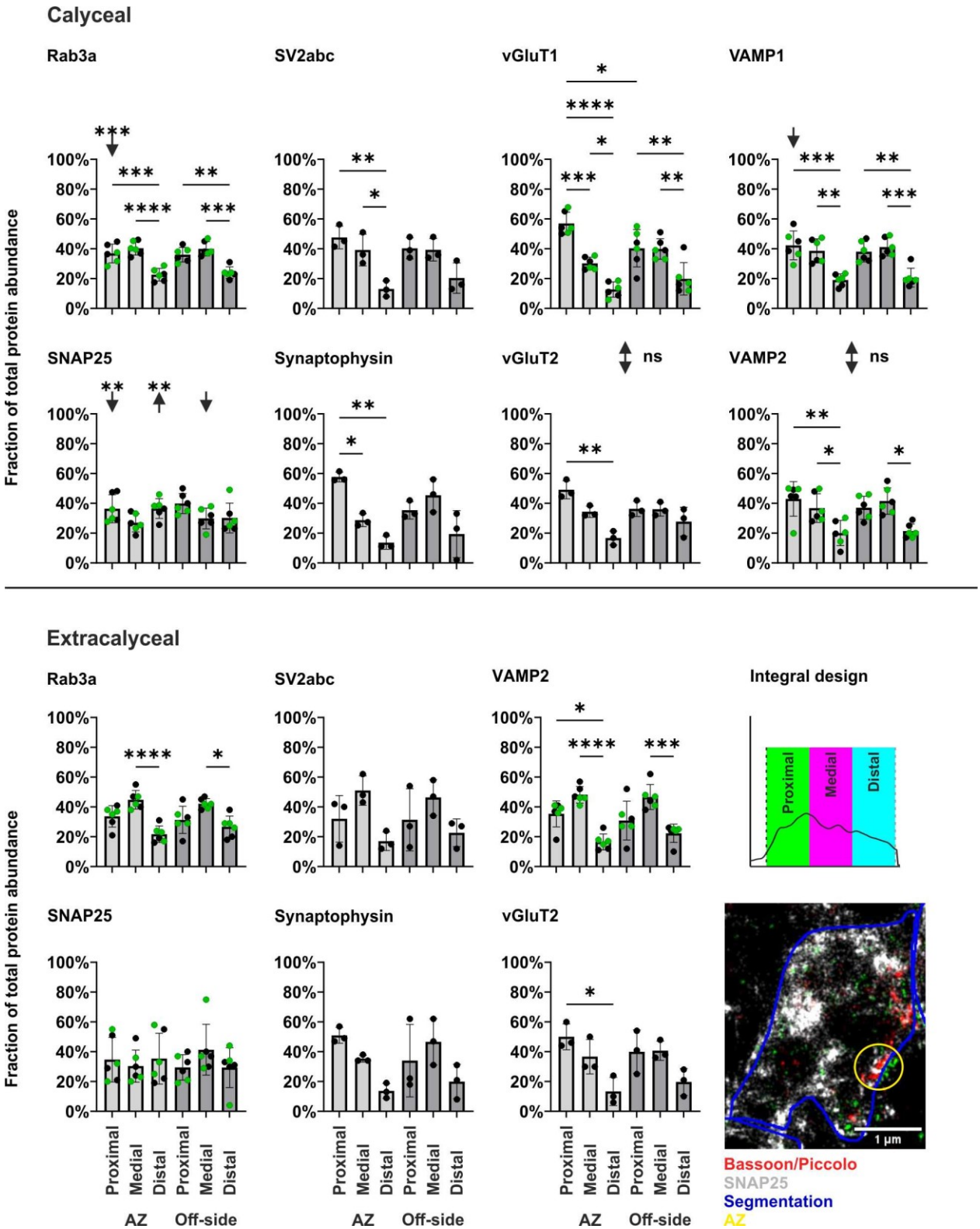

Figure 3.27 Integration of line profiles to assess structure of protein distribution throughout entire terminal. The line profiles from the previous section were integrated over three segments to compare the protein distribution in distinct sections of the presynaptic terminal (see integral design). Example shows merged maS³TORM images of calyceal terminal. SNAP25 is present directly at the AZ (**yellow circle**) and in the distal parts of the terminal. Significance bars represent one-way ANOVA of protein abundance

between all sections of a respective graph. Arrows indicate deviation of protein abundance from estimated SV abundance in the respective segment. The three sections per category add up to 100%, respectively; Mean ± StD; for statistics see Table 7.1.

The second part of this analysis focussed on the SV-enriched terminal area as identified in the previous section (Figure 3.23 - Figure 3.26). Three consecutive integrals of 200 nm width, each, were fitted to the line profiles, starting at the proximal border of the terminal. Because of the defined width of the integrals for this part of the analysis, line profiles were not scaled to align at both terminal borders and therefore absolute spatial information was retained. The width of 200 nm per integral was chosen based on the elevated presence of the cytomatrix proteins Bassoon/Piccolo within the proximal ~200 nm of the terminal, and the decline of the SV accumulation between ~400 nm to ~600 nm inwards of the AZ. In case the basal population of SV does not contribute to the RP, molecular markers for the RP which were obscured by the basal population before should be uncovered with this integral layout.

Generally, the protein distribution in extracalyceal terminals appeared highly similar to the results obtained for the whole terminal width, likely because extracalyceal terminals rarely exceeded the width of 600 nm (compare Figure 3.19 and Figure 3.23), which was probed in this second part of the analysis. In calyceal terminals, the protein distributions appeared less inclined towards the proximal border as a result of omitting the basal SV population. In regions off-side of AZs, except for SNAP25, a pronounced focus of protein abundance towards the medial segment was observed.

Again, the protein distribution in extracalyceal terminals did not significantly deviate from the SV distribution as approximated by Synaptophysin IF. The elevation of SNAP25 protein abundance in distal parts of AZ-containing regions, compared to the estimated SV population, was observed under these conditions as well, thus further strengthening the hypothesis that a SNAP25-labelled reserve pool is spatially segregated. Similarly, the significant reduction of Rab3a in proximal AZ regions was preserved, irrespective of the investigated terminal width. In addition, an increased abundance of Rab3a compared to the SV population was measured distal to AZs. An explanation for the latter observation might be that Rab3a-bound SVs, through its interaction with Tomosyn1[213], could be predominantly arrested at a medial distance to the AZ. Proximal VAMP1 deviation from the SV abundance was observed with both approaches as well.

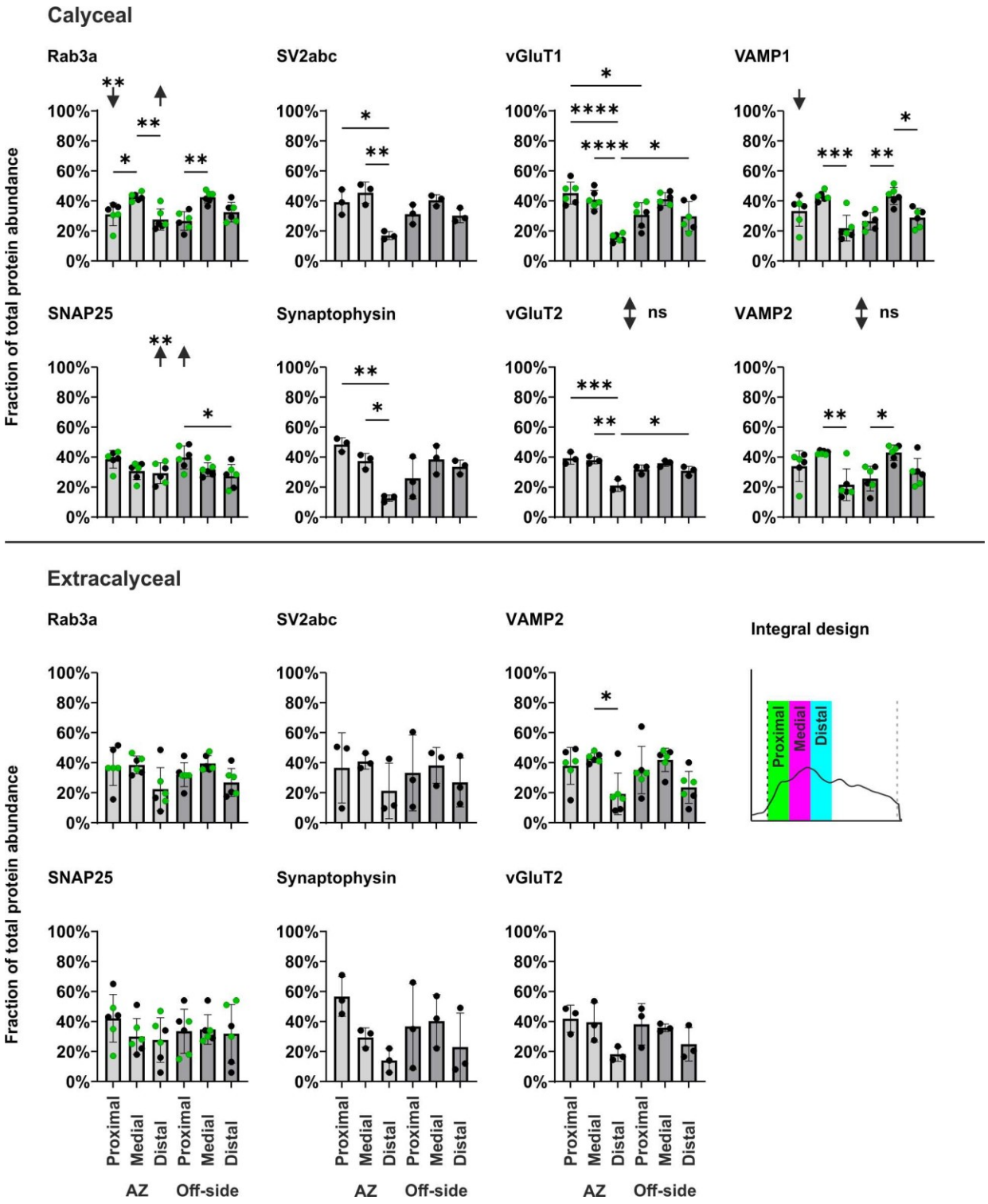

Figure 3.28 Integration of line profiles, restricted to a proximal width of 600 nm. Integration of the previously obtained line profiles was restricted to the area of raised SV abundance by fitting three integrals of 200 nm, each (see integral design comic). Significance bars represent one-way ANOVA of protein abundance between all sections of a respective graph. Arrows indicate deviation of protein abundance from estimated SV abundance in the respective segment. The three sections per category add up to 100%, respectively; Mean ± StD; for statistics see Table 7.1.

Irrespective of the analysis approach, the direct comparison of vGluT1 with vGluT2 as well as VAMP1 with VAMP2 in calyceal terminals did not reveal any significant differences. Nevertheless, minor differences between the distributions of both paralog pairs were observed, especially for VAMP1 in segments proximal to an AZ. This might indicate the sorting of the paralogs into separate SVs, at least to a limited degree. Since distinct recycling pathways have been described both for vGluT1[209] and -2[210] as well as VAMP1 and -2[27], occupancy of separate SV subpopulations appears plausible.

The results obtained for SNAP25 strengthen the argument for a spatial sorting of SV pools, possibly in a probabilistic, passive fashion. While Rab3a and VAMP1 in calyceal terminals also showed deviation from the estimated SV population, the proposed mechanisms of how they define potential SV pools are yet to be investigated.

The question of whether the basal population of SVs constitutes part of the super pool of SVs could not be clearly answered based on the results obtained for individual proteins. A reduced presence of vGluT1 at the distal end of calyceal terminals was observed, however, its presence was not significantly different than the overall SV population predicted. In addition, no significant difference in the distribution of vGluT2 was measured, which has not been implicated in super pool regulation. Taken together, the analysis of the line profiles both by Gaussian approximation beforehand and in this section strongly suggest that the majority of SVs is located within ~400-600 nm of an AZ. In an earlier EM reconstruction of rat calyces at P16, even lower AZ offsets of only up to ~250 nm were reported[214]. Since up to 80% of SVs have been reported to reside in the RP[215], according to these findings the RP must be located within or closer than these first 400-600 nm proximal to the AZ, which would render the basal population of SVs part of the super pool, indeed.

3.5.4 Examination of Laterally Structured SV Pools via Micro-Segmentation Analysis

In the previous section, the choice of line selection positions off-side of AZs was based on the abundance of SV clusters and not necessarily at a defined distance to the adjacent AZ. Therefore, this data did not allow to examine whether VAMP1 or Rab3a were localised more peripheral with respect to an AZ, or any other laterally organised SV pool structures exist. To investigate potential laterally structured SV pools, in this section I used a micro-segmentation approach, which assessed protein IF in spatially clearly defined areas around the AZ (see Figure 2.5 and Figure 2.6 for details).

The micro-segmentation approach used a grid of three by three segments. At the active zone, the width of the three lateral segments combined was matched to the width of the respective AZ. Off-side, the average AZ width of ~500 nm (data not shown) was used. Since extracalyceal terminals were significantly smaller than calyceal terminals, the off-side micro-segmentation grid frequently extended over the outward terminal borders and therefore did not yield sufficient data for analysis. The proximal and medial segment both spanned 100 nm into the terminal to focus on the area that likely contains the AZ cytomatrix framework and, according to EM studies[214], the majority of AZ-related SV clusters. In addition, the proximal segments can be expected to contain docked and primed SVs. As a reference of the total SV population along the examined vector, the final distal segments then covered the remaining distance to the distal terminal border.

In the presented experiments, Synaptophysin IF was weaker than the IF obtained from other targets, even though Synaptophysin is assumed to be highly abundant on the majority of SVs. This indicates a comparably low binding efficiency for the anti-Synaptophysin pAB that was used here. While on a larger scale, a low proportion of labelled targets is still sufficient to capture the overall relative distribution, my Micro-Segmentation analysis is focussed on significantly smaller areas and therefore required a more reliable SV detection, as incremental deviations have more weight in smaller samples. In addition, it was unclear whether the Synaptophysin epitope that is recognised by the employed pAB is fully accessible on SVs that are engaged in SNARE complex formation. Lastly, the effect of molecular crowding could influence detection rates in dense environments like the AZ. To compensate for the mentioned constraints, instead of relying on the Synaptophysin IF alone, the relative abundance of multiple SV markers (both vGluT and VAMP-1 and -2, SV2abc, SNAP25 and Synaptophysin) was averaged to minimise a potential bias.

Comparing the estimated SV distribution of calyceal and extracalyceal AZ areas, no significant difference was found between the two areas (Figure 3.29). In extracalyceal terminals, the medial centre (0.161 ± 0.069 a.u.) contained significantly more SVs than the proximal centre (0.105 ± 0.066 a.u.). This effect was more pronounced in calyceal terminals, both in areas centred around an AZ (Ø proximal: 0.1 ± 0.049 a.u., medial: 0.148 ± 0.0412 a.u.) and in the adjacent off-side areas (Ø proximal: 0,09 ± 0.046 a.u., medial: 0.133 ± 0.047 a.u.), where all three medial segments contained more SVs than the proximal segment. Potentially as an effect of the lower number of extracalyceal terminals that were found around the principal cell, the StD of its SV distribution was markedly larger than the one found for calyceal terminals. Overall, SVs appeared to be located predominantly in the medial segments, which fits with the report from EM data where the main peak of SV location was found ~80-100 nm inwards from the AZ[214].

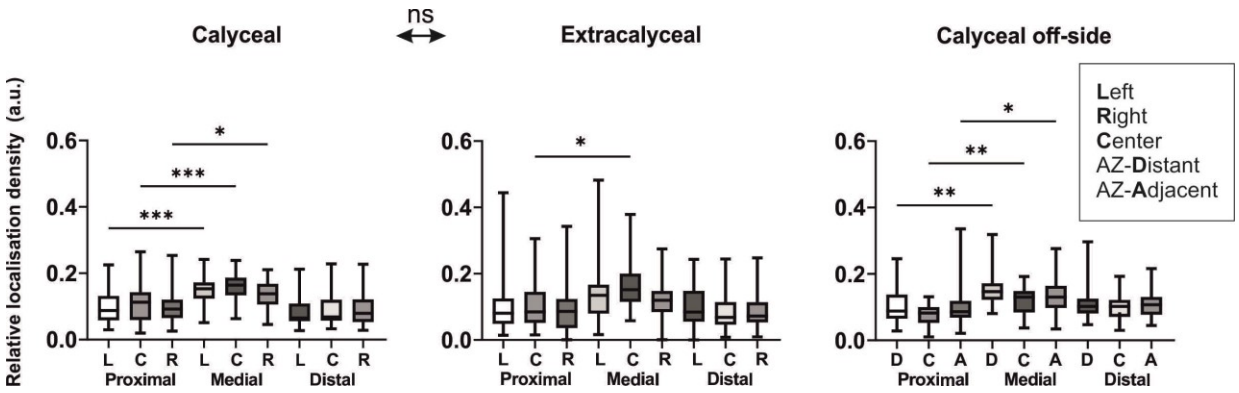

Figure 3.29 SVs are predominantly located 100-200 nm inwards from the AZ. The SV distribution was estimated by averaging the relative localisation density of several SV-associated protein markers. Mean ± StD; for statistics see Table 7.1.

As expected from the SV estimation above, the majority of proteins in calyceal terminals was detected in the medial segment, once again except for SNAP25, which was comparably evenly distributed throughout the terminal. For Rab3a, the left and central side of the proximal segment showed significantly less signal than the medial counterparts. Similarly, VAMP1 was found to be significantly more present in proximal than medial segments. This was not the case for VAMP2. Compared to the estimated SV distribution, Rab3a was significantly reduced in both the central and right side of the proximal segment. The findings for VAMP1 and Rab3a fit well with the results from the reserve pool analysis in the previous section (Figure 3.27). VAMP2 was also significantly reduced in a proximal area, but only on the left side of the segment. SNAP25 showed a significant reduction in the medial centre and both vGluT paralogs exhibited significant reductions in the distal segment; vGluT1 at the left and right, vGluT2 in the centre.

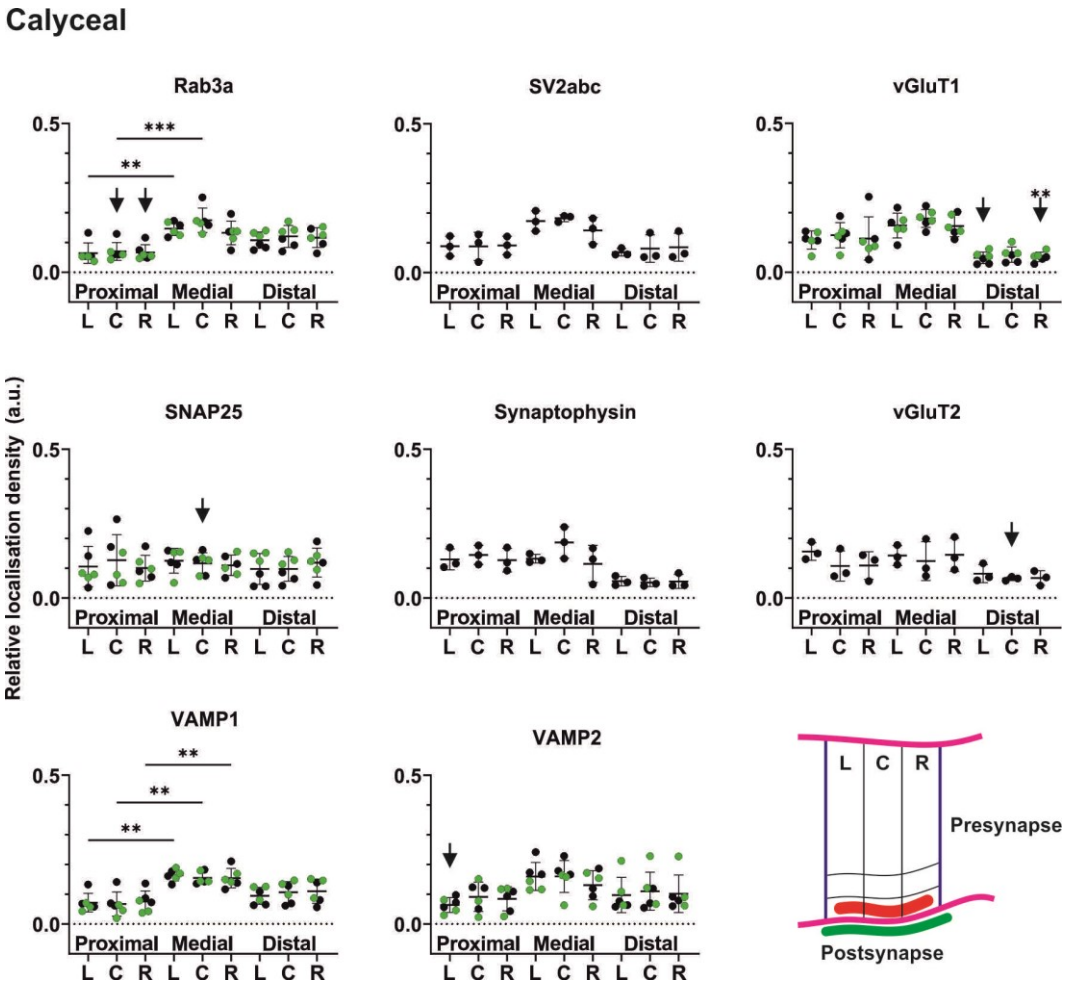

Figure 3.30 Micro-segmentation analysis of calyceal terminals in areas containing an AZ. Lateral SV pool structures were probed by micro-segmentation analysis. The width of the combined lateral segments was matched to the respective AZ dimensions. The proximal and medial segments both reached 100 nm inwards from the AZ border, the distal segment reached towards the distal terminal border. Neighbouring segments were statistically tested using one-way ANOVA, arrows indicate significant deviation from the estimated SV abundance (see Figure 3.29). For orientation see Figure 2.6, legend in Figure 3.29; Data points represent individual animals; Mean ± StD; for statistics see Table 7.1.

Figure 3.31 illustrates the significantly lower presence of vGluT1 in the distal parts of calyceal terminals (also compare distribution in Figure 3.27).

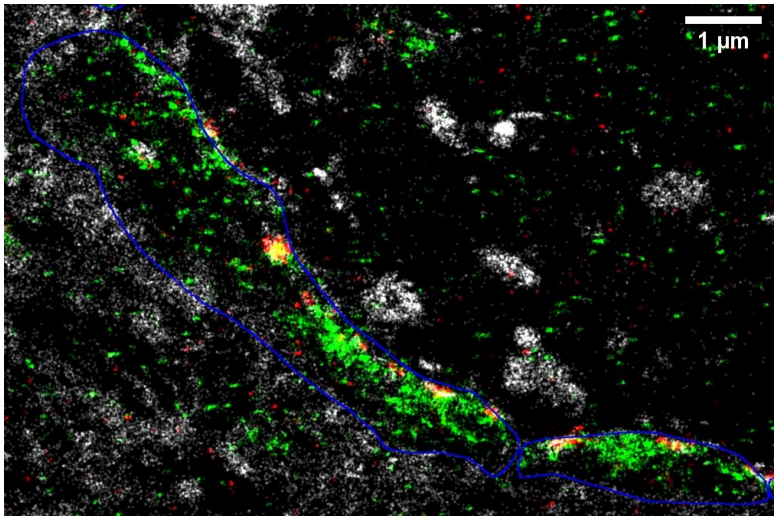

Figure 3.31 Example of vGluT1 protein distribution in calyceal terminals. The merged maS³TORM image of Homer (**red**), vGluT1 (**green**), WGA (**grey**) and the terminal segmentation (**blue**) illustrates the significant reduction of vGluT1 in the distal parts of calyceal terminals.

In areas directly adjoined to an AZ, Rab3a was also found at significantly reduced levels in the proximal segments adjacent and distant to the AZ, when compared with the medial segments (Figure 3.32). Identical findings were obtained for VAMP1, while VAMP2 was significantly reduced in the distant and central parts of the proximal segments. Compared to the estimated SV distribution, the AZ adjacent, proximal segment of Rab3a and VAMP1, the medial centre of SNAP25 as well as the distant side of the distal segment of vGluT1 were significantly reduced. Conversely, the distant side of the medial segment of VAMP1 and the medial centre of VAMP2 contained significantly more IF signal than the SV abundance predicted.

The contrary presence of VAMP1 in the proximal-adjacent and medial-distant segments ties in with the hypothesis of VAMP1 being radially displaced by VAMP2 and therefore potentially governing the slow-releasing SV pool of the calyx[216] (Figure 3.33). However, with the total width of the combined lateral segments of 500 nm, this would imply a potential coupling distance of the assumed VAMP1-dependent SV pool of more than 300 nm to the edge of the Bassoon/Piccolo cluster of the adjacent AZ. It appears unlikely that Ca^{2+} levels would rise sufficiently to trigger SV release at this distance, especially since the calyx is believed to transition from microdomain to nanodomain Ca^{2+} coupling during its maturation[217].

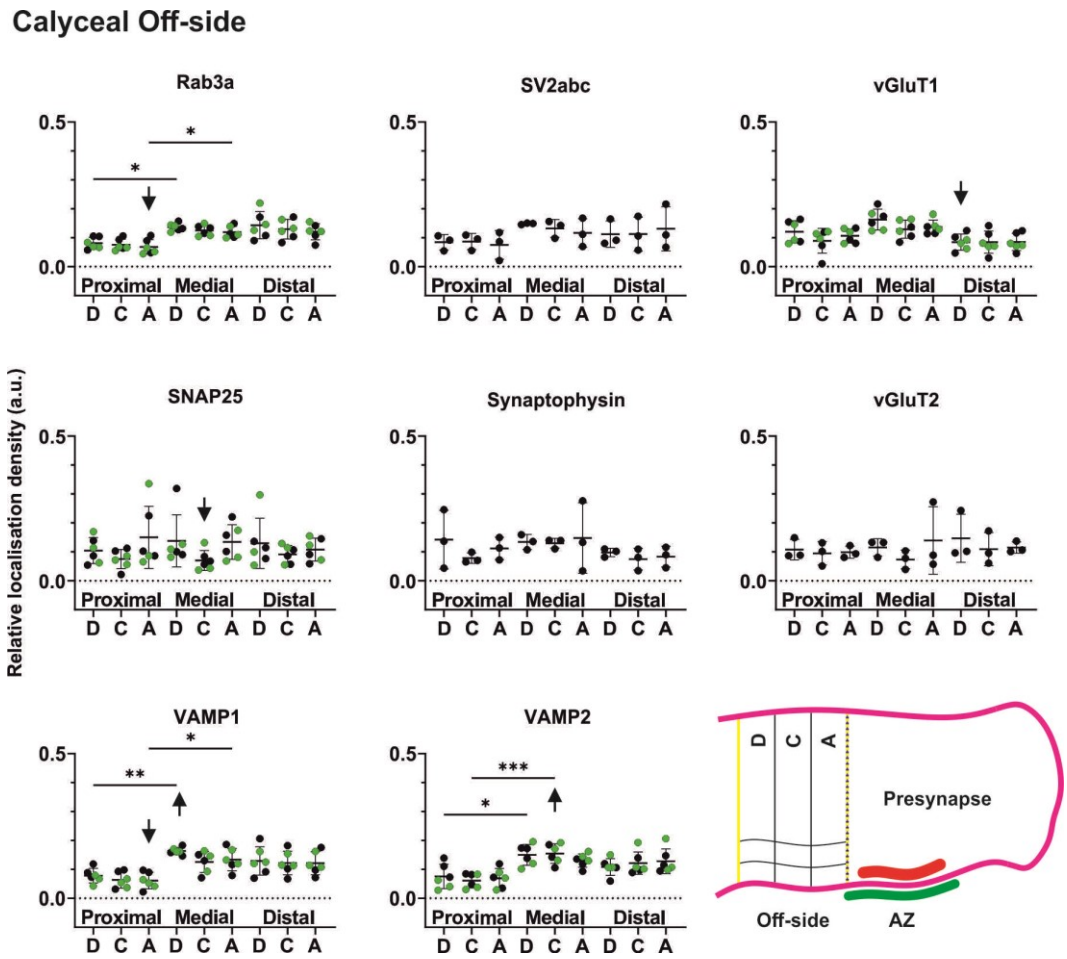

Figure 3.32 Micro-segmentation analysis of calyceal terminals in areas adjacent to an AZ. The micro-segmentation grid was placed immediately adjacent to a respective AZ. Combined width of the lateral segments was 500 nm and the perpendicular dimensions were identical to the AZ grid. Neighbouring segments were statistically tested using one-way ANOVA, arrows indicate significant deviation from the estimated SV abundance (see Figure 3.29). For orientation see Figure 2.6, legend in Figure 3.29; Data points represent individual animals; Mean ± StD; for statistics see Table 7.1.

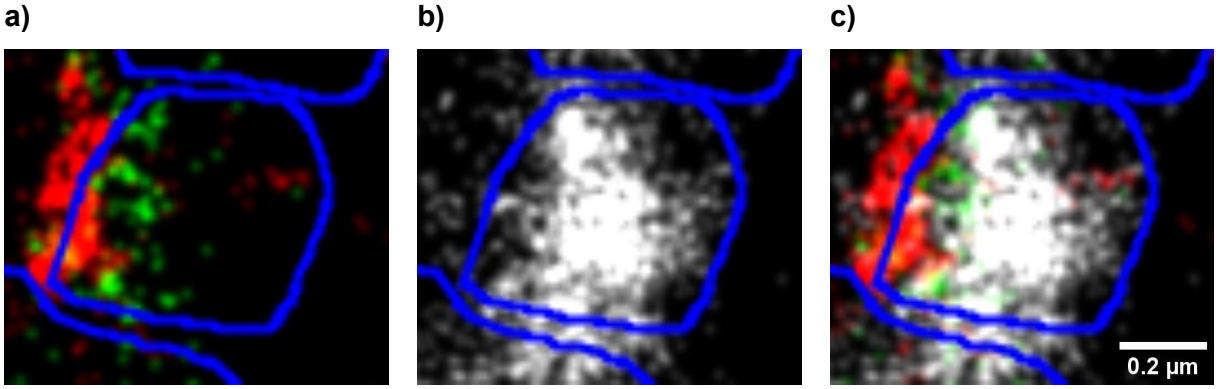

Figure 3.33 Example of reduced presence of VAMP1 in the vicinity of AZs. Merged maS³TORM images of Bassoon/Piccolo (**red**) and Homer (**green**; **a**), VAMP1 (**grey**; **b**) and merged image of **a** and **b** (**c**), encompassed by the terminal segmentation (**blue**).

In extracalyceal terminals, upon visual inspection, Rab3a, VAMP2 and vGluT2 were found at mildly elevated levels in the medial segments and reduced in the proximal segments (Figure 3.34). In comparison, SV2abc and SNAP25 appeared evenly distributed throughout the terminal and Synaptophysin was found insignificantly reduced in the distal segments. Compared to the estimated SV population, Rab3a and SNAP25 were significantly reduced in the medial centre segment. In contrast, VAMP2 was significantly enriched in the medial right segment.

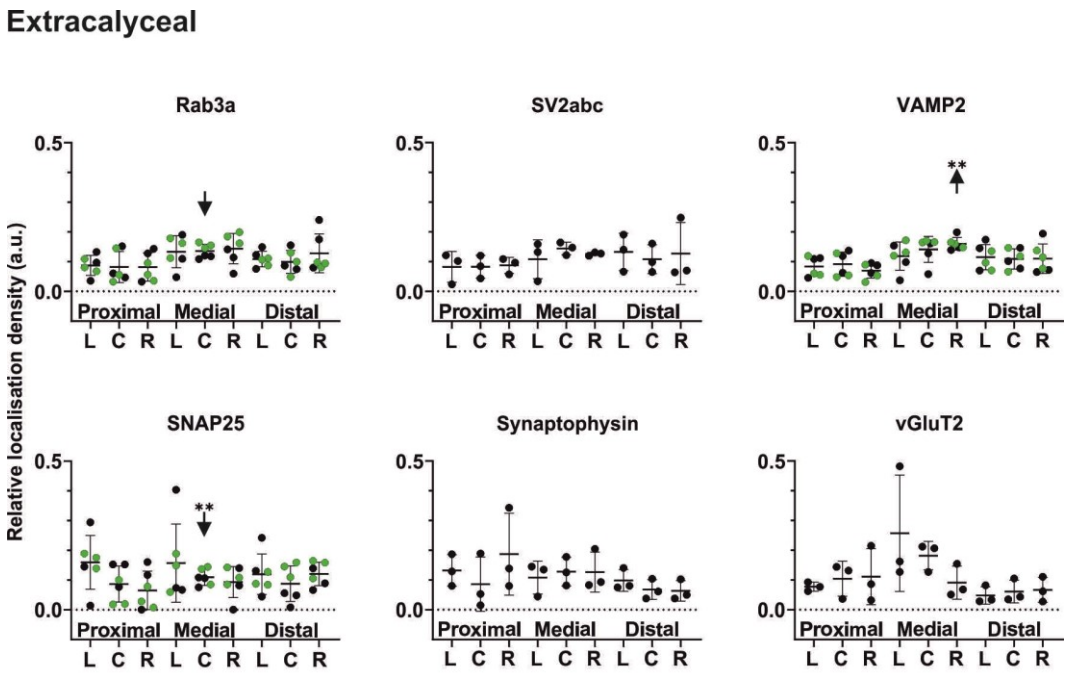

Figure 3.34 Micro-segmentation analysis of extracalyceal terminals in areas containing an AZ. Analysis was performed analogue to the analysis of calyceal terminals. Neighbouring segments were statistically tested using one-way ANOVA, arrows indicate significant deviation from the estimated SV abundance (see Figure 3.29). For orientation see Figure 2.6, legend in Figure 3.29; Data points represent individual animals; Mean ± StD; for statistics see Table 7.1.

While significant differences in the distribution of proteins were obtained for Rab3a, SNAP25 and both VAMP and vGluT paralogs in this section, both compared to the abundance in neighbouring segments and compared to the estimated SV population, lateral differences of the protein distribution were mostly subtle. No significant differences were found between the distribution of VAMP1 and -2 as well as vGluT1 and -2 in calyceal terminal segments, independent of the presence of an AZ. Similarly, a direct comparison of all protein distributions in respective segments between calyceal and extracalyceal terminals did not reveal any significant differences for the VAMP and vGluT paralogs. Nevertheless, four of my findings provide leads for future investigations:

Firstly, the proximally reduced presence of Rab3a, detected both with the micro-segmentation approach and the previous analysis via integrals (Figure 3.27 and Figure 3.28) in areas containing an AZ as well as immediately adjacent to one (Figure 3.32), raises the question whether Rab3a might be involved in structuring a potential reserve pool, which would be located ~100-300 nm (micro-segmentation distance vs. unscaled integral size) inwards from an AZ. As mentioned before, the interaction with Tomosyn has been reported in this context[213]. The inaccessibility of the epitope during SNARE complex formation needs to be considered as well.

Secondly, similar results were obtained for the presence of VAMP1. The striking deviation from the estimated SV population in the proximal and medial segments next to an AZ (Figure 3.32), together with the generally reduced presence in proximity of an AZ, support the idea that VAMP1-containing SVs are located more peripherally of AZs and constitute the slow-releasing SV pool[211]. While the Ca^{2+} coupling distance of ~300 nm appears optimistic, it would explain the reluctant release of this SV pool[216]. Again, restricted access to the epitope during SNARE complex formation needs to be considered. While VAMP2 has been reported to be present on SVs with ~70 copies on average[53], which would make it unlikely that the entire population is inaccessible for pAB binding at any given moment, VAMP1 copy numbers have not been determined, yet.

Third, the reduced presence of vGluT1 at the distal side of calyceal terminals, both in areas in line with an AZ and off-side areas. This strongly indicates a spatially distinct super pool, which vGluT1 has been reported to regulate[208].

And fourth, the more even distribution of SV proteins in extracalyceal terminals. The calyx of Held is known for its particularly large pool of SVs (~70 000[88]-180 000[218]), which might require increased structuring for proper function. The extracalyceal terminals, on the other hand, were found to be significantly smaller (Figure 3.19) and have not been reported to be capable of similarly high firing rates as the calyx. The reduced structure of its SV cluster might therefore indicate a functionally simpler, potentially also less regulated synapse type. The lack of vGluT1 and VAMP1 supports this notion, as the expression of partially redundant paralogs would add regulatory elements to its repertoire.

In summary, the distribution profiles that were analysed in section 3.5 support the idea that additional regulatory elements and off-target interactions of SV proteins (and potentially other classes of presynaptic proteins) structure SV pools. While I found indications for distinct spatial distributions of a subset of SV proteins, the majority of the data suggests that SV clusters are highly heterogeneous. The direct comparison of VAMP1 and -2 as well as vGluT1 and -2 in the

calyx underlines this assumption, since in direct comparison no significant differences were found for their distribution, even though paralogs from both protein families are highly differentially regulated and expressed mutually exclusive in most brain regions[55,219]. It will be interesting to see whether techniques that offer a higher resolution than the maS³TORM approach will find the paralogs to be mutually present on SVs or if they are confined to separate SV pools in the calyx.

Lastly, also the possibility of a probabilistic RP without any molecular marker needs to be considered. Synapsins have been reported to maintain a RP, from which they dissociate under intense stimulation[46,47]. Therefore, SVs that have been released from this RP potentially no longer carry a marker that would allow identity tracking. Instead, passive displacement by other SVs might move a subpopulation of SVs away from the AZ where unspecific binding of synapsins creates a markerless, random reserve pool. While fully hypothetical, this mechanism might represent the closest option to a dedicated SV pool marker without direct involvement in the SV cycle that is currently considered.

4. Conclusions

4.1 Importance of Reliable Fiducial Performance for Multiplexed Microscopy

The image quality of many microscopy techniques benefits from the use of fiducials, however, for SMLM in general and highly multiplexed SRM in particular, a reliable fiducial strategy is quintessential to compensate drift and optical aberrations. Selection of suitable fiducials can be challenging, I therefore compared three popular choices which are NV^--centre ND, TS and GB. I found that ND are spectrally well suited to be used with our maS³TORM microscope. Building on our previous fiducial strategy as reported in Klevanski *et al.*[92], I solved the issue of diametric fiducial brightness requirements during target and fiducial imaging by sequentially acquiring target and fiducial images using different laser lines for excitation. As reported before, fluorescence is recorded from a common colour channel, thus avoiding chromatic aberrations between fiducial and target images. The stable fluorescence of ND allowed continuous recording for one hour and beyond (up to 90 min for presented multiplexed experiments) without deterioration.

In addition, mobility of fiducials can be challenging, especially with imaging modalities that require liquid exchanges, such as exchange-PAINT[135,136] or our maS³TORM approach. I developed an immobilisation approach based on the well-known EDC coupling reaction, which allows cross-linking of carboxylated fiducials to primary amine-containing surface coatings. In contrast to Balinovic *et al.*[165] or others, with my optimised protocol I achieved a monodispersed particle distribution not only with TS, but also using ND and GB. The combination of ND fiducials and EDC immobilisation fully prevented particle loss or relocation from repeated fluid exchange and yielded a superior precision for sequential image registration with uncertainties in the low single-nanometre range.

4.2 Key Characteristics of Calyceal and Extracalyceal Glutamatergic Terminals and How to Tell Them Apart

Synaptic heterogeneity and synaptic plasticity are two of the main factors that shape neuronal networks and allow learning and adaptation. Independent of the synapse type or neurotransmitter composition, all synapses rely on the same basic mechanism: transmitters are stored in SVs,

released into the synaptic cleft from AZs using a complex formed by members of the SNARE family and induce a postsynaptic response by binding to respective receptors. Heterogeneity instead arises from variability in the composition of the SV proteome, the constituents of the release machinery, nanostructural differences and its dynamic regulation through feedback loops or gene expression. Understanding how these regulatory elements connect with each other and shape the observed neuronal response is key to advancing in this medically important field. To achieve this, neurons and their synapses need to be unambiguously identified to avoid averaging features from different neuron or synapse types.

The calyx of Held represents an ideal model synapse for the ultrastructural characterisation of glutamatergic presynapses, as its distinct shape and highly repetitive structure facilitate the identification and orientation of synaptic contacts. However, issues arise from the existence of additional, extracalyceal bouton-type inputs to the MNTB principal cell, of which I found at least one type to be of glutamatergic nature as well. On average, calyceal terminals were significantly larger in size than their extracalyceal counterparts, but at the same time, calyceal terminals exhibited stronger variance in size. Since calyceal AZs closely resemble bouton-type AZs, calyceal swellings could not be distinguished from extracalyceal terminals by morphological features alone. I found two different expression profiles of vGluT1 and -2, as well as VAMP1 and -2 in those smaller terminals, though. One matched the profile of calyceal stalks, in that the terminals expressed both vGluT and VAMP paralogs, while the other terminal subset was characterised by the presence of vGluT2 and VAMP2 alone.

In the first step, I validated the extracalyceal origin of the second terminal type by viral GFP transduction of the contralateral VCN, which therefore labelled calyceal terminals only. Indeed, GFP expression was absent from the second type of terminals, thus confirming that they do not represent precalyceal or otherwise calyx-related projections. In a second step, I developed an approach that allowed identification of the extracalyceal terminal population with ≥85% accuracy without the need for GFP labelling, which uses the ratio of measured VAMP1 and -2 IF in a respective terminal.

Of the glutamatergic terminals surrounding a principal cell, I found over three-quarters to be of calyceal origin. In addition to the aforementioned differences in protein expression levels of vGluT and VAMP paralogs, significantly lower levels of Rab3a IF were found in extracalyceal terminals.

4.3 Updates on SV Pool Organization

To my knowledge, this study represents the most detailed super-resolved description of protein distributions in SV clusters, not only in the calyx of Held but also in mammalian tissue samples in general. I successfully implemented the technical prerequisites for large-scale correlation studies using the maS³TORM approach and established an analysis pipeline to investigate the spatial distribution of SV- and other synaptic proteins in presynaptic terminals.

Using averaged line profiles, I found that SVs accumulated in an area up to ~400-500 nm inwards from an AZ. The strong morphological discrepancy between calyceal and extracalyceal terminals was only mildly reflected by the protein distribution, with extracalyceal terminals exhibiting slightly more even distributions. This is a possible indication of differently organised SV pools in different types of neurons or synapses. I used two separate approaches to assess the protein distribution in orthogonal and lateral direction of an AZ. I found leads towards a distinct distribution of the VAMP paralogs -1 and -2 in close proximity of AZs, but otherwise no significant differences. In addition, I found distinct distributions for the SV proteins SNAP25 and vGluT1, which tie in well with previous reports of SV pool organisation.

The presented results support the notion that SV pools are not structured by a sole dedicated protein but rather by secondary interactions and regulatory elements of proteins involved in the SV cycle or the release machinery that alter SV mobility and availability for exocytosis. Therefore, the added effects of various protein interactions shape the SV pool architecture to the needs of the respective synapse. This also implies that pool boundaries are fluid and depend on the specific context. For example, pools can be shaped through acquired regulatory elements which are present only on a subset of functionally redundant paralogs or isoforms (e.g. vGluT1 and -2 or VAMP1 and -2) and therefore the expression profile would directly influence the SV pool composition.

Ultimately, this study was limited by the lack of single SV resolution, which would be needed to dissect SV subpopulations and detect spatial distribution patterns in heterogeneous SV clouds. Potential avenues are discussed below.

5. Future Perspectives

To address the aforementioned limitations in future endeavours to investigate SV clusters, multiple avenues could be explored. MinFlux or other minimal flux approaches offer unprecedented resolution while keeping the benefit of molecular identification that is inherent to label-based fluorescence microscopy. Using primary labelled antibodies, my group achieved a resolution below 10 nm even in densely populated areas, which would be sufficient to resolve single SVs. The use of DNA-PAINT in minimal flux microscopy has already been demonstrated[220] and, once routinely implemented, will possibly allow multiplexed imaging to a similar degree as our maS³TORM approach. However, in the hands of my group, the combination of 3D localisation and ratiometric dual colour acquisition has proven to be difficult. In addition, acquisition times are drastically longer compared to maS³TORM imaging, even though generally smaller ROIs are imaged with MinFux. To achieve a data set of similar size as it was used for this study, drastic improvements of the technique will be needed.

Provided that suitable pABs or labels against lumenal epitopes of potential SV marker candidates are found, select candidates could be evaluated with higher resolution by adding the label to live neurons in acute brain slices. Amongst others, Truckenbrodt *et al.*[41] demonstrated that these labels would then be internalised under mild to intensive stimulation, depending on the SV pool that is attempted to be targeted. According to SuReSim simulations[221], this would provide a significant boost to the achievable resolution of the maS³TORM microscope without the need to establish new imaging setups or modalities.

The downside of image based analysis approaches, like the ones presented in this study, is, that they omit the axial information which was obtained by maS³TORM imaging. However, algorithms that can handle the amount of localisation data, as it was generated for this study, and which can analyse it in a similar fashion do not exist, yet. With the advent of artificial neuronal networks or artificial intelligence (AI), computer-aided pattern recognition tools are under development which will likely be capable of processing 3D localisation data directly and without constraints to the size of the data sets. AI-driven *a priori* pattern analysis also eliminates the subjective bias that testing of preformed hypotheses creates, but which is unavoidable when data sets of this size are analysed manually.

With a combination of these developments, it will be feasible to image individual SVs and thereby identify the molecular composition on single SV level, which allows to unambiguously assign them to specific SV pools, which will then have to be related to function.

6. Remarks

6.1 References

1. Südhof, T. C. The presynaptic active zone. *Neuron* **75,** 11–25; 10.1016/j.neuron.2012.06.012 (2012).
2. Sheng, M. & Kim, E. The postsynaptic organization of synapses. *Cold Spring Harbor perspectives in biology* **3**; 10.1101/cshperspect.a005678 (2011).
3. Kavalali, E. T. The mechanisms and functions of spontaneous neurotransmitter release. *Nature reviews. Neuroscience* **16,** 5–16; 10.1038/nrn3875 (2015).
4. Andreae, L. C. & Burrone, J. The role of spontaneous neurotransmission in synapse and circuit development. *Journal of Neuroscience Research* **96,** 354–359; 10.1002/jnr.24154 (2018).
5. Bhardwaj, R. D. *et al.* Neocortical neurogenesis in humans is restricted to development. *Proceedings of the National Academy of Sciences of the United States of America* **103,** 12564–12568; 10.1073/pnas.0605177103 (2006).
6. Spalding, K. L. *et al.* Dynamics of hippocampal neurogenesis in adult humans. *Cell* **153,** 1219–1227; 10.1016/j.cell.2013.05.002 (2013).
7. Alvarez-Buylla, A. & Lim, D. A. For the long run: maintaining germinal niches in the adult brain. *Neuron* **41,** 683–686; 10.1016/S0896-6273(04)00111-4 (2004).
8. Nusser, Z. Creating diverse synapses from the same molecules. *Current opinion in neurobiology* **51,** 8–15; 10.1016/j.conb.2018.01.001 (2018).
9. Chua, J. J. E., Kindler, S., Boyken, J. & Jahn, R. The architecture of an excitatory synapse. *Journal of cell science* **123,** 819–823; 10.1242/jcs.052696 (2010).
10. Hughes, B. W., Kusner, L. L. & Kaminski, H. J. Molecular architecture of the neuromuscular junction. *Muscle & nerve* **33,** 445–461; 10.1002/mus.20440 (2006).
11. Südhof, T. C. Towards an Understanding of Synapse Formation. *Neuron* **100,** 276–293; 10.1016/j.neuron.2018.09.040 (2018).
12. Bragina, L. *et al.* Heterogeneity of presynaptic proteins: do not forget isoforms. *Frontiers in cellular neuroscience* **7,** 8; 10.3389/fncel.2013.00008 (2013).
13. Wichmann, C. & Kuner, T. Heterogeneity of glutamatergic synapses: cellular mechanisms and network consequences. *Physiological reviews* **102,** 269–318 (2022).
14. Bury, L. A. D. & Sabo, S. L. How it's made: the synapse. *Molecular interventions* **10,** 282–292; 10.1124/mi.10.5.5 (2010).
15. van den Pol, A. N. Neuropeptide transmission in brain circuits. *Neuron* **76,** 98–115; 10.1016/j.neuron.2012.09.014 (2012).
16. Schoch, S. & Gundelfinger, E. D. Molecular organization of the presynaptic active zone. *Cell and tissue research* **326,** 379–391; 10.1007/s00441-006-0244-y (2006).
17. Tang, A.-H. *et al.* A trans-synaptic nanocolumn aligns neurotransmitter release to receptors. *Nature* **536,** 210–214; 10.1038/nature19058 (2016).
18. Reshetniak, S. & Rizzoli, S. O. The vesicle cluster as a major organizer of synaptic composition in the short-term and long-term. *Current opinion in cell biology* **71,** 63–68; 10.1016/j.ceb.2021.02.007 (2021).
19. Kaeser, P. S. *et al.* RIM proteins tether Ca2+ channels to presynaptic active zones via a direct PDZ-domain interaction. *Cell* **144,** 282–295; 10.1016/j.cell.2010.12.029 (2011).

20. He, R. *et al.* New Insights Into Interactions of Presynaptic Calcium Channel Subtypes and SNARE Proteins in Neurotransmitter Release. *Frontiers in molecular neuroscience* **11,** 213; 10.3389/fnmol.2018.00213 (2018).

21. Jahn, R. & Scheller, R. H. SNAREs--engines for membrane fusion. *Nature reviews. Molecular cell biology* **7,** 631–643; 10.1038/nrm2002 (2006).

22. Jahn, R., Cafiso, D. C. & Tamm, L. K. Mechanisms of SNARE proteins in membrane fusion. *Nature reviews. Molecular cell biology* **25,** 101–118; 10.1038/s41580-023-00668-x (2024).

23. Neher, E. What is Rate-Limiting during Sustained Synaptic Activity: Vesicle Supply or the Availability of Release Sites. *Frontiers in synaptic neuroscience* **2,** 144; 10.3389/fnsyn.2010.00144 (2010).

24. Emperador-Melero, J. & Kaeser, P. S. Assembly of the presynaptic active zone. *Current opinion in neurobiology* **63,** 95–103; 10.1016/j.conb.2020.03.008 (2020).

25. van den Bogaart, G. *et al.* One SNARE complex is sufficient for membrane fusion. *Nature structural & molecular biology* **17,** 358–364; 10.1038/nsmb.1748 (2010).

26. Mohrmann, R., Wit, H. de, Verhage, M., Neher, E. & Sørensen, J. B. Fast vesicle fusion in living cells requires at least three SNARE complexes. *Science (New York, N.Y.)* **330,** 502–505; 10.1126/science.1193134 (2010).

27. Pennuto, M., Bonanomi, D., Benfenati, F. & Valtorta, F. Synaptophysin I controls the targeting of VAMP2/synaptobrevin II to synaptic vesicles. *Molecular biology of the cell* **14,** 4909–4919; 10.1091/mbc.e03-06-0380 (2003).

28. Adams, D. J., Arthur, C. P. & Stowell, M. H. B. Architecture of the Synaptophysin/Synaptobrevin Complex: Structural Evidence for an Entropic Clustering Function at the Synapse. *Scientific reports* **5,** 13659; 10.1038/srep13659 (2015).

29. Bera, M. *et al.* Synaptophysin chaperones the assembly of 12 SNAREpins under each ready-release vesicle. *Proceedings of the National Academy of Sciences of the United States of America* **120,** e2311484120; 10.1073/pnas.2311484120 (2023).

30. Rothman, J. E., Krishnakumar, S. S., Grushin, K. & Pincet, F. Hypothesis - buttressed rings assemble, clamp, and release SNAREpins for synaptic transmission. *FEBS letters* **591,** 3459–3480; 10.1002/1873-3468.12874 (2017).

31. Wen, X., Saltzgaber, G. W. & Thoreson, W. B. Kiss-and-Run Is a Significant Contributor to Synaptic Exocytosis and Endocytosis in Photoreceptors. *Frontiers in cellular neuroscience* **11,** 286; 10.3389/fncel.2017.00286 (2017).

32. Alabi, A. A. & Tsien, R. W. Perspectives on kiss-and-run: role in exocytosis, endocytosis, and neurotransmission. *Annual review of physiology* **75,** 393–422; 10.1146/annurev-physiol-020911-153305 (2013).

33. Chanaday, N. L., Cousin, M. A., Milosevic, I., Watanabe, S. & Morgan, J. R. The Synaptic Vesicle Cycle Revisited: New Insights into the Modes and Mechanisms. *The Journal of neuroscience : the official journal of the Society for Neuroscience* **39,** 8209–8216; 10.1523/JNEUROSCI.1158-19.2019 (2019).

34. Eriksen, J., Li, F. & Edwards, R. H. The mechanism and regulation of vesicular glutamate transport: Coordination with the synaptic vesicle cycle. *Biochimica et biophysica acta. Biomembranes* **1862,** 183259; 10.1016/j.bbamem.2020.183259 (2020).

35. Südhof, T. C. Calcium control of neurotransmitter release. *Cold Spring Harbor perspectives in biology* **4,** a011353; 10.1101/cshperspect.a011353 (2012).

36. Dittman, J. S. & Ryan, T. A. The control of release probability at nerve terminals. *Nature reviews. Neuroscience* **20,** 177–186; 10.1038/s41583-018-0111-3 (2019).

37. Körber, C. & Kuner, T. Molecular Machines Regulating the Release Probability of Synaptic Vesicles at the Active Zone. *Frontiers in synaptic neuroscience* **8,** 5; 10.3389/fnsyn.2016.00005 (2016).

38. Alabi, A. A. & Tsien, R. W. Synaptic vesicle pools and dynamics. *Cold Spring Harbor perspectives in biology* **4,** a013680; 10.1101/cshperspect.a013680 (2012).

39. Denker, A. & Rizzoli, S. O. Synaptic vesicle pools: an update. *Frontiers in synaptic neuroscience* **2,** 135; 10.3389/fnsyn.2010.00135 (2010).

40. Staras, K. *et al.* A vesicle superpool spans multiple presynaptic terminals in hippocampal neurons. *Neuron* **66,** 37–44; 10.1016/j.neuron.2010.03.020 (2010).

41. Truckenbrodt, S. *et al.* Newly produced synaptic vesicle proteins are preferentially used in synaptic transmission. *The EMBO journal* **37**; 10.15252/embj.201798044 (2018).

42. Denker, A., Kröhnert, K. & Rizzoli, S. O. Revisiting synaptic vesicle pool localization in the Drosophila neuromuscular junction. *The Journal of physiology* **587,** 2919–2926; 10.1113/jphysiol.2009.170985 (2009).

43. Crawford, D. C. & Kavalali, E. T. Molecular underpinnings of synaptic vesicle pool heterogeneity. *Traffic (Copenhagen, Denmark)* **16,** 338–364; 10.1111/tra.12262 (2015).

44. Guarnieri, F. C. How Do Synaptic Vesicles "Know" Which Pool They Belong to? *J. Neurosci.* **37,** 2276–2278; 10.1523/JNEUROSCI.3889-16.2017 (2017).

45. Morgan, J. R., Comstra, H. S., Cohen, M. & Faundez, V. Presynaptic membrane retrieval and endosome biology: defining molecularly heterogeneous synaptic vesicles. *Cold Spring Harbor perspectives in biology* **5,** a016915; 10.1101/cshperspect.a016915 (2013).

46. Zhang, M. & Augustine, G. J. Synapsins and the Synaptic Vesicle Reserve Pool: Floats or Anchors? *Cells* **10**; 10.3390/cells10030658 (2021).

47. Vasileva, M., Horstmann, H., Geumann, C., Gitler, D. & Kuner, T. Synapsin-dependent reserve pool of synaptic vesicles supports replenishment of the readily releasable pool under intense synaptic transmission. *The European journal of neuroscience* **36,** 3005–3020; 10.1111/j.1460-9568.2012.08225.x (2012).

48. Orenbuch, A. *et al.* Inhibition of exocytosis or endocytosis blocks activity-dependent redistribution of synapsin. *Journal of neurochemistry* **120,** 248–258; 10.1111/j.1471-4159.2011.07579.x (2012).

49. Wölfel, M., Lou, X. & Schneggenburger, R. A mechanism intrinsic to the vesicle fusion machinery determines fast and slow transmitter release at a large CNS synapse. *J. Neurosci.* **27,** 3198–3210; 10.1523/JNEUROSCI.4471-06.2007 (2007).

50. Sakaba, T. Roles of the fast-releasing and the slowly releasing vesicles in synaptic transmission at the calyx of Held. *J. Neurosci.* **26,** 5863–5871; 10.1523/JNEUROSCI.0182-06.2006 (2006).

51. Guzikowski, N. J. & Kavalali, E. T. Nano-Organization at the Synapse: Segregation of Distinct Forms of Neurotransmission. *Frontiers in synaptic neuroscience* **13,** 796498; 10.3389/fnsyn.2021.796498 (2021).

52. Sudhof, T. C. The synaptic vesicle cycle. *Annual review of neuroscience* **27,** 509–547; 10.1146/annurev.neuro.26.041002.131412 (2004).

53. Takamori, S. *et al.* Molecular anatomy of a trafficking organelle. *Cell* **127,** 831–846; 10.1016/j.cell.2006.10.030 (2006).

54. Zimmermann, J., Trimbuch, T. & Rosenmund, C. Synaptobrevin 1 mediates vesicle priming and evoked release in a subpopulation of hippocampal neurons. *Journal of neurophysiology* **112,** 1559–1565; 10.1152/jn.00340.2014 (2014).

55. Raptis, A., Torrejón-Escribano, B., Gómez de Aranda, I. & Blasi, J. Distribution of synaptobrevin/VAMP 1 and 2 in rat brain. *Journal of chemical neuroanatomy* **30,** 201–211; 10.1016/j.jchemneu.2005.08.002 (2005).

56. Fremeau, R. T. *et al.* The expression of vesicular glutamate transporters defines two classes of excitatory synapse. *Neuron* **31,** 247–260; 10.1016/s0896-6273(01)00344-0 (2001).

57. Weston, M. C., Nehring, R. B., Wojcik, S. M. & Rosenmund, C. Interplay between VGLUT isoforms and endophilin A1 regulates neurotransmitter release and short-term plasticity. *Neuron* **69,** 1147–1159; 10.1016/j.neuron.2011.02.002 (2011).

58. Blaesse, P., Ehrhardt, S., Friauf, E. & Nothwang, H. G. Developmental pattern of three vesicular glutamate transporters in the rat superior olivary complex. *Cell and tissue research* **320,** 33–50; 10.1007/s00441-004-1054-8 (2005).

59. White, D. N. & Stowell, M. H. B. Room for Two: The Synaptophysin/Synaptobrevin Complex. *Frontiers in synaptic neuroscience* **13,** 740318; 10.3389/fnsyn.2021.740318 (2021).

60. Fischer von Mollard, G. *et al.* rab3 is a small GTP-binding protein exclusively localized to synaptic vesicles. *Proceedings of the National Academy of Sciences of the United States of America* **87,** 1988–1992; 10.1073/pnas.87.5.1988 (1990).

61. Schlüter, O. M., Basu, J., Südhof, T. C. & Rosenmund, C. Rab3 superprimes synaptic vesicles for release: implications for short-term synaptic plasticity. *J. Neurosci.* **26,** 1239–1246; 10.1523/JNEUROSCI.3553-05.2006 (2006).

62. Li, T., Cheng, Q., Wang, S. & Ma, C. Rabphilin 3A binds the N-peptide of SNAP-25 to promote SNARE complex assembly in exocytosis. *eLife* **11**; 10.7554/eLife.79926 (2022).

63. Mutch, S. A. *et al.* Protein quantification at the single vesicle level reveals that a subset of synaptic vesicle proteins are trafficked with high precision. *J. Neurosci.* **31,** 1461–1470; 10.1523/JNEUROSCI.3805-10.2011 (2011).

64. Ciruelas, K., Marcotulli, D. & Bajjalieh, S. M. Synaptic vesicle protein 2: A multi-faceted regulator of secretion. *Seminars in cell & developmental biology* **95,** 130–141; 10.1016/j.semcdb.2019.02.003 (2019).

65. Schneggenburger, R. & Forsythe, I. D. The calyx of Held. *Cell and tissue research* **326,** 311–337; 10.1007/s00441-006-0272-7 (2006).

66. Baydyuk, M., Xu, J. & Wu, L.-G. The calyx of Held in the auditory system: Structure, function, and development. *Hearing research* **338,** 22–31; 10.1016/j.heares.2016.03.009 (2016).

67. Cramer, K. S. & Rubel, E. W. Glial Cell Contributions to Auditory Brainstem Development. *Frontiers in neural circuits* **10,** 83; 10.3389/fncir.2016.00083 (2016).

68. Chequer Charan, D. *et al.* Volume electron microscopy reveals age-related circuit remodeling in the auditory brainstem. *Frontiers in cellular neuroscience* **16,** 1070438; 10.3389/fncel.2022.1070438 (2022).

69. Sierksma, M. C., Slotman, J. A., Houtsmuller, A. B. & Borst, J. G. G. Structure-function relation of the developing calyx of Held synapse in vivo. *The Journal of physiology* **598,** 4603–4619; 10.1113/JP279976 (2020).

70. Bergsman, J. B., Camilli, P. de & McCormick, D. A. Multiple large inputs to principal cells in the mouse medial nucleus of the trapezoid body. *Journal of neurophysiology* **92,** 545–552; 10.1152/jn.00927.2003 (2004).

71. Hoffpauir, B. K., Kolson, D. R., Mathers, P. H. & Spirou, G. A. Maturation of synaptic partners: functional phenotype and synaptic organization tuned in synchrony. *The Journal of physiology* **588,** 4365–4385; 10.1113/jphysiol.2010.198564 (2010).

72. Geal-Dor, M., Freeman, S., Li, G. & Sohmer, H. Development of hearing in neonatal rats: air and bone conducted ABR thresholds. *Hearing research* **69,** 236–242; 10.1016/0378-5955(93)90113-f (1993).

73. Ford, M. C., Grothe, B. & Klug, A. Fenestration of the calyx of Held occurs sequentially along the tonotopic axis, is influenced by afferent activity, and facilitates glutamate clearance. *Journal of Comparative Neurology* **514,** 92–106; 10.1002/cne.21998 (2009).

74. Kandler, K. & Friauf, E. Pre- and postnatal development of efferent connections of the cochlear nucleus in the rat. *The Journal of comparative neurology* **328,** 161–184; 10.1002/cne.903280202 (1993).

75. Lenn, N. J. & Reese, T. S. The fine structure of nerve endings in the nucleus of the trapezoid body and the ventral cochlear nucleus. *The American journal of anatomy* **118,** 375–389 (1966).

76. Smith, P. H., Joris, P. X., Carney, L. H. & Yin, T. C. Projections of physiologically characterized globular bushy cell axons from the cochlear nucleus of the cat. *The Journal of comparative neurology* **304,** 387–407; 10.1002/cne.903040305 (1991).

77. Smith, P. H., Joris, P. X. & Yin, T. C. Anatomy and physiology of principal cells of the medial nucleus of the trapezoid body (MNTB) of the cat. *Journal of neurophysiology* **79,** 3127–3142; 10.1152/jn.1998.79.6.3127 (1998).

78. Hoffpauir, B. K., Grimes, J. L., Mathers, P. H. & Spirou, G. A. Synaptogenesis of the calyx of Held: rapid onset of function and one-to-one morphological innervation. *J. Neurosci.* **26,** 5511–5523; 10.1523/JNEUROSCI.5525-05.2006 (2006).

79. Kuwabara, N., DiCaprio, R. A. & Zook, J. M. Afferents to the medial nucleus of the trapezoid body and their collateral projections. *The Journal of comparative neurology* **314,** 684–706; 10.1002/cne.903140405 (1991).

80. Albrecht, O., Dondzillo, A., Mayer, F., Thompson, J. A. & Klug, A. Inhibitory projections from the ventral nucleus of the trapezoid body to the medial nucleus of the trapezoid body in the mouse. *Frontiers in neural circuits* **8,** 83; 10.3389/fncir.2014.00083 (2014).

81. Hamann, M., Billups, B. & Forsythe, I. D. Non-calyceal excitatory inputs mediate low fidelity synaptic transmission in rat auditory brainstem slices. *The European journal of neuroscience* **18,** 2899–2902 (2003).

82. Adams, J. C. & Mugnaini, E. Immunocytochemical evidence for inhibitory and disinhibitory circuits in the superior olive. *Hearing research* **49,** 281–298; 10.1016/0378-5955(90)90109-3 (1990).

83. Borst, J. G., Helmchen, F. & Sakmann, B. Pre- and postsynaptic whole-cell recordings in the medial nucleus of the trapezoid body of the rat. *The Journal of physiology* **489 (Pt 3),** 825–840; 10.1113/jphysiol.1995.sp021095 (1995).

84. Forsythe, I. D. Direct patch recording from identified presynaptic terminals mediating glutamatergic EPSCs in the rat CNS, in vitro. *The Journal of physiology* **479 (Pt 3),** 381–387; 10.1113/jphysiol.1994.sp020303 (1994).

85. Wong, A. Y. C., Graham, B. P., Billups, B. & Forsythe, I. D. Distinguishing between presynaptic and postsynaptic mechanisms of short-term depression during action potential trains. *J. Neurosci.* **23,** 4868–4877; 10.1523/JNEUROSCI.23-12-04868.2003 (2003).

86. Schneggenburger, R. & Neher, E. Intracellular calcium dependence of transmitter release rates at a fast central synapse. *Nature* **406,** 889–893; 10.1038/35022702 (2000).

87. Rowland, K. C., Irby, N. K. & Spirou, G. A. Specialized synapse-associated structures within the calyx of Held. *J. Neurosci.* **20,** 9135–9144; 10.1523/JNEUROSCI.20-24-09135.2000 (2000).

88. Sätzler, K. *et al.* Three-Dimensional Reconstruction of a Calyx of Held and Its Postsynaptic Principal Neuron in the Medial Nucleus of the Trapezoid Body. *J. Neurosci.* **22,** 10567–10579; 10.1523/JNEUROSCI.22-24-10567.2002 (2002).

89. Taschenberger, H., Leão, R. M., Rowland, K. C., Spirou, G. A. & Gersdorff, H. von. Optimizing synaptic architecture and efficiency for high-frequency transmission. *Neuron* **36,** 1127–1143; 10.1016/s0896-6273(02)01137-6 (2002).

90. Lorteije, J. A. M., Rusu, S. I., Kushmerick, C. & Borst, J. G. G. Reliability and precision of the mouse calyx of Held synapse. *J. Neurosci.* **29,** 13770–13784; 10.1523/JNEUROSCI.3285-09.2009 (2009).

91. Taschenberger, H. & Gersdorff, H. von. Fine-tuning an auditory synapse for speed and fidelity: developmental changes in presynaptic waveform, EPSC kinetics, and synaptic plasticity. *J. Neurosci.* **20,** 9162–9173; 10.1523/JNEUROSCI.20-24-09162.2000 (2000).

92. Klevanski, M. *et al.* Automated highly multiplexed super-resolution imaging of protein nano-architecture in cells and tissues. *Nature communications* **11,** 1552; 10.1038/s41467-020-15362-1 (2020).

93. Lichtman, J. W. & Conchello, J.-A. Fluorescence microscopy. *Nature methods* **2,** 910–919; 10.1038/nmeth817 (2005).

94. van de Linde, S. & Sauer, M. How to switch a fluorophore: from undesired blinking to controlled photoswitching. *Chemical Society reviews* **43,** 1076–1087; 10.1039/c3cs60195a (2014).

95. Patterson, G. H. Fluorescence microscopy below the diffraction limit. *Seminars in cell & developmental biology* **20,** 886–893; 10.1016/j.semcdb.2009.08.006 (2009).

96. Blom, H. & Widengren, J. Stimulated Emission Depletion Microscopy. *Chem. Rev.* **117,** 7377–7427; 10.1021/acs.chemrev.6b00653 (2017).

97. Franken, L. E., Grünewald, K., Boekema, E. J. & Stuart, M. C. A. A Technical Introduction to Transmission Electron Microscopy for Soft-Matter: Imaging, Possibilities, Choices, and Technical Developments. *Small (Weinheim an der Bergstrasse, Germany)* **16,** e1906198; 10.1002/smll.201906198 (2020).

98. Gustafsson, M. G. Surpassing the lateral resolution limit by a factor of two using structured illumination microscopy. *Journal of microscopy* **198,** 82–87; 10.1046/j.1365-2818.2000.00710.x (2000).

99. Gustafsson, M. G. L. *et al.* Three-dimensional resolution doubling in wide-field fluorescence microscopy by structured illumination. *Biophysical journal* **94,** 4957–4970; 10.1529/biophysj.107.120345 (2008).

100. Chen, X. *et al.* Superresolution structured illumination microscopy reconstruction algorithms: a review. *Light, science & applications* **12,** 172; 10.1038/s41377-023-01204-4 (2023).

101. Elliott, A. D. Confocal Microscopy: Principles and Modern Practices. *Current protocols in cytometry* **92,** e68; 10.1002/cpcy.68 (2020).

102. Hell, S. W. & Wichmann, J. Breaking the diffraction resolution limit by stimulated emission: stimulated-emission-depletion fluorescence microscopy. *Optics letters* **19,** 780–782; 10.1364/ol.19.000780 (1994).

103. Wegel, E. *et al.* Imaging cellular structures in super-resolution with SIM, STED and Localisation Microscopy: A practical comparison. *Scientific reports* **6,** 27290; 10.1038/srep27290 (2016).

104. Lelek, M. *et al.* Single-molecule localization microscopy. *Nature reviews. Methods primers* **1**; 10.1038/s43586-021-00038-x (2021).

105. Rust, M. J., Bates, M. & Zhuang, X. Sub-diffraction-limit imaging by stochastic optical reconstruction microscopy (STORM). *Nature methods* **3,** 793–795; 10.1038/nmeth929 (2006).

106. Betzig, E. *et al.* Imaging intracellular fluorescent proteins at nanometer resolution. *Science (New York, N.Y.)* **313,** 1642–1645; 10.1126/science.1127344 (2006).

107. Hess, S. T., Girirajan, T. P. K. & Mason, M. D. Ultra-high resolution imaging by fluorescence photoactivation localization microscopy. *Biophysical journal* **91,** 4258–4272; 10.1529/biophysj.106.091116 (2006).

108. Fricke, F., Beaudouin, J., Eils, R. & Heilemann, M. One, two or three? Probing the stoichiometry of membrane proteins by single-molecule localization microscopy. *Scientific reports* **5,** 14072; 10.1038/srep14072 (2015).

109. van de Linde, S. *et al.* Direct stochastic optical reconstruction microscopy with standard fluorescent probes. *Nature protocols* **6,** 991–1009; 10.1038/nprot.2011.336 (2011).

110. Heilemann, M. *et al.* Subdiffraction-resolution fluorescence imaging with conventional fluorescent probes. *Angewandte Chemie (International ed. in English)* **47,** 6172–6176; 10.1002/anie.200802376 (2008).

111. Sharonov, A. & Hochstrasser, R. M. Wide-field subdiffraction imaging by accumulated binding of diffusing probes. *Proceedings of the National Academy of Sciences of the United States of America* **103,** 18911–18916; 10.1073/pnas.0609643104 (2006).

112. Jungmann, R. *et al.* Single-molecule kinetics and super-resolution microscopy by fluorescence imaging of transient binding on DNA origami. *Nano letters* **10,** 4756–4761; 10.1021/nl103427w (2010).

113. Fish, K. N. Total internal reflection fluorescence (TIRF) microscopy. *Current protocols in cytometry* **Chapter 12,** Unit12.18; 10.1002/0471142956.cy1218s50 (2009).

114. Chung, K. K. H. *et al.* Fluorogenic DNA-PAINT for faster, low-background super-resolution imaging. *Nature methods* **19,** 554–559; 10.1038/s41592-022-01464-9 (2022).

115. Kessler, L. F. *et al.* Self-quenched Fluorophore Dimers for DNA-PAINT and STED Microscopy. *Angewandte Chemie (International ed. in English)* **62,** e202307538; 10.1002/anie.202307538 (2023).

116. Narayanasamy, K. K., Rahm, J. V., Tourani, S. & Heilemann, M. Fast DNA-PAINT imaging using a deep neural network. *Nature communications* **13,** 5047; 10.1038/s41467-022-32626-0 (2022).

117. Speiser, A. *et al.* Deep learning enables fast and dense single-molecule localization with high accuracy. *Nature methods* **18,** 1082–1090; 10.1038/s41592-021-01236-x (2021).

118. Schmidt, R. *et al.* MINFLUX nanometer-scale 3D imaging and microsecond-range tracking on a common fluorescence microscope. *Nature communications* **12,** 1478; 10.1038/s41467-021-21652-z (2021).

119. Franke, C., Sauer, M. & van de Linde, S. Photometry unlocks 3D information from 2D localization microscopy data. *Nature methods* **14,** 41–44; 10.1038/nmeth.4073 (2017).

120. Juette, M. F. *et al.* Three-dimensional sub-100 nm resolution fluorescence microscopy of thick samples. *Nature methods* **5,** 527–529; 10.1038/nmeth.1211 (2008).

121. Ram, S., Prabhat, P., Chao, J., Ward, E. S. & Ober, R. J. High accuracy 3D quantum dot tracking with multifocal plane microscopy for the study of fast intracellular dynamics in live cells. *Biophysical journal* **95,** 6025–6043; 10.1529/biophysj.108.140392 (2008).

122. Pavani, S. R. P. *et al.* Three-dimensional, single-molecule fluorescence imaging beyond the diffraction limit by using a double-helix point spread function. *Proceedings of the National Academy of Sciences of the United States of America* **106,** 2995–2999; 10.1073/pnas.0900245106 (2009).

123. Huang, B., Wang, W., Bates, M. & Zhuang, X. Three-dimensional super-resolution imaging by stochastic optical reconstruction microscopy. *Science (New York, N.Y.)* **319,** 810–813; 10.1126/science.1153529 (2008).

124. Mortensen, K. I., Churchman, L. S., Spudich, J. A. & Flyvbjerg, H. Optimized localization analysis for single-molecule tracking and super-resolution microscopy. *Nature methods* **7,** 377–381; 10.1038/nmeth.1447 (2010).

125. C.E. Shannon. Communication in the Presence of Noise. *Proceedings of the IRE* **37,** 10–21 (1949).

126. Shroff, H., Galbraith, C. G., Galbraith, J. A. & Betzig, E. Live-cell photoactivated localization microscopy of nanoscale adhesion dynamics. *Nature methods* **5,** 417–423; 10.1038/nmeth.1202 (2008).

127. Dempsey, G. T., Vaughan, J. C., Chen, K. H., Bates, M. & Zhuang, X. Evaluation of fluorophores for optimal performance in localization-based super-resolution imaging. *Nature methods* **8,** 1027–1036; 10.1038/nmeth.1768 (2011).

128. Sieben, C., Banterle, N., Douglass, K. M., Gönczy, P. & Manley, S. Multicolor single-particle reconstruction of protein complexes. *Nature methods* **15,** 777–780; 10.1038/s41592-018-0140-x (2018).

129. Lampe, A., Haucke, V., Sigrist, S. J., Heilemann, M. & Schmoranzer, J. Multi-colour direct STORM with red emitting carbocyanines. *Biology of the cell* **104,** 229–237; 10.1111/boc.201100011 (2012).

130. Bossi, M. *et al.* Multicolor far-field fluorescence nanoscopy through isolated detection of distinct molecular species. *Nano letters* **8,** 2463–2468; 10.1021/nl801471d (2008).

131. Gimber, N., Strauss, S., Jungmann, R. & Schmoranzer, J. Simultaneous Multicolor DNA-PAINT without Sequential Fluid Exchange Using Spectral Demixing. *Nano letters* **22,** 2682–2690; 10.1021/acs.nanolett.1c04520 (2022).

132. Erdelyi, M. *et al.* Correcting chromatic offset in multicolor super-resolution localization microscopy. *Optics express* **21,** 10978–10988; 10.1364/OE.21.010978 (2013).

133. Lampe, A., Tadeus, G. & Schmoranzer, J. Spectral demixing avoids registration errors and reduces noise in multicolor localization-based super-resolution microscopy. *Methods and applications in fluorescence* **3,** 34006 (2015).

134. Yi, J. *et al.* madSTORM: a superresolution technique for large-scale multiplexing at single-molecule accuracy. *Molecular biology of the cell* **27,** 3591–3600; 10.1091/mbc.E16-05-0330 (2016).

135. Jungmann, R. *et al.* Multiplexed 3D cellular super-resolution imaging with DNA-PAINT and Exchange-PAINT. *Nature methods* **11,** 313–318; 10.1038/nmeth.2835 (2014).

136. Narayanasamy, K. K. *et al.* Visualizing Synaptic Multi-Protein Patterns of Neuronal Tissue With DNA-Assisted Single-Molecule Localization Microscopy. *Frontiers in synaptic neuroscience* **13,** 671288; 10.3389/fnsyn.2021.671288 (2021).

137. Tam, J., Cordier, G. A., Borbely, J. S., Sandoval Álvarez, A. & Lakadamyali, M. Cross-talk-free multi-color STORM imaging using a single fluorophore. *PloS one* **9,** e101772; 10.1371/journal.pone.0101772 (2014).

138. Valley, C. C., Liu, S., Lidke, D. S. & Lidke, K. A. Sequential superresolution imaging of multiple targets using a single fluorophore. *PloS one* **10,** e0123941; 10.1371/journal.pone.0123941 (2015).

139. Strauss, S. *et al.* Modified aptamers enable quantitative sub-10-nm cellular DNA-PAINT imaging. *Nature methods* **15,** 685–688; 10.1038/s41592-018-0105-0 (2018).

140. Tan, Y. H. *et al.* A nanoengineering approach for investigation and regulation of protein immobilization. *ACS nano* **2,** 2374–2384; 10.1021/nn800508f (2008).

141. Los, G. V. *et al.* HaloTag: a novel protein labeling technology for cell imaging and protein analysis. *ACS chemical biology* **3,** 373–382; 10.1021/cb800025k (2008).

142. Keppler, A. *et al.* A general method for the covalent labeling of fusion proteins with small molecules in vivo. *Nature biotechnology* **21,** 86–89; 10.1038/nbt765 (2003).

143. Adams, A. E. & Pringle, J. R. Staining of actin with fluorochrome-conjugated phalloidin. *Methods in enzymology* **194,** 729–731; 10.1016/0076-6879(91)94054-g (1991).

144. Nagata, Y. & Burger, M. M. Wheat germ agglutinin. Molecular characteristics and specificity for sugar binding. *The Journal of biological chemistry* **249,** 3116–3122 (1974).

145. Traenkle, B. & Rothbauer, U. Under the Microscope: Single-Domain Antibodies for Live-Cell Imaging and Super-Resolution Microscopy. *Frontiers in immunology* **8,** 1030; 10.3389/fimmu.2017.01030 (2017).

146. Erickson, H. P. Size and shape of protein molecules at the nanometer level determined by sedimentation, gel filtration, and electron microscopy. *Biological procedures online* **11,** 32–51; 10.1007/s12575-009-9008-x (2009).

147. Li, S. & Sheng, Z.-H. Energy matters: presynaptic metabolism and the maintenance of synaptic transmission. *Nature reviews. Neuroscience* **23,** 4–22; 10.1038/s41583-021-00535-8 (2022).

148. Pulido, C. & Ryan, T. A. Synaptic vesicle pools are a major hidden resting metabolic burden of nerve terminals. *Science advances* **7,** eabi9027; 10.1126/sciadv.abi9027 (2021).

149. Merck Millipore. Application Note: Microsphere Coupling https://www.merckmillipore.com/Web-INTL-Site/en_US/-/USD/ShowDocument-Pronet?id=201507.097 - 20.07.2024, 23:05.

150. Wen, H. *et al.* Correlative Fluorescence and Transmission Electron Microscopy Assisted by 3D Machine Learning Reveals Thin Nanodiamonds Fluoresce Brighter. *ACS nano* **17,** 16491–16500; 10.1021/acsnano.3c00857 (2023).

151. Schindelin, J. *et al.* Fiji: an open-source platform for biological-image analysis. *Nature methods* **9,** 676–682; 10.1038/nmeth.2019 (2012).

152. Herrmannsdörfer, F. *et al.* 3D d STORM Imaging of Fixed Brain Tissue. *Methods in molecular biology (Clifton, N.J.)* **1538,** 169–184; 10.1007/978-1-4939-6688-2_13 (2017).

153. Körber, C. *et al.* Modulation of Presynaptic Release Probability by the Vertebrate-Specific Protein Mover. *Neuron* **87,** 521–533; 10.1016/j.neuron.2015.07.001 (2015).

154. Tokuyasu, K. T. A technique for ultracryotomy of cell suspensions and tissues. *The Journal of cell biology* **57,** 551–565; 10.1083/jcb.57.2.551 (1973).

155. Tokuyasu, K. T., Dutton, A. H. & Singer, S. J. Immunoelectron microscopic studies of desmin (skeletin) localization and intermediate filament organization in chicken cardiac muscle. *The Journal of cell biology* **96,** 1736–1742; 10.1083/jcb.96.6.1736 (1983).

156. Wimmer, V. C., Nevian, T. & Kuner, T. Targeted in vivo expression of proteins in the calyx of Held. *Pflugers Archiv : European journal of physiology* **449,** 319–333; 10.1007/s00424-004-1327-9 (2004).

157. Herrmannsdörfer, F. *Exploring the limits of single molecule localization microscopy using realistic simulations with a focus on presynaptic nerve terminals* (Heidelberg, 2017).

158. Edelstein, A., Amodaj, N., Hoover, K., Vale, R. & Stuurman, N. Computer control of microscopes using μManager. *Current protocols in molecular biology* **Chapter 14,** Unit14.20; 10.1002/0471142727.mb1420s92 (2010).

159. Wolter, S. *et al.* rapidSTORM: accurate, fast open-source software for localization microscopy. *Nature methods* **9,** 1040–1041; 10.1038/nmeth.2224 (2012).

160. Descloux, A., Grußmayer, K. S. & Radenovic, A. Parameter-free image resolution estimation based on decorrelation analysis. *Nature methods* **16,** 918–924; 10.1038/s41592-019-0515-7 (2019).

161. Levet, F. *et al.* A tessellation-based colocalization analysis approach for single-molecule localization microscopy. *Nature communications* **10,** 2379; 10.1038/s41467-019-10007-4 (2019).

162. Bates, M., Dempsey, G. T., Chen, K. H. & Zhuang, X. Multicolor super-resolution fluorescence imaging via multi-parameter fluorophore detection. *Chemphyschem : a European journal of chemical physics and physical chemistry* **13,** 99–107; 10.1002/cphc.201100735 (2012).

163. Linsley, J. W. *et al.* Automated four-dimensional long term imaging enables single cell tracking within organotypic brain slices to study neurodevelopment and degeneration. *Communications biology* **2,** 155; 10.1038/s42003-019-0411-9 (2019).

164. Colomb, W., Czerski, J., Sau, J. D. & Sarkar, S. K. Estimation of microscope drift using fluorescent nanodiamonds as fiducial markers. *Journal of microscopy* **266,** 298–306 (2017).

165. Balinovic, A., Albrecht, D. & Endesfelder, U. Spectrally red-shifted fluorescent fiducial markers for optimal drift correction in localization microscopy. *J. Phys. D: Appl. Phys.* **52,** 204002; 10.1088/1361-6463/ab0862 (2019).

166. Fan, X. *et al.* Three dimensional drift control at nano-scale in single molecule localization microscopy. *Optics express* **28,** 32750–32763; 10.1364/OE.404123 (2020).

167. Jain, P. K., Lee, K. S., El-Sayed, I. H. & El-Sayed, M. A. Calculated absorption and scattering properties of gold nanoparticles of different size, shape, and composition: applications in biological imaging and biomedicine. *The journal of physical chemistry. B* **110,** 7238–7248; 10.1021/jp057170o (2006).

168. He, H., Xie, C. & Ren, J. Nonbleaching fluorescence of gold nanoparticles and its applications in cancer cell imaging. *Analytical Chemistry* **80,** 5951–5957; 10.1021/ac8005796 (2008).

169. Li, T. *et al.* Revealing the Mechanism of Photoluminescence from Single Gold Nanospheres by Defocused Imaging. *ACS Photonics* **4,** 2003–2010; 10.1021/acsphotonics.7b00376 (2017).

170. Alkahtani, M. H. *et al.* Fluorescent nanodiamonds: past, present, and future. *Nanophotonics* **7,** 1423–1453; 10.1515/nanoph-2018-0025 (2018).

171. Nakajima, N. & Ikada, Y. Mechanism of amide formation by carbodiimide for bioconjugation in aqueous media. *Bioconjugate chemistry* **6,** 123–130; 10.1021/bc00031a015 (1995).

172. Costello, I. & Cox, S. Analysing errors in single-molecule localisation microscopy. *The international journal of biochemistry & cell biology* **134,** 105931; 10.1016/j.biocel.2021.105931 (2021).

173. Qu, L., Akbergenova, Y., Hu, Y. & Schikorski, T. Synapse-to-synapse variation in mean synaptic vesicle size and its relationship with synaptic morphology and function. *The Journal of comparative neurology* **514,** 343–352; 10.1002/cne.22007 (2009).

174. Milinkeviciute, G. *et al.* Microglia Regulate Pruning of Specialized Synapses in the Auditory Brainstem. *Frontiers in neural circuits* **13,** 55; 10.3389/fncir.2019.00055 (2019).

175. Nakamura, P. A. & Cramer, K. S. Formation and maturation of the calyx of Held. *Hearing research* **276,** 70–78; 10.1016/j.heares.2010.11.004 (2011).

176. Mendoza Schulz, A. The role of the presynaptic scaffold protein Bassoon in synaptic transmission at the mouse endbulb of Held synapse. University Goettingen Repository.

177. Banks, M. I. & Smith, P. H. Intracellular recordings from neurobiotin-labeled cells in brain slices of the rat medial nucleus of the trapezoid body. *J. Neurosci.* **12,** 2819–2837; 10.1523/JNEUROSCI.12-07-02819.1992 (1992).

178. Wenthold, R. J., Huie, D., Altschuler, R. A. & Reeks, K. A. Glycine immunoreactivity localized in the cochlear nucleus and superior olivary complex. *Neuroscience* **22,** 897–912; 10.1016/0306-4522(87)92968-x (1987).

179. Dondzillo, A. *et al.* Targeted three-dimensional immunohistochemistry reveals localization of presynaptic proteins Bassoon and Piccolo in the rat calyx of Held before and after the onset of hearing. *Journal of Comparative Neurology* **518,** 1008–1029; 10.1002/cne.22260 (2010).

180. Schneggenburger, R., Meyer, A. C. & Neher, E. Released fraction and total size of a pool of immediately available transmitter quanta at a calyx synapse. *Neuron* **23,** 399–409; 10.1016/s0896-6273(00)80789-8 (1999).

181. Spirou, G. A., Chirila, F. V., Gersdorff, H. von & Manis, P. B. Heterogeneous Ca2+ influx along the adult calyx of Held: a structural and computational study. *Neuroscience* **154,** 171–185; 10.1016/j.neuroscience.2008.04.002 (2008).

182. Iwasaki, S. & Takahashi, T. Developmental regulation of transmitter release at the calyx of Held in rat auditory brainstem. *The Journal of physiology* **534,** 861–871; 10.1111/j.1469-7793.2001.00861.x (2001).

183. Crins, T. T. H., Rusu, S. I., Rodríguez-Contreras, A. & Borst, J. G. G. Developmental changes in short-term plasticity at the rat calyx of Held synapse. *J. Neurosci.* **31,** 11706–11717; 10.1523/JNEUROSCI.1995-11.2011 (2011).

184. Mikaelian, D. & Ruben, R. J. Development of Hearing in the Normal Cba-J Mouse: Correlation of Physiological Observations with Behavioral Responses and with Cochlear Anatomy. *Acta Oto-Laryngologica* **59,** 451–461; 10.3109/00016486509124579 (1965).

185. Miyazaki, T., Fukaya, M., Shimizu, H. & Watanabe, M. Subtype switching of vesicular glutamate transporters at parallel fibre-Purkinje cell synapses in developing mouse cerebellum. *The European journal of neuroscience* **17,** 2563–2572; 10.1046/j.1460-9568.2003.02698.x (2003).

186. Schlüter, O. M., Schmitz, F., Jahn, R., Rosenmund, C. & Südhof, T. C. A complete genetic analysis of neuronal Rab3 function. *J. Neurosci.* **24,** 6629–6637; 10.1523/JNEUROSCI.1610-04.2004 (2004).

187. Manders, E. M. M., Verbeek, F. J. & Aten, J. A. Measurement of co-localization of objects in dual-colour confocal images. *Journal of microscopy* **169,** 375–382; 10.1111/j.1365-2818.1993.tb03313.x (1993).

188. Willems, J. & MacGillavry, H. D. A coordinate-based co-localization index to quantify and visualize spatial associations in single-molecule localization microscopy. *Scientific reports* **12,** 4676; 10.1038/s41598-022-08746-4 (2022).

189. Ejdrup, A. L. *et al.* A density-based enrichment measure for assessing colocalization in single-molecule localization microscopy data. *Nature communications* **13,** 4388; 10.1038/s41467-022-32064-y (2022).

190. Levet, F. *et al.* SR-Tesseler: a method to segment and quantify localization-based super-resolution microscopy data. *Nature methods* **12,** 1065–1071; 10.1038/nmeth.3579 (2015).

191. Root, D. H. *et al.* Selective Brain Distribution and Distinctive Synaptic Architecture of Dual Glutamatergic-GABAergic Neurons. *Cell reports* **23,** 3465–3479; 10.1016/j.celrep.2018.05.063 (2018).

192. Root, D. H. *et al.* Single rodent mesohabenular axons release glutamate and GABA. *Nature neuroscience* **17,** 1543–1551; 10.1038/nn.3823 (2014).

193. Liu, W. W. & Wilson, R. I. Glutamate is an inhibitory neurotransmitter in the Drosophila olfactory system. *Proceedings of the National Academy of Sciences of the United States of America* **110,** 10294–10299; 10.1073/pnas.1220560110 (2013).

194. Isaacson, J. S. & Murphy, G. J. Glutamate-mediated extrasynaptic inhibition: direct coupling of NMDA receptors to Ca(2+)-activated K+ channels. *Neuron* **31,** 1027–1034; 10.1016/s0896-6273(01)00428-7 (2001).

195. Hubrecht, R. C. & Carter, E. The 3Rs and Humane Experimental Technique: Implementing Change. *Animals : an Open Access Journal from MDPI* **9**; 10.3390/ani9100754 (2019).

196. Meyer, A. C., Neher, E. & Schneggenburger, R. Estimation of quantal size and number of functional active zones at the calyx of Held synapse by nonstationary EPSC variance analysis. *J. Neurosci.* **21,** 7889–7900; 10.1523/JNEUROSCI.21-20-07889.2001 (2001).

197. Regehr, W. G. Short-term presynaptic plasticity. *Cold Spring Harbor perspectives in biology* **4,** a005702; 10.1101/cshperspect.a005702 (2012).

198. Giovedì, S., Darchen, F., Valtorta, F., Greengard, P. & Benfenati, F. Synapsin is a novel Rab3 effector protein on small synaptic vesicles. II. Functional effects of the Rab3A-synapsin I interaction. *The Journal of biological chemistry* **279,** 43769–43779; 10.1074/jbc.M404168200 (2004).

199. Bae, J. R. *et al.* Distinct synaptic vesicle recycling in inhibitory nerve terminals is coordinated by SV2A. *Progress in neurobiology* **194,** 101879; 10.1016/j.pneurobio.2020.101879 (2020).

200. Glebov, O. O., Cox, S., Humphreys, L. & Burrone, J. Neuronal activity controls transsynaptic geometry. *Scientific reports* **6,** 22703; 10.1038/srep22703 (2016).

201. Dani, A., Huang, B., Bergan, J., Dulac, C. & Zhuang, X. Superresolution imaging of chemical synapses in the brain. *Neuron* **68,** 843–856; 10.1016/j.neuron.2010.11.021 (2010).

202. Qiu, X., Zhu, Q. & Sun, J. Quantitative analysis of vesicle recycling at the calyx of Held synapse. *Proceedings of the National Academy of Sciences of the United States of America* **112,** 4779–4784; 10.1073/pnas.1424597112 (2015).

203. Fischer von Mollard, G., Stahl, B., Li, C., Südhof, T. C. & Jahn, R. Rab proteins in regulated exocytosis. *Trends in biochemical sciences* **19,** 164–168; 10.1016/0968-0004(94)90278-X (1994).

204. Gordon, S. L., Leube, R. E. & Cousin, M. A. Synaptophysin is required for synaptobrevin retrieval during synaptic vesicle endocytosis. *J. Neurosci.* **31,** 14032–14036; 10.1523/JNEUROSCI.3162-11.2011 (2011).

205. Schivell, A. E., Mochida, S., Kensel-Hammes, P., Custer, K. L. & Bajjalieh, S. M. SV2A and SV2C contain a unique synaptotagmin-binding site. *Molecular and cellular neurosciences* **29,** 56–64; 10.1016/j.mcn.2004.12.011 (2005).

206. Ogunmowo, T. *et al.* Intersectin and Endophilin condensates prime synaptic vesicles for release site replenishment. *bioRxiv : the preprint server for biology*; 10.1101/2023.08.22.554276 (2023).

207. Gowrisankaran, S. *et al.* Endophilin-A coordinates priming and fusion of neurosecretory vesicles via intersectin. *Nature communications* **11,** 1266; 10.1038/s41467-020-14993-8 (2020).

208. Zhang, X. M. *et al.* A proline-rich motif on VGLUT1 reduces synaptic vesicle super-pool and spontaneous release frequency. *eLife* **8**; 10.7554/eLife.50401 (2019).

209. Pan, P.-Y., Marrs, J. & Ryan, T. A. Vesicular glutamate transporter 1 orchestrates recruitment of other synaptic vesicle cargo proteins during synaptic vesicle recycling. *The Journal of biological chemistry* **290,** 22593–22601; 10.1074/jbc.M115.651711 (2015).

210. Li, H., Santos, M. S., Park, C. K., Dobry, Y. & Voglmaier, S. M. VGLUT2 Trafficking Is Differentially Regulated by Adaptor Proteins AP-1 and AP-3. *Frontiers in cellular neuroscience* **11,** 324; 10.3389/fncel.2017.00324 (2017).

211. Sakaba, T. & Neher, E. Calmodulin mediates rapid recruitment of fast-releasing synaptic vesicles at a calyx-type synapse. *Neuron* **32,** 1119–1131; 10.1016/s0896-6273(01)00543-8 (2001).

212. Cheung, G., Jupp, O. J. & Cousin, M. A. Activity-dependent bulk endocytosis and clathrin-dependent endocytosis replenish specific synaptic vesicle pools in central nerve terminals. *J. Neurosci.* **30,** 8151–8161; 10.1523/JNEUROSCI.0293-10.2010 (2010).

213. Cazares, V. A. *et al.* Dynamic Partitioning of Synaptic Vesicle Pools by the SNARE-Binding Protein Tomosyn. *J. Neurosci.* **36,** 11208–11222; 10.1523/JNEUROSCI.1297-16.2016 (2016).

214. Horstmann, H., Körber, C., Sätzler, K., Aydin, D. & Kuner, T. Serial section scanning electron microscopy (S3EM) on silicon wafers for ultra-structural volume imaging of cells and tissues. *PloS one* **7,** e35172; 10.1371/journal.pone.0035172 (2012).

215. Denker, A., Kröhnert, K., Bückers, J., Neher, E. & Rizzoli, S. O. The reserve pool of synaptic vesicles acts as a buffer for proteins involved in synaptic vesicle recycling. *Proceedings of the National Academy of Sciences of the United States of America* **108,** 17183–17188; 10.1073/pnas.1112690108 (2011).

216. Wadel, K., Neher, E. & Sakaba, T. The coupling between synaptic vesicles and Ca2+ channels determines fast neurotransmitter release. *Neuron* **53,** 563–575; 10.1016/j.neuron.2007.01.021 (2007).

217. Wang, L.-Y. & Augustine, G. J. Presynaptic nanodomains: a tale of two synapses. *Frontiers in cellular neuroscience* **8,** 455; 10.3389/fncel.2014.00455 (2014).

218. Lange, R. P. J. de, Roos, A. D. G. de & Borst, J. G. G. Two modes of vesicle recycling in the rat calyx of Held. *J. Neurosci.* **23,** 10164–10173; 10.1523/JNEUROSCI.23-31-10164.2003 (2003).

219. Nakakubo, Y. *et al.* Vesicular Glutamate Transporter Expression Ensures High-Fidelity Synaptic Transmission at the Calyx of Held Synapses. *Cell reports* **32,** 108040; 10.1016/j.celrep.2020.108040 (2020).

220. Ostersehlt, L. M. *et al.* DNA-PAINT MINFLUX nanoscopy. *Nature methods* **19,** 1072–1075; 10.1038/s41592-022-01577-1 (2022).

221. Venkataramani, V., Herrmannsdörfer, F., Heilemann, M. & Kuner, T. SuReSim: simulating localization microscopy experiments from ground truth models. *Nature methods* **13,** 319–321; 10.1038/nmeth.3775 (2016).

6.2 Acknowledgements and Contributions

I would like to thank the people that were involved during the course of this thesis and contributed to its successful completion:

Prof. Dr. Thomas Kuner, thank you for the opportunity to pursue my doctoral degree under your supervision, your scientific inputs and organisational guidance.

Prof. Dr. Christoph Schuster, I appreciate your involvement as a member of my Thesis Advisory Committee and as my second reviewer.

Prof. Dr. Mike Heilemann, thank you for our insightful discussions and for your involvement as external member of my Thesis Advisory Committee.

Prof. Dr. Gáspàr Jékely and Prof. Dr. Andres Jäschke for your time and efforts as members of my disputation committee.

Dr. Maja Klevanski, my deepest appreciation for our sometimes intense, but always fruitful discussions, your leadership, supply of tissue sections and code contributions.

Dr. Kaarjel Narayanasamy, Dr. Aleksandar Stojic and Marina Hesse for your everlasting comradeship as well as constant supply of tissue sections.

Franziska Gleiche, Simone Hoppe, Michaela Kaiser and Claudia Kocksch for your patience and support as well as Marion Schmitt for the stereotactic injections.

Dr. Jörg Malsam for your support in acquiring the GB absorbance spectrum.

Dr. Franziska Grün for your support in acquiring the GB emission spectra.

Dr. Carlo Beretta and Dr. Frank Herrmannsdoerfer for your technical assistance and coding lessons.

What is life without family and friends, without whose undying support I would not be writing this paragraph today:

My parents Wiebke and Wolfgang, words cannot describe the gratitude that I feel for your never-ending support and heartfelt advice.

My partner Dr. Megan Palmer for your patience and advice, the occasional kick in my backside, for climbing every mountain with me and catching me whenever I fall.

Dr. Patrick Eiring, Dr. Ralph Götz and Dr. Philipp Kreisz, thank you for keeping my hopes up and my expectations down during all these years.

And a big thank you to everyone else who has a space in my life, but unfortunately not on this page!

7. Appendix

Appendix 1 Experiment Information and Statistics

Table 7.1 Experiment information and statistics

Sample ID	Animal ID	Age	Multiplexing protocol	n ROIs	n Segmentations		n Line Profiles				n Micro-Segmentations		
					Calyx	Extrac.	AZ Calyx	AZ Extrac.	Off. Calyx	Off. Extrac.	AZ Calyx	AZ Extrac.	Off. Calyx
µ131	r61	12	LM(a)	12	331	83	68	19	54	12	23	22	34
µ150	r60	12	LM(b)	10	120	36	32	8	23	10	12	6	14
A188	r64	13	LM(b)	8	172	45	10	9	25	4	8	5	13
µ211	r85	21	P21	8	169	88							
µ221	r86	21	P21	7	83	46							
µ189	r79	21	P21	9	132	44							
µ265	r95	13	GFP	10	353	109	54	15	40	16	15	7	17
µ280	r101	13	GFP	8	195	70	25	10	21	9	13	10	20
µ272	r100	13	GFP	10	230	82	37	12	35	13	21	6	28

Appendix 2 Multiplexed Experiments

Table 7.2 Large Multiplexed (LM) Experiment

SR	Treatment	Reagents		Parameters	Duration
1	pAB staining	WGA-AF488 (1:1000), vGluT1-gp (1:500), Piccolo-rb (1:200), Bassoon-ms(k) (1:500)		in 0.5% FCS in PBS	45 min
	sAB staining	gp-AF647, rb-CF680, ms-CF680, ms(k)-CF680 (1:500, each)		in 0.5% FCS in PBS	45 min
	Imaging	100 mM MEA, pH 8		20k frames, 30 ms, 2.7 kW/cm²	15 min/ROI
	Label removal	Elution: 0.1% SDS in PBS (pH 13), Bleaching: PBS		661 nm (2.7 kW/cm²) + 405 nm (1 kW/cm²)	15 min/ 4 min
2	pAB staining	Homer-rb (1:1000), vGluT2-ch (1:500)		in 0.5% FCS in PBS	45 min
	sAB staining	rb-CF680, ch-AF647 (1:500, each)		in 0.5% FCS in PBS	45 min
	Imaging	100 mM MEA, pH 8		20k frames, 30 ms, 2.7 kW/cm²	
	Label removal	Bleaching: PBS		661 nm (2.7 kW/cm²) + 405 nm (1 kW/cm²)	4 min/ROI
3a/b	pAB staining	WGA-CF680 (1:5000), CHC17-AF647 (1:100)	vGluT1-CF680 (1:100), CHC17-AF647 (1:100)	in 0.5% FCS in PBS	45 min
	sAB staining	-		in 0.5% FCS in PBS	-
	Imaging	100 mM MEA, pH 8		20k frames, 30 ms, 2.7 kW/cm²	15 min/ROI
	Label removal	Elution: 0.1% SDS in PBS (pH 13), Bleaching: PBS		661 nm (2.7 kW/cm²) + 405 nm (1 kW/cm²)	15 min/ 4 min
4	pAB staining	Synaptophysin-rb (1:500), SNAP25-ms(k) (1:200)		in 0.5% FCS in PBS	45 min
	sAB staining	rb-AF647 (1:500), ms(k)-CF680 (1:100)		in 0.5% FCS in PBS	45 min
	Imaging	100 mM MEA, pH 8		20k frames, 30 ms, 2.7 kW/cm²	15 min/ROI
	Label removal	Elution: 0.1% SDS in PBS (pH 13), Bleaching: PBS		661 nm (2.7 kW/cm²) + 405 nm (1 kW/cm²)	15 min/ 4 min
5	pAB staining	VAMP2-rb (1:500), SV2abc-ms (1:500)		in 0.5% FCS in PBS	45 min
	sAB staining	rb-AF647, ms-CF680 (1:500, each)		in 0.5% FCS in PBS	45 min
	Imaging	100 mM MEA, pH 8		20k frames, 30 ms, 2.7 kW/cm²	15 min/ROI
	Label removal	Elution: 0.1% SDS in PBS (pH 13), Bleaching: PBS		661 nm (2.7 kW/cm²) + 405 nm (1 kW/cm²)	15 min/ 4 min
6	pAB staining	VAMP1-rb (1:500), Rab3a-ms(k) (1:200)		in 0.5% FCS in PBS	45 min
	sAB staining	rb-AF647 (1:500), ms(k)-CF680 (1:100)		in 0.5% FCS in PBS	45 min
	Imaging	100 mM MEA, pH 8		20k frames, 30 ms, 2.7 kW/cm²	15 min/ROI
	Label removal	Elution: 0.1% SDS in PBS (pH 13), Bleaching: PBS		661 nm (2.7 kW/cm²) + 405 nm (1 kW/cm²)	15 min/ 4 min
7a/b	pAB staining	Tom20-rb (1:100), PSA-AF647 (1:50)	Tom20-rb (1:100), Synapsin2-ms(IgG1) (1:200)	in 0.5% FCS in PBS	45 min
	sAB staining	rb-CF680 (1:500)	rb-CF680 (1:500), ms(IgG1)-Atto647n (500)	in 0.5% FCS in PBS	45 min
	Imaging	100 mM MEA, pH 8		20k frames, 30 ms, 2.7 kW/cm²	15 min/ROI
	Label removal	Elution: 0.1% SDS in PBS (pH 13), Bleaching: PBS		661 nm (2.7 kW/cm²) + 405 nm (1 kW/cm²)	15 min/ 4 min
8b	pAB staining	PSA-AF647 (1:50)		in 0.5% FCS in PBS	45 min
	sAB staining	-		-	-
	Imaging	100 mM MEA, pH 8		20k frames, 30 ms, 2.7 kW/cm²	15 min/ROI
	Label removal	-		-	-

Table 7.3 P21 Multiplexed Experiment

SR	Treatment	Reagents	Parameters	Duration
1	pAB staining	WGA-AF488 (1:1000), vGluT1-gp (1:500), Piccolo-rb (1:200), Bassoon-ms(k) (1:500)	in 0.5% FCS in PBS	45 min
	sAB staining	gp-AF647, rb-CF680, ms-CF680, ms(k)-CF680 (1:500, each)	in 0.5% FCS in PBS	45 min
	Imaging	100 mM MEA, pH 8	20k frames, 30 ms, 2.7 kW/cm²	15 min/ROI
	Label removal	Elution: 0.1% SDS in PBS (pH 13), Bleaching: PBS	661 nm (2.7 kW/cm²) + 405 nm (1 kW/cm²)	15 min/ 4 min
2	pAB staining	VAMP2-rb (1:500), SNAP25-ms(k) (1:200)	in 0.5% FCS in PBS	45 min
	sAB staining	rb-AF647, ms-CF680 (1:500, each)	in 0.5% FCS in PBS	45 min
	Imaging	100 mM MEA, pH 8	20k frames, 30 ms, 2.7 kW/cm²	15 min/ROI
	Label removal	Elution: 0.1% SDS in PBS (pH 13), Bleaching: PBS	661 nm (2.7 kW/cm²) + 405 nm (1 kW/cm²)	15 min/ 4 min
3	pAB staining	VAMP1-rb (1:500), Rab3a-ms(k) (1:200)	in 0.5% FCS in PBS	45 min
	sAB staining	rb-AF647 (1:500), ms(k)-CF680 (1:100)	in 0.5% FCS in PBS	45 min
	Imaging	100 mM MEA, pH 8	20k frames, 30 ms, 2.7 kW/cm²	15 min/ROI
	Label removal	Elution: 0.1% SDS in PBS (pH 13), Bleaching: PBS	661 nm (2.7 kW/cm²) + 405 nm (1 kW/cm²)	15 min/ 4 min
4	pAB staining	PSA-AF647 (1:50)	in 0.5% FCS in PBS	45 min
	sAB staining	-	-	-
	Imaging	100 mM MEA, pH 8	20k frames, 30 ms, 2.7 kW/cm²	15 min/ROI
	Label removal	-	-	

Table 7.4 GFP Multiplexed Experiment

SR	Treatment	Reagents	Parameters	Duration
1	pAB staining	WGA-AF488 (1:1000), vGluT1-gp (1:500), Piccolo-rb (1:200), Bassoon-ms(k) (1:500)	in 0.5% FCS in PBS	45 min
	sAB staining	gp-AF647, rb-CF680, ms-CF680, ms(k)-CF680 (1:500, each)	in 0.5% FCS in PBS	45 min
	Imaging	100 mM MEA, pH 8	20k frames, 30 ms, 2.7 kW/cm²	15 min/ROI
	Label removal	Elution: 0.1% SDS in PBS (pH 13), Bleaching: PBS	661 nm (2.7 kW/cm²) + 405 nm (1 kW/cm²)	15 min/ 4 min
2	pAB staining	Homer-rb (1:1000), eGFP-ch (1:500)	in 0.5% FCS in PBS	45 min
	sAB staining	rb-CF680, ch-AF647 (1:500, each)	in 0.5% FCS in PBS	45 min
	Imaging	100 mM MEA, pH 8	20k frames, 30 ms, 2.7 kW/cm²	15 min/ROI
	Label removal	Elution: 0.1% SDS in PBS (pH 13), Bleaching: PBS	661 nm (2.7 kW/cm²) + 405 nm (1 kW/cm²)	15 min/ 4 min
3	pAB staining	VAMP2-rb (1:500), SNAP25-ms(k) (1:200)	in 0.5% FCS in PBS	45 min
	sAB staining	rb-AF647, ms-CF680 (1:500, each)	in 0.5% FCS in PBS	45 min
	Imaging	100 mM MEA, pH 8	20k frames, 30 ms, 2.7 kW/cm²	15 min/ROI
	Label removal	Elution: 0.1% SDS in PBS (pH 13), Bleaching: PBS	661 nm (2.7 kW/cm²) + 405 nm (1 kW/cm²)	15 min/ 4 min
4	pAB staining	VAMP1-rb (1:500), Rab3a-ms(k) (1:200)	in 0.5% FCS in PBS	45 min
	sAB staining	rb-AF647 (1:500), ms(k)-CF680 (1:100)	in 0.5% FCS in PBS	45 min
	Imaging	100 mM MEA, pH 8	20k frames, 30 ms, 2.7 kW/cm²	15 min/ROI
	Label removal	Bleaching: PBS	661 nm (2.7 kW/cm²) + 405 nm (1 kW/cm²)	4 min/ROI
5	pAB staining	PSA-AF647 (1:50) and/or WGA-CF680 (1:500)	in 0.5% FCS in PBS	15 min
	sAB staining	-	-	-
	Imaging	100 mM MEA, pH 8	20k frames, 30 ms, 2.7 kW/cm²	15 min/ROI
	Label removal	-	-	